Apertureless Scanning Nearfield Optical Microscopy with Ultra-high Temporal Resolution

Von der Fakultät für Mathematik, Physik und Informatik
der Universität Bayreuth zur Erlangung des Grades eines
Doktors der Naturwissenschaften (Dr. rer. nat.)
genehmigte Abhandlung

vorgelegt von
Matthias Brandstetter
geb. in Pfarrkirchen

1. Gutachter: Prof. Dr. M. Lippitz

2. Gutachter: Dr. L. Kador

Tag der Einreichung: 27.08.2015
Tag des Kolloquiums: 18.12.2015

Abstract

By combining an apertureless scanning nearfield optical microscope (aSNOM) with a pump probe scheme, we create a novel experimental tool called pump probe apertureless scanning near field optical microscope (ppaSNOM), that combines a temporal resolution of 1ps with a spatial resolution of 20nm. This alloptical technique far below the diffraction limit of light allows to study ultrafast processes on the nano scale. As a proof of principle system we choose the mechanical oscillations exhibited by gold nano discs that are impulsively heated through a short pump pulse. First we provide the theoretical foundation needed to understand the optical and mechanical properties of gold nano particles. In particular we use a FEM solver to predict the mechanical properties as well as the field distributions of gold nano discs promising high signal contrast for the experiment operating at 800nm. Furthermore the absorption and scattering cross section calculated with the T-Matrix are used to derive the ideal sample structure. Before aSNOM and farfield pump probe scheme are combined, we characterize them separately. The aSNOM is an interferometric technique that collects light scattered of a dielectric AFM tip. It allows for the simultaneous acquistion of the sample topography, magnitude and phase of the z-component of the electrical nearfield with a spatial resolution of 20nm. The aSNOM measurements of a gold disc with 100nm radius and 50nm height reveal a dipolar plasmon resonance which agrees very well with FEM simulations. In a next step we apply the pump probe measurement scheme to gold nano discs. The impulsive heating of a gold nano disc through a short pump pulse starts mechanical oscillations in the disc. As the volume changes periodically, the optical properties are modulated by the mechanical mode. In this experiment we measure the transient transmission signal of an individual gold nano disc. Changing the delay between pump and probe reveals an oscillatory delay trace as expected. The data analyzation reveals a mechanical oscillation frequency of 10GHz which we can attribute to the first order breathing mode in agreement with FEM simulations. In a

last step we combine the aSNOM with the pump probe scheme in order to create a tool with 1ps temporal and 20nm spatial resolution. As a proof of principle measurement we are looking for a pump induced perturbation of the nearfield signal. We use FEM calculations to simulate the 2D distribution of the nearfield perturbation which reveals a dipolar shape. The measurements of several gold discs show no differential nearfield response. Instead we see a ring like structure in the differential nearfield signal that overlaps with the AFM topography. We conclude that the ring structure is an AFM artefact and that our signal is buried in the noise floor. We use the measurement data to estimate an upper limit for the relative pump induced perturbation. The results agree with T-Matrix simulations which suggest that an increase in relative sensitivity by a factor of 10^{-2} is needed. By reaching the shot noise limit with our ppaSNOM and modifying certain aspects, the detection of timeresolved nearfield signals seems feasible. Some ideas for possible modifications to the ppaSNOM, such as an increase in collection efficiency of the objective or the replacement of the dielectric AFM tip by a metallic tip, are given in the end. Due to time constraints an implementation of the modifications was not possible.

Zusammenfassung

Die vorliegende Arbeit befasst sich mit der experimentellen Umsetzung eines zeitaufgelösten aperturlosen Nahfeldmikroskops (ppaSNOM). Dieses neuartige Experiment ensteht aus der Kombination von einem aperturlosen Nahfeldmikroskop (aSNOM) mit einem Anrege-Abfrage-Experiment. Das neu entstandene Gerät wird eine zeitliche Auflösung von 1ps mit einer räumlichen Auflösung von 20nm verbinden und die Untersuchung von ultrakurzen Prozessen auf der Nanoskala ermöglichen. Der Nachweis über die Funktionsfähigkeit des Gerätes soll dabei an den durch impulsives Heizen mittels eines Pumppulses entstandenen mechanischen Oszillationen von Gold erbracht werden. Im Rahmen der Arbeit werden die für das Verständnis der optischen und mechanischen Eigenschaften von Gold notwendigen theoretischen Konzepte erörtert. Finite-Elemente Simulation werden verwendet um sowohl die mechanischen Eigenschaften, als auch die optischen Eigenschaften von nanoskopischen Goldscheiben vorherzusagen. Mit Hilfe von theoretischen Modelle wird eine Probengeometrie gefunden, welche das differentielle Nahfeldsignal bei einer Wellenlänge von 800nm maximiert. Vor der Vereinigung von aSNOM und der Anrege-Abfrage-Technik, werden die Messmethoden einzeln an Hand von Messungen an nanoskopischen Goldscheiben charakterisiert. Das aSNOM Experiment beruht auf einer interferometrischen Messung des von einer scharfen, dielektrischen AFM Spitze gestreuten Nahfeldes. Gleichzeitig können dabei die Topografie, die z-Komponente des Nahfeldes und die Phase der z-Komponente des Nahfeldes mit einer, nur durch den Spitzenradius begrenzten Auflösung von 20nm aufgezeichnet werden. Nahfeldmessungen an Goldscheiben, welche mit 800nm Wellenlänge angeregt wurden, zeigen die Feldverteilung einer dipolaren Plasmonresonanz. In einem weiteren Schritt werden ein Anrege-Abfrage-Experiment an Goldnanoscheiben durchgeführt. Durch impulsives Heizen mittels eines kurzen Pumppulses werden mechanischen Oszillationen in der Goldscheibe gestartet, welche die optischen Eigenschaften der Goldscheibe periodisch mod-

ulieren. Das verzögerungszeitabhängige transiente Transmissionsignal durch die Goldnanoscheibe zeigt ein periodisch moduliertes Signal. Durch Datenauswertung und den Vergleich mit FEM-Simulationen kann das periodische Messsignal auf die erste Atmungsmode der Goldnanoscheibe bei einer Frequenz von 10GHz zurückgeführt werden. Im letzten Schritt wird die Anrege-Abfrage-Technik im aSNOM implementiert um eine neuartige Untersuchungsmethode zu schaffen welche eine Zeitauflösung von 1ps mit einer Ortsauflösung von 20nm kombiniert. Die Funktion des Gerätes soll an Hand der pumpinduzierten Änderung des Nahfeldes einer Goldnanoscheibe nachgewiesen werden. Die zweidimensionale Form der Nahfeldänderung wird mit Hilfe von FEM-Simulationen berechnet, nach welchen wir ein dipolförmiges Signal erwarten. Im Experiment zeigen Messungen an mehreren Goldnanoscheiben dagegen kein zeitabhängiges Nahfeldsignal. Die Messungen zeigen eine zeitunabhängige, ringförmige Struktur mit den Abmessungen der Goldnanoscheibe. Wir interpretieren diese Struktur als AFM Artefakt. Auf Grundlage der Messungen wird die obere Grenze für die relative zeitabhängige Änderung bestimmt. Der Vergleich von Messung und T-Matrix-Rechnungen zeigt das eine Erhöhung der relativen Messempfindlichkeit von 10^{-2} benötigt wird. Durch Modifikationen des Experiments und durch das Erreichen der Schrotrauschgrenze erscheint die Messung von zeitaufgelösten Nahfeldsignalen möglich. Den Abschluss der Arbeit bilden Vorschläge zur Steigerung der Messempfindlichkeit wie z.B die Erhöhung der Einsammeleffizienz oder den Einsatz einer Metallspitze als starker Streuer. Aus zeitlichen Gründen konnten diese Änderungen nicht mehr durchgeführt werden.

Contents

CHAPTER 1

Introduction

The word ***microscope*** originates from the two greek words ***mikros*** and ***skopein*** which translate to ***small*** and ***look***. Like no other invention, microscopes helped to unveil the previously hidden secrets of nature. Until the 16th century the best tool to investigate nature was the human eye that has a resolution on the order of $100\mu m$. In the late 16th century Hans Lippershey [1] discovered that by placing a few lenses in a tube, one can get a greatly magnified view of an object at the end of the tube. This supposedly was the birth of the first compound microscope. Through the discovery of the light microscope a whole new world was suddenly accessible. With a resolution on the order of $1\mu m$ light microscopes were particularly important for discoveries in biology and medicine as they allow to study human cells and bacteria. The only drawback of conventional optical farfield microscopes is, that they are limited in spatial resolution d by the Abbe diffraction limit

$$d = \frac{\lambda}{2 \cdot NA} \tag{1.1}$$

Since then many other microscopy techniques have been discovered [2–6] that are based on different physical principles. Next to the optical microscopes, electron microscopes and scanning probe microscopes are the most prominent techniques. Scanning probe microscopy and electron microscopy techniques can achieve very high spatial resolutions of less then 0.1Å[7, 8]. Although optical microscopy techniques can't compete with scanning probe and electron microscopy techniques in terms of resolution, they are far from being obsolete as they are a very good approach of investigating light-matter interaction and resolving ultrafast phenomena. There are specialized optical techniques like Stimulated Emission Depletion (STED), Photoactivated Localization Microscopy (PALM) and Nearfield Scanning

Optical Microscopy (NSOM) that circumvent the Abbe limit [9–16]. Another approach of achieving high lateral and spatial resolution is to combine electron microscopy with optics [17–19]. However we prefer the alloptical approach as it allows to directly detect the light-matter interaction. In our group we make use of an apertureless scanning nearfield optical microscope (aSNOM) that is based on the work of R. Vogelgesang et al. [20]. In our aSNOM we circumvent the Abbe diffraction limit by collecting the light that is scattered of a sharp, dielectric AFM tip in the local nearfields of a sample. The aSNOM delivers a spatial resolution of about 20nm which is wavelength independent and only depends on the radius of the apex of the AFM tip. However the spatial resolution limit is not the only feature of a microscopy technique. It is often not only interesting to resolve fine details but also to investigate dynamics of processes. Ideally a measurement tool can achieve high temporal and spatial resolution at the same time. There are different approaches to create tools with these qualities. In this work we want to combine an aSNOM with the pump probe scheme which results in a tool that unites 20nm spatial resolution and 1ps temporal resolution. We demonstrate the functionality of the setup by measuring a perturbation of the nearfield of a gold nano disc which is caused by a mechanical oscillation.
Chapter 2 lays the theoretical foundation that is needed to understand the optical properties of metallic nanoparticles. Different methods to calculate the scattering properties of a metal particle will be introduced. The quasi-static dipole model describes the interaction of the probing AFM tip with a surface in terms of an effective polarizability [21]. The scattered nearfield is expressed in terms of the incident field and the effective polarizability. In the end we describe the interferometric measurement approach that allows us to measure amplitude and phase of the nearfield signals.
After the theoretical foundation has been established we begin chapter 3 by describing technical aspects of this work like the fabrication of our sample system and the sample geometry. We continue by introducing the experimental setups. In particular we describe a farfield pump probe setup that is used to investigate the optomechanical properties of individual gold nano discs. Next we show our implementation of an apertureless scanning optical nearfield microscope (aSNOM) which allows us to record nearfield signals with 20nm spatial resolution. We explain the alignment of the system that makes use of a cross polarization scheme which suppresses the background. In the end we present the combination of pump probe scheme and aSNOM, the so called pump probe apertureless nearfield optical microscope (ppaSNOM) which is a device that is thought to combine 20nm spatial resolution with 1ps temporal resolution or higher. Before combining the pump probe scheme with the aSNOM we perform measurements on each system separatly.
The farfield pump probe setup is used in chapter 4 to investigate the mechani-

cal oscillations of metal particles that are exhibited upon impulsive heating. We introduce Lamb's theory that allows us to analytically determine the mechanical eigenmodes of spherical particles. Because Lamb's theory is only valid for homogenious media, we introduce a numerical model created in Comsol Multiphysics that we use to calculate the mechanical eigenmodes of gold discs. We use the Comsol model to predict the evolution of the oscillation period with respect to the disc radius. The results are compared to transient absorption measurements. Lastly we use T-Matrix simulations to optimize the disc dimensions for the transient nearfield measurements [22].
Chapter 5 presents the nearfield measurements of gold nano discs. In the beginning we describe the difference between an aperture SNOM and an apertureless SNOM in terms of temporal and spatial resolution. We introduce a Comsol model that is used to calculate the field distributions around the gold nano disc. A CW and a pulsed laser source are used to investigate the nearfields around the gold disc.
The combination of farfield pump probe scheme and aSNOM is shown in chapter 6. We start chapter 6 by explaining the procedure that is used to overlap two noncollinear beams in four dimensions. We simulate the transient nearfield signals with the previously described models and discuss the expected features. In the experiment a pump induced nearfield perturbation can be described as the amplitude modulation of a carrier signal. We calculate the interferometer signal of the perturbed nearfields that help to interpret the double modulated signals. Differential nearfield measurements are presented and discussed. In the last part we summarize this work and give a brief outlook.

CHAPTER 2

Theory

This chapter presents the theorectical concepts that are used to explain phenomena observed when studying nanoscopic structures with ultra fast pump probe spectroscopy and nearfield optics. We start by introducing the Maxwell equations. The Drude model is used to calculate the dielectric function of bulk metals. Furthermore we briefly introduce Mie theory which describes the light scattering by a particle and allows to calculate the scattering and extinction cross sections. The limitations of Mie theory motivate the usage of the transmission matrix method (T-Matrix), that allows us to calculate scattering properties of more complicated particle shapes. We introduce the coupled dipole model to describe the fields scattered by the tip sample interaction. Furthermore we give a description of the timedependent fields that are caused by the oscillation of the AFM tip. In the end we give an expression for the detector response.

2.1 Maxwell Equations

The Maxwell Equations form the theoretical basis of the electrodynamical phenomen observed in this thesis. They are constituted by Gauss's Law, Gauss's Law for magnetism, the Maxwell-Faraday equation and Amperè's circuitial law.

$$\nabla \cdot D = \rho \tag{2.1}$$

$$\nabla \cdot B = 0 \tag{2.2}$$

$$\nabla \times E = -\frac{\delta B}{\delta t} \tag{2.3}$$

$$\nabla \times H = J + \frac{\delta D}{\delta t} \tag{2.4}$$

E and H are the electric and magnetic field, J is the total current density, ρ is the charge density. The displacement field D is a vector field that accounts for charges in materials and for dielectric media. D can be written as

$$D = \epsilon_0 E + P \tag{2.5}$$

with ϵ_0 being the vacuum permittivity and P being the polarization density. B is the magnetic flux density that is related to the magnetic field vector H via

$$B = \mu_0 H + M \tag{2.6}$$

with μ_0 being the magnetic permeability and M being the magnetization. The total displacement field D can also be written as

$$D = \epsilon_0 \epsilon_r E \tag{2.7}$$

where the relative electrical permittivity

$$\epsilon_r = 1 + \frac{P}{\epsilon_0 E} \tag{2.8}$$

contains the material response to the electric field.

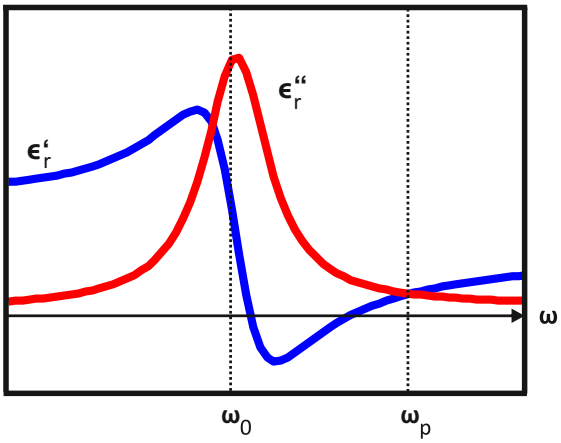

Figure 2.1 *Real part $\epsilon_r^{'}$ and imaginary part $\epsilon^{''}$ of the dielectric funtion calculated in the Lorentz-Model.*

2.2 Lorentz-Model

The material response to an incident electric field E is frequency dependent so that $P = P(\omega)$ and $\epsilon_r = \epsilon_r(\omega)$.
A classical approach to model this frequency dependence was given by Lorentz [23]. Lorentz proposed that the electron is bound to the nucleus of the atom by a force that behaves according to Hooke's Law. The harmonic oscillator equation for an electron bound to a nucleus can be written as

$$\frac{\delta^2 P(\omega,t)}{\delta t^2} + \gamma \frac{\delta P(\omega,t)}{\delta t} + {\omega_0}^2 P(\omega,t) = -\epsilon_0 {\omega_p}^2 E(\omega,t) \tag{2.9}$$

where $P(\omega) = Pe^{i\omega t}$ is the polarization density, γ is the dampening coefficient, $E(\omega,t) = Ee^{i\omega t}$ of the driving electric field and $\omega_p = \sqrt{\frac{n_e q^2}{m\epsilon_0}}$ is the plasma frequency. Combining and evaluating 2.8 and 2.9 yields the complex relative permittivity as

$$\epsilon_r = 1 + \frac{{\omega_p}^2}{\epsilon_0({\omega_0}^2 - \omega^2) + i\omega\gamma} \quad . \tag{2.10}$$

The complex relative permittivity can be separated in a real and an imaginary part which equate to

$$\epsilon_r^{'}(\omega) = 1 + \frac{{\omega_p}^2(\omega_0^2 - \omega^2)}{(\omega_0^2 - \omega^2)^2 + \omega^2\gamma^2} \tag{2.11}$$

and

$$\epsilon_r^{''}(\omega) = \frac{{\omega_p}^2\gamma\omega}{(\omega_0^2 - \omega^2)^2 + \omega^2\gamma^2} \quad . \tag{2.12}$$

Figure 2.1 shows a plot of $\epsilon_r^{'}$ and $\epsilon_r^{''}$ for arbitrary values of ω_0,ω_p and γ.

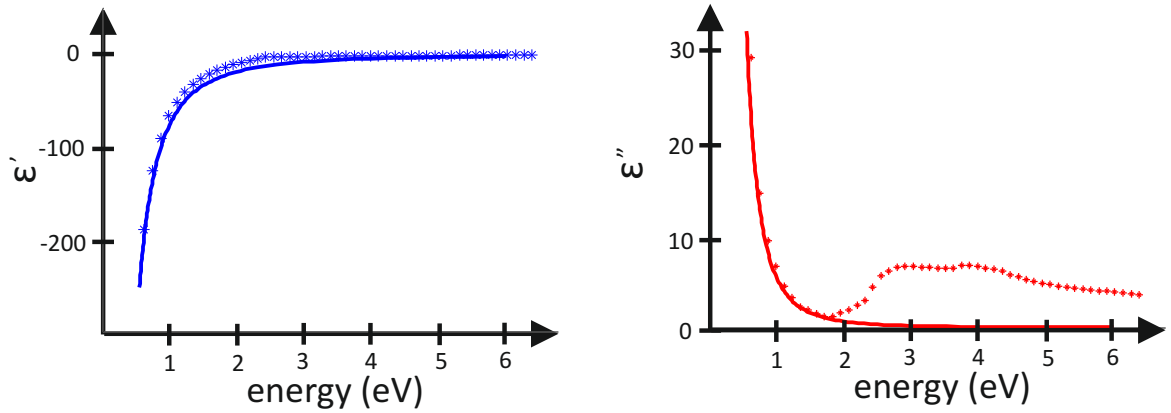

Figure 2.2 *Real and imaginary part of the dielectric function for gold. The Drude model (solid line) is in very good agreement with the data measured by Johnson and Christy (stars) in a range beween* $0.8eV$ *and* $2eV$ *.*

2.3 Drude Model

To model the dielectric response of metals Drude considered electrons as a gas of negatively charged particles that are embedded in a matrix of positively charged ions. The model applies classical mechanical theory to describe the transport properties of conduction electrons in a metal [24]. Because the conduction electrons are considered free $\omega_0 = 0$. Therefore equation 2.10 simplifies to

$$\epsilon_r = 1 + \frac{{\omega_p}^2}{-\epsilon_0\omega^2 + i\omega\gamma} \tag{2.13}$$

The complex relative permittivity can be separated in a real and an imaginary part which equate to

$$\epsilon_r^{'}(\omega) = 1 - \frac{{\omega_p}^2}{\omega^2 + \gamma^2} \tag{2.14}$$

and

$$\epsilon_r^{''}(\omega) = \frac{{\omega_p}^2\omega}{\omega^3 + \omega\gamma^2} \quad . \tag{2.15}$$

In order to make use of the Drude model for real metals, one has to find the values for the parameters ω_p and γ. Figure 2.2 shows the real and imaginary part of the dielectric function calculated in the Drude model with $\omega_p = 9.06eV$ and $\gamma = 62.03meV$ [25]. In an energy range between $0.8eV$ and $2eV$ the Drude model matches the data as measured by Johnson and Christy [26] very well. At $2eV$ and above the imaginary part calculated by the Drude model deviates from the measured data. The increase of the imaginary part in the measured data is caused by the gold d-band absorption which the Drude model doesn't account for.

In this work the plasmonic properties of gold were studied in an energy range

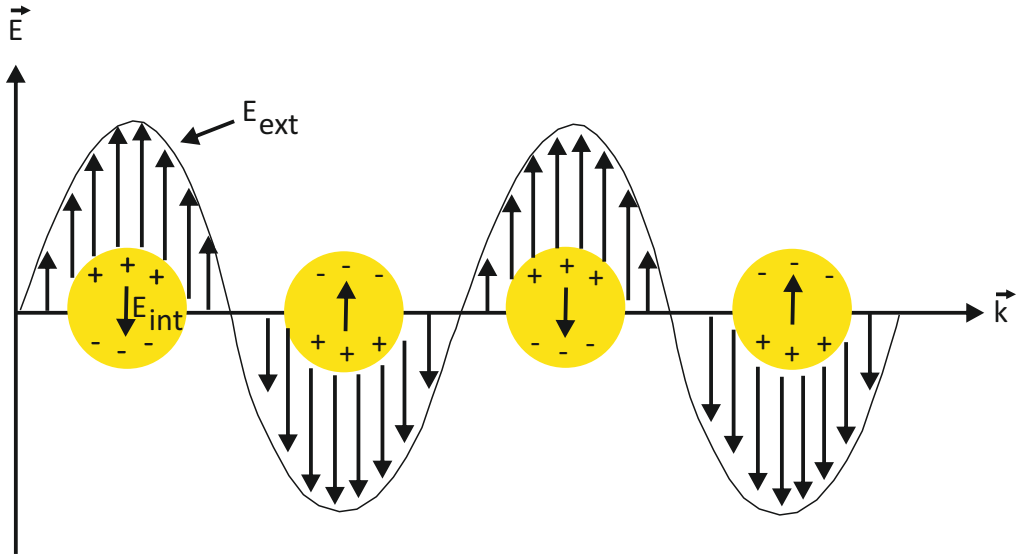

Figure 2.3 *Quasi-static model for the interaction of a plasmon and an external field.*

between $1.4eV$ and $2.3eV$. As the Drude model models this energy range insufficiently, the optical constants of gold as measured by Johnson and Christy were used throughout this thesis.

2.4 Plasmons

Plasmons are collective oscillations of the free electron gas density. The energy of a plasmon can be estimated as

$$\omega_p = \sqrt{\frac{n_e q^2}{m\epsilon_0}} \quad . \tag{2.16}$$

If a lightfield interacts with a metallic particle whose dimensions are much smaller than the wavelength of the lightfield, a quasi-static model can be used to describe the interaction between an internal field and external electric field. This approach assumes that the phase of the external field is constant over the particle and therefore can be neglected. If the particle approaches the dimensions of the wavelenth of the external field retardation effects due to self-induction need to be taken into account. However it has been shown that even for particle sizes that approach the wavelength of external the field, the coupled dipole approximation delivers good results [27]. Figure 2.3 shows the interaction of a free electron density with an external field.

In the quasi-static approach the polarizability of a metal sphere can be calculated according to the Claudius-Mossotti relation

$$\alpha = \epsilon_0 \cdot 3 \cdot V \frac{\epsilon_r - 1}{\epsilon_r + 2} \tag{2.17}$$

with the complex dielectric function relative to the medium

$$\epsilon_r = \epsilon_r' + i \cdot \epsilon_r'' = \frac{\epsilon_{metal}}{\epsilon_{medium}} \tag{2.18}$$

and V as the volume of the particle. The scattering and absorption cross section are then given by [28]

$$C_{Sca} = \frac{k^4}{6\pi} \cdot (3V^2) \frac{(\epsilon_r' - 1)^2 + \epsilon_r''^2}{(2 + \epsilon_r')^2 + \epsilon_r''^2} \tag{2.19}$$

$$C_{Abs} = k \cdot 3 \cdot V \frac{3\epsilon_r''^2}{(2 + \epsilon_r')^2 + \epsilon_r''^2} \tag{2.20}$$

From equation 2.19 we see that the resonance condition for spherical particles is $\epsilon_r' = -2$. Note that the scattering cross section $C_{Sca} \propto V^2$ whereas the absorption cross section $C_{Abs} \propto V$. Therefore for small particles C_{Abs} dominates the optical properties, whereas for large particles C_{Sca} holds the main contribution to the optical properties.

2.5 Mie theory

For spherical nanoparticles, an analytical solution for the extinction and scattering properties was found by Gustav Mie [29]. The Mie solution to 2.9 describes the scattering of electromagnetic radiation by a sphere and allows for calculation of important scattering parameters such as the extinction cross section σ_{ext} and the scattering cross section σ_{scat}. The concept of the cross section describes a geometrical area in which an incident photon reacts with a particle. The extinction cross section represents the total losses of energy from the incident flux due to both absorption and scattering, and is defined as the sum of the absorption and scattering cross sections. Through series expansion of the electric field into partial waves the expressions for the extinction cross-section σ_{ext} and scattering cross-section σ_{scat} can be derived [30]. It can be shown that

$$\sigma_{ext} = \frac{2\pi}{|k|^2} \sum_{l=1}^{+\infty} (2l + 1) Re(a_l + b_l) \tag{2.21}$$

and

$$\sigma_{sca} = \frac{2\pi}{|k|^2} \sum_{l=1}^{+\infty} (2l + 1) Re(|a_l|^2 + |b_l|^2) \tag{2.22}$$

with

$$a_l = \frac{m\Psi_l(mx)\Psi_l{}'(x) - \Psi_l{}'(mx)\Psi_l(x)}{m\Psi_l(mx)\eta_l{}'(x) - \Psi_l{}'(mx)\eta_l(x)} \tag{2.23}$$

and

$$b_l = \frac{\Psi_l(mx)\Psi_l{}'(x) - m\Psi_l{}'(mx)\Psi_l(x)}{\Psi_l(mx)\eta_l{}'(x) - m\Psi_l{}'(mx)\eta_l(x)} \tag{2.24}$$

with $m = \frac{n}{n_m}$ where n is the complex refractive index of the particle and n_m is the refractive index of the surrounding medium. k is the wave-vector and $x = |k|r$ with r being the radius of the sphere. Ψ_l and η_l are the l-th order Ricatti and Bessel cylindrical functions. l is the summation index of the partial waves. $l = 1$ corresponds to the dipole oscilation while $l = 2$ is associated with the quadrupole oscillation.

The absorption cross section σ_{abs} is given by

$$\sigma_{abs} = \sigma_{ext} - \sigma_{scat} \quad . \tag{2.25}$$

As an example, figure 2.4 shows the scattering, extinction and absorption cross section of a gold sphere of 100nm diameter. Note that at these particle dimensions, the extinction cross section is dominated by the scattering contribution. Furthermore figure 2.4 depicts a comparison of the extinction cross section of a 100nm sized sphere consisting of several typical metals. For a given sphere radius the extinction resonance can be shifted throughout the visible regime by employing different materials. Due to high internal losses nickel has a broad resonance with low peak extinction cross section. Silver has the highest peak extinction cross section in this comparison. For our samples we use gold as a material as the degradation of gold samples is much lower and gold is also easier to handle in the fabrication process.

2.6 T-Matrix method

Unfortunately the analytical Mie solution is restricted to spherical particles. To simulate scattering problems of more advanced structures the T-Matrix method (transmission matrix) is used in this thesis. The T-Matrix method was formulated by P. C. Waterman [22] and is also known as the null-field method or the extended boundary condition method. In the T-Matrix method the incident, internal and scattered fields of a scattering problem are expanded into spherical wave funtions. The T-Matrix relates the expansion coefficient of the involved fields. For a given incident field, the internal and scattered field are determined under the condition of fulfilling the Maxwell equation as well as transmission conditions given by the particle surface. The T-Matrix calculations carried out in this thesis were done using a Matlab script that was developed in earlier work [31][32].

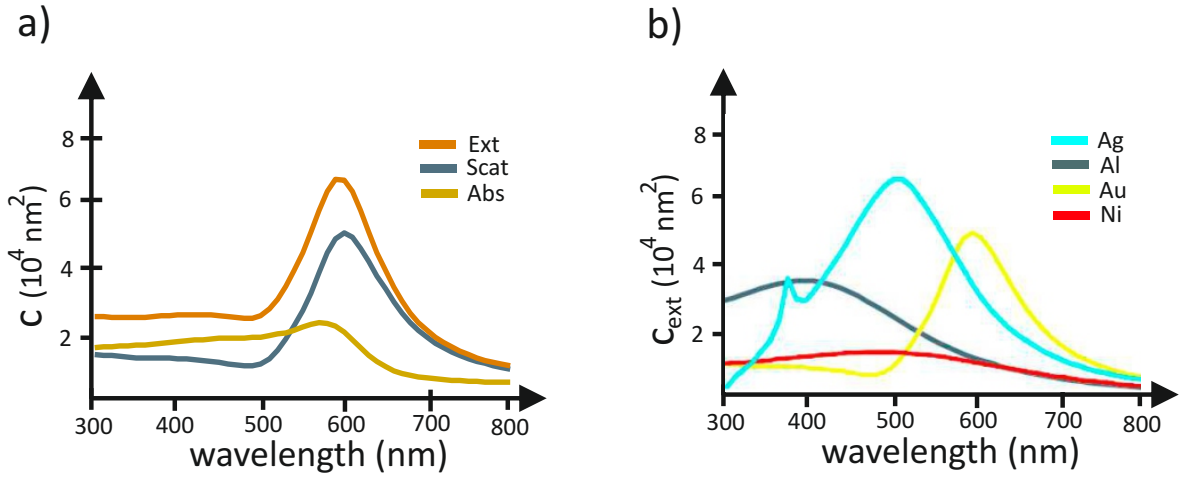

Figure 2.4 *a) Mie calculations for a gold sphere of 100nm diameter. The scattering cross section c_{Scat} shows a resonance at a wavelength of 600nm. The extinction cross section c_{ext} is dominated by c_{Scat}. b) Mie calculations for a 100nm sized sphere consisting of different metals. The plot shows the extinction cross section c_{ext} in dependence of the wavelength. For these particle dimensions, gold and silver exhibit strong resonances in the visible regime. The resonance of nickel is not very pronounced due to high internal losses.*

Figure 2.5 shows a comparison between a measurement of the normalized extinction cross section of gold discs of 50nm height and varying diameter obtained with an FTIR (Fourier transform infrared spectrosopy) and calculation results obtained with T-Matrix. The T-Matrix calculation uses the dielectric function of gold measured by Johnston and Christy [26] as well as an effective medium refractive index of $n_{eff} = 1.4$. The comparison shows a good agreement between computed and measured data. Due to the good agreement of measurement and simulation the T-Matrix method is employed throughout this thesis.

As will be seen in chapter 4, the measurement signal we are interested in stems from the periodic volume change of a gold nano disc that was excited by a short pump pulse. The periodic volume change causes a change in the dieelectric properties of the particle as ω_p in equation 2.10 is related to the electron density n_e via

$$\omega_p = \sqrt{\frac{n_e e^2}{m \cdot \epsilon_0}} \tag{2.26}$$

The parameter we are interested in is the change in the absorption cross section Δc_{ext} as this is directly proportional to the measurement signal. Figure 2.6 shows a comparison of the extintinction cross section of a disc in its ground state (cold) and in its excited state (hot).

In order to simulate Δc_{ext} the volume change ΔV induced by the temperature

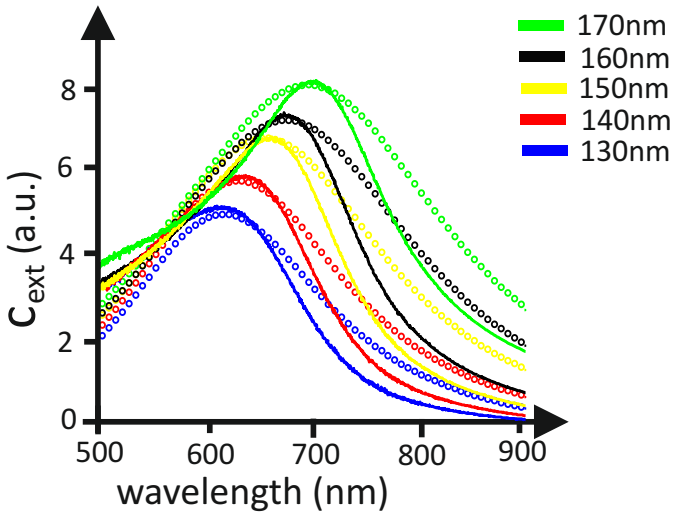

Figure 2.5 *Comparison of the extinction cross section as calculated by T-Matrix with measurements on a widely spaced gold disc array obtained by FTIR. The discs have a height of* $50nm$*. The extinction resonance shifts to longer wavelength as the disc diameter increases. The T-Matrix calculations depend on an effective refractive index, as the method assumes that the particle is surrounded by a homogeneous medium. This doesn't resemble the sample conditions as the gold discs were fabricated on a glass substrate. However an effective refractive index* $n_{eff} = 1.4$ *matches the measurements quite well.*

change dT caused by the absorption of a pump pulse has to be determined. We can write

$$\Delta V = (1 + \alpha \cdot dT) \cdot V_{equ} \tag{2.27}$$

where α is the thermal expansion coefficient, dT the temperature change and V_{equ} is the volume of the disc in its ground state.
To estimate dT, the energy a pump pulse deposits in the particle has to be calculated. A typical experiment situation involved gold discs with a volume of $V = (100nm)^3$ (disc radius 100nm, disc height 50nm), a focus size for the pump beam of $A_{focus} = (100nm)^2$, a pump power $P_{pump} = 1mW$ and a repetition rate $f_{rep} = 80MHz$. A typical value for the deposited energy is $\Delta Q = 100fJ$. c_{abs} is a function of the wavelength and is determined by T-Matrix simulations to be $c_{abs} = 100^2 \cdot nm^2$. The temperature change dT in the gold particle can therefore be estimated as

$$dT = \frac{p_{pump} \cdot c_{abs}}{A_{focus} \cdot f_{rep} \cdot m_{disc} \cdot c_{Au}} \approx 10K \tag{2.28}$$

Knowing ΔT, the T-Matrix code can now be used to calculate the cross section data for a gold disc in its ground state and excited state. The differential cross

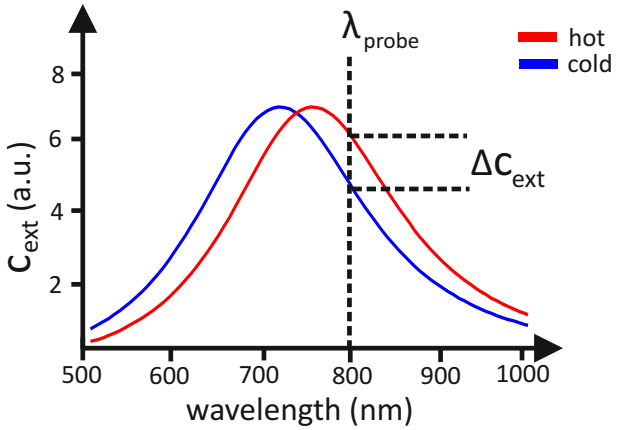

Figure 2.6 *The plasmon resonance of a nano structure at thermal equilibrium (cold) and while being hot. The temperature increase causes an expansion of the particle and thus a decrease in electron density n_e. The change in extinction Δc at the wavelength λ_{probe} can be measured in a transmission experiment.*

section is obtained via

$$\frac{\Delta c_{sca}}{c_{sca,gs}} = \frac{c_{sca,es} - c_{sca,gs}}{c_{sca,gs}} \tag{2.29}$$

An example calculation for the differential scattering cross section $\Delta c_{sca}/c_{sca,gs}$ can be seen in figure 2.7.

2.7 Nearfield theory

Conventional far field techniques have a resolution limit that was first introduced by Lord Rayleigh. The Rayleigh criterion states that two point sources can be regarded as just resolved when the principal diffraction maximum of one image coincides with the first minimum of the other [33]. If the distance is greater, the two points are distiniguishable and if it is smaller, they are not distinguishable. For a microscope the Rayleigh criterion can be written as [33]

$$\Delta R = 1.22\lambda/NA \tag{2.30}$$

with ΔR being the resolution, λ being the wavelength of light, $NA = n \cdot sin(\alpha)$ being the numerical aperture and n being the refractive index. A typical limit for optical farfield measurements is $\Delta R \approx 200nm$ which makes it impossible to resolve detailed field information of plasmonic nanostructures which typically have a size on the order of 100nm. The idea of a nearfield microscope was first formulated by Synge [34]. Synge suggested a super resolution microscope that achieves the resolution by bringing a probe in the shape of a nanometer sized aperture in the close vincinity of the sample, thereby interacting with the evanescent fields.

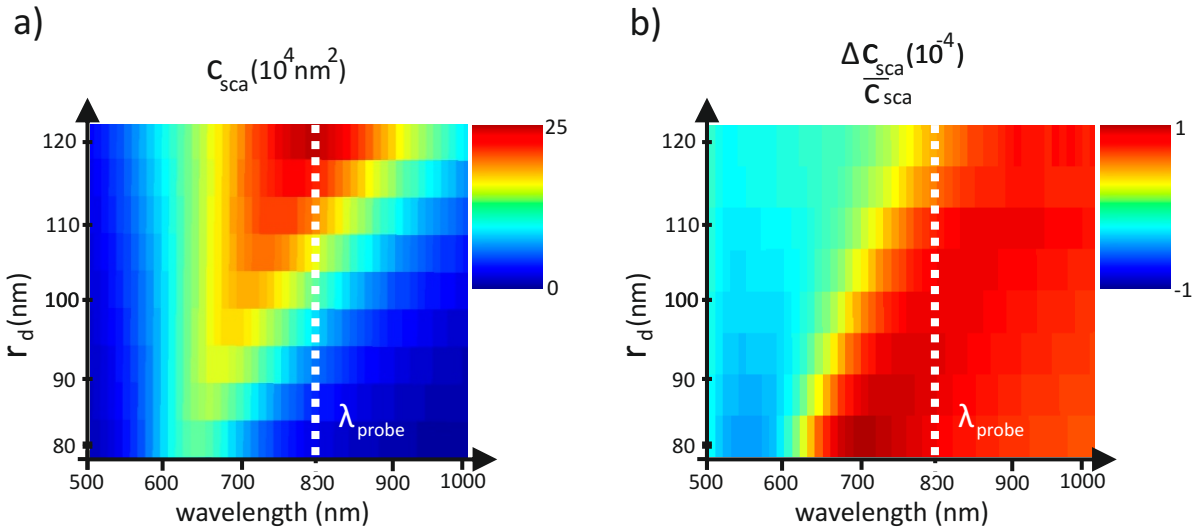

Figure 2.7 *a) T-Matrix calculations of a gold disc of 50nm height and varying radius plotted against the wavelength. The color scale depicts the magnitude of the scattering cross section c_{sca}. The maximum of c_{sca} shifts to longer wavelengths with increasing diameter. The white dashed line represents the wavelength of our laser system. Figure b) shows the differential scattering cross section of a gold disc for a temperature change $\Delta T = 10K$ as obtained with T-Matrix calculations. The color scale has positive and negative values depending on which side of the resonance Δc_{scat} is analyzed. In order to gain the highest imaging contrast the c_{sca} has to be probed at the position of highest slope.*

In the context of near field microscopy there are two approaches to circumvent the Rayleigh criterion. One approach is to gain resolution by confining a lightsource to nanoscopic scales via an aperture. The second method gains resolution by confining the interaction volume between probe and sample to a nanoscopic volume.

Figure 2.8 visualizes the differences between aperture and apertureless nearfield microscope.

2.8 Signal Modulation

The basis of our aSNOM is an AFM in which the height feedback is accomplished by monitoring the oscillation amplitude of the AFM cantilever. The harmonic motion of the tip perpendicular to the sample surface is depicted in figure 2.9 a). The tip-surface distance as a function of time t can be written as

$$d_z(t) = d_0 - d_A \cdot \sin(\omega \cdot t + \phi)$$

where d_0 is the mean tip surface distance, d_A is the oscillation amplitude and ω is the oscillation frequency which is roughly 300kHz in our case. The mean tip sample distance d_0 in non contact mode is on the order of 10nm and the oscillation

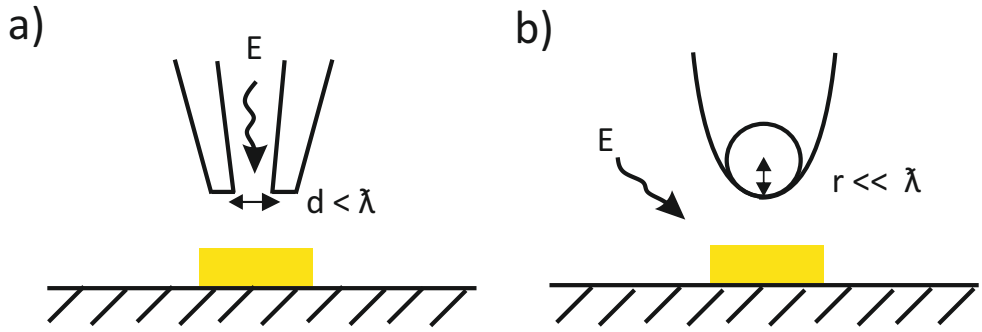

Figure 2.8 *a) Nanoscale lightsource illuminating the surface. The light confinement is usually achieved by tapering a glass fiber und coating a metal on it. The resolution is determined by the diameter d of the aperture [35]. Due to reciprocity reasons the nanoscale lightsource could also be used as nanoscale detector. b) A sharp probe in the vicinity of a sample is illuminated by E. In this apertureless configuration the interaction between probe and evanescent nearfield causes light to be scattered of the probe. Due to the small interaction volume of probe and surface, the lateral resolution can be very high and is defined by the probe radius r.*

amplitude of the tip is around $d_A \approx$ 10nm. The driving wavelength of the optical fields of the sample is 800nm. The distance dependence of the electric nearfield can be written as

$$E_{d_z} = E_{nf,0} \cdot e^{\frac{-d_z}{z}}$$

The nearfield E_{nf} which is scattered from the tip is proportional to the nearfield E_{d_z} and therefore

$$E_{nf}(t) \propto E_{nf,0} \cdot e^{\frac{-d_0}{z} + \frac{d_A}{z} \cdot \sin(\omega \cdot t + \phi)}$$

The taylor expansion of this expression yields

$$E_{nf}(t) \propto E_{nf,0} \cdot e^{\frac{-d_0}{z}} \cdot (\frac{d_A}{z} + \frac{d_A}{z} \cdot sin(\omega \cdot t + \phi) + \frac{(\frac{d_A}{z} \cdot sin(\omega \cdot t + \phi))^2}{2} + \frac{(\frac{d_A}{z} \cdot sin(\omega \cdot t + \phi))^3}{6} + ...)$$

Therefore E_{nf} is modulated on harmonics of the cantilever oscillation frequency.

2.9 AFM tip in a farfield focus

A big challenge in nearfield microscopy is to separate the weak nearfield signals from other signal contributions. Figure 2.10 shows a sketch of the magnified view of the AFM tip in a diffraction limited focus. Due to the evanescent nature of the nearfields, effective tip-field interaction only occurrs at the very tip apex. Comparing the geometric cross section of the tip apex of

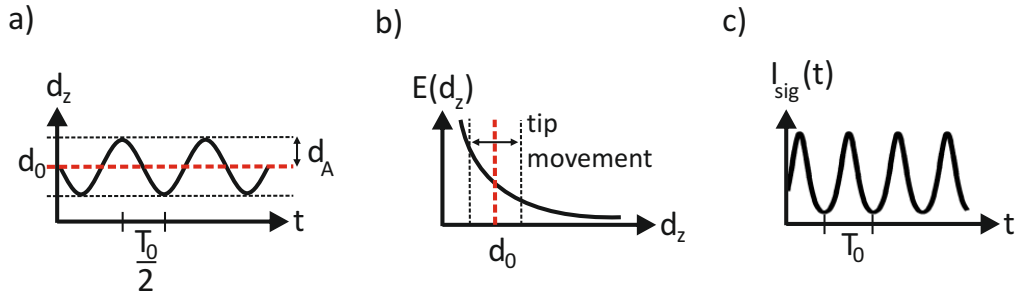

Figure 2.9 *a) Periodic distance dependence of an oscillating AFM tip. The red dashed curved denotes the mean position commonly referred to as the set point in AFM software. b) Visualization of exponentially decaying evanescent fields. The tip oscillation takes place in a zone of large field gradient.*
c) Time dependent scattering signal.

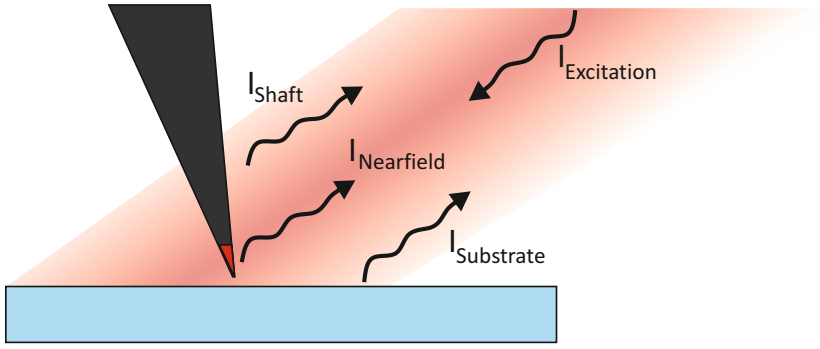

Figure 2.10 *Schematic representation of the different contributions to the optical signal. The diffraction limited spot is much larger than the AFM tip apex. A combination of cross polarization scheme and higher harmonic demodulation isolates the weak nearfield signals.*

$$\sigma_{tip} = \pi \cdot {r_{apex}}^2$$

$$\sigma_{tip} = \pi \cdot (20 \cdot 10^{-9} nm)^2$$

with r_{apex} being the radius curvature with the focus area

$$A_{focus} = \pi \cdot (1000 \cdot 10^{-9} nm)^2$$

one can see that a huge area around the AFM tip is illuminated which causes a big background signal. The light that is collected by the objective has several components (see figure 2.10). To separate the nearfield signal from the large background a modulation/demodulation scheme and a cross polarization scheme are employed. As shown in the last section the nearfield signal is modulated on harmonics of the cantilever oscillation frequency. This means that demodulating the detector signal on higher harmonics discriminates the nearfield signal from signal that stems from the reflection of the AFM tip shaft I_{Shaft}, as the tip shaft signal is only modulated

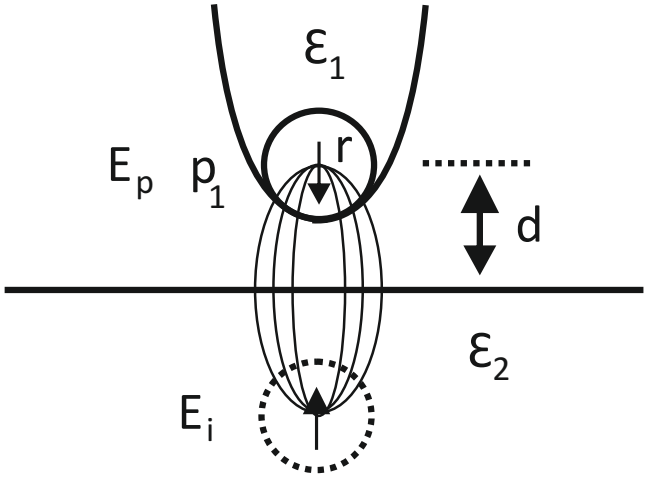

Figure 2.11 *Quasi-static dipole model to describe the interaction of an AFM tip with a surface. The incident radiation excites a dipole in a sphere, which represents the tip. This in turn induces an image dipole in the material, which also interacts with the sphere. The combined system responds with an effective total polarizability* α_{eff}.

at the fundamental frequency. In addition we employ a cross polarization scheme where excitation and detection polarization are orthogonal to each other. In this scheme, we illuminate the sample with s-polarized light. Excitations on the sample can have p-polarized out of plane components of the electric nearfield. The tip can couple efficiently to these out of plane components and scatters them into the farfield. The collected light is analyzed in front of the detector for p-polarization. By separating excitation and detection polarization, light which is reflected of the sample surface and the AFM tip can be fully suppressed.

There are several ways of how to model the tip sample interaction. One of the easiest models is the coupled dipole model in which the tip is reduced to a homogenous sphere of radius r with a dielectric constant ϵ_1 that is placed next to a surface at distance d. The surface has a dielectric constant ϵ_2 and represents the sample [36]. The induced dipole moment in the sphere p_1 can be approximated as [37]

$$p_1 = \alpha(E_p + E_i(r+d)) = \alpha E_p + \frac{\beta p_1}{2\pi(2(r+d))^3} \tag{2.31}$$

where E_p is the primary field. E_i is the image field at the position of the sphere and

$$\alpha = 4\pi r^3 \frac{\epsilon_1 - 1}{\epsilon_1 + 2} \tag{2.32}$$

is the polarizability of the sphere. The induced image dipole moment can be written as

$$\beta p_1 = \frac{\epsilon_2 - 2}{\epsilon_2 + 1} p_1 \tag{2.33}$$

The combined tip-sample system can now be described with the effective polarizability α_{eff}

$$\alpha_{eff} = \alpha(1 - \frac{\alpha\beta}{16\pi(r+d)^3})^{-1} \tag{2.34}$$

such that $p_1 = \alpha_{eff} E_p$. The field emitted by the sphere modeled tip is directly proportional to p_1.
For the signal I_{det} at the farfield detector the following we can write [21]

$$I_{det} = |E_{nf} + E_s|^2 \tag{2.35}$$

where E_s stems from background scattering by the tip. It can be shown that the signal at the detector I_{det} can be written as [38] [21]

$$I_{det} \propto E_{nf} \cdot E_s \propto a_{eff} \tag{2.36}$$

2.10 Interferometric Detection

Silicon AFM tips are highly popular for AFM measurements as they are resistant to wear off, they can be manufactured with a small radius of curvature [39] and therefore deliver high resolution and can be fabricated cheaply. A silicon tip only interacts weakly with plasmonic nearfields which makes imaging of unperturbed plasmonic eigenmodes possible [40]. However, because the interaction of tip and nearfield is weak [40], interferometric amplification is essential to be able to record nearfield signals. The interferometric signal on the detector can be written as the intensity of the superposition of two electric fields E_{nf} and E_{ref} which represent the light that is scattered of the AFM tip and the light of the reference path. We can write

$$\begin{aligned} I &= |E_{nf} + E_{ref}|^2 \\ I &= {E_{nf}}^2 + {E_{ref}}^2 + 2 \cdot \Re(E_{nf} \cdot E_{ref}) \\ I &= {E_{nf}}^2 + {E_{ref}}^2 + 2 \cdot E_{nf} \cdot E_{ref} \cdot cos\phi \end{aligned}$$

with ϕ being the phase between E_{nf} and E_{ref}. The components of the equation that contain information about the electric near field are ${E_{nf}}^2$ and the interference term $2 \cdot E_{nf} \cdot E_{Ref} \cdot cos\phi$. The harmonic oscillation of the AFM tip modulates E_{nf}. Due to the modulation/demodulation scheme used in this experiment ${E_{Ref}}^2$ doesn't contribute to the Lock-In Signal as it is unmodulated. Furthermore $I = {E_{nf}}^2$ can

also be neglected because usually $E_{nf} \ll E_{ref}$ and therefore $E_{nf} \cdot E_{ref} \gg E_{nf}^2$ [41]. Given these assumptions, the resulting signal I_{det} can be written as

$$I \approx 2 \cdot E_{Sig} \cdot E_{Ref} \cdot cos\phi \quad \text{or}$$
$$I \approx 2 \cdot \sqrt{I_{Sig} \cdot I_{Ref}} \cdot cos\phi \quad .$$

This means that the signal magnitude can be amplified by the reference beam. Also the field information is preserved in the Lock-In Signal, as long as the phase of the reference field is constant.
The interferometer allows to reconstruct the optical magnitude A_{opt} and phase $\Delta\phi$. We use the homodyne measurement scheme in which the Lock-In signal is measured for two phase delays between signal and reference arm. The phase delay is accomplished by changing the optical path length of the reference arm. The resulting phase delay is given by

$$\Delta\phi = 2\pi\frac{\Delta x}{\lambda}$$

where λ is the wavelength and Δx is the change in the path length of one interferometer arm. Each of the two measurements provides a Lock-In measurement value of $S_{1,2}$ with

$$S_{1,2} = A_{opt} \cdot \cos\phi_{1,2}$$

Changing the phase by $\Delta\phi = 90°$, the two measurement values $S_{1,2}$ span a rectangular coordinate system in the complex plane in which the optical magnitude and phase can be calculated as

$$A_{opt} = \sqrt{{S_1}^2 + S_2^2}$$
$$\phi_{opt} = \tan\frac{S_2}{S_1}$$

The phase change of 90° is accomplished by shifting the voltage on the piezo delay. Because the magnitude of the shift is unknown at first, a calibration measurement has to be done (see figure 2.12). Scanning the voltage on the piezo delay, the Lock-In amplitude S shows an oscillatory behaviour that corresponds to constructive and destructive interference of signal and reference beam. For the homodyne measurement mode the piezo delay positions are set to V_1 and V_2 respectively.

The measurements $S_{1,2}$ are projections of the total signal A in the complex plane. In order to adress the full range of $\phi \in [0°, 360°]$, it is important to attribute a sign to the two measured amplitudes $S_{1,2}$. We choose to assign a negative amplitude if the lock-in phase is $\phi \in [-180°, 0°]$ and a positive amplitude for $\phi \in [0°, 180°]$.

2.11 Signal to noise ratio (SNR)

As was shown in the last section, the Lock-In signal I is proportional to the interference term

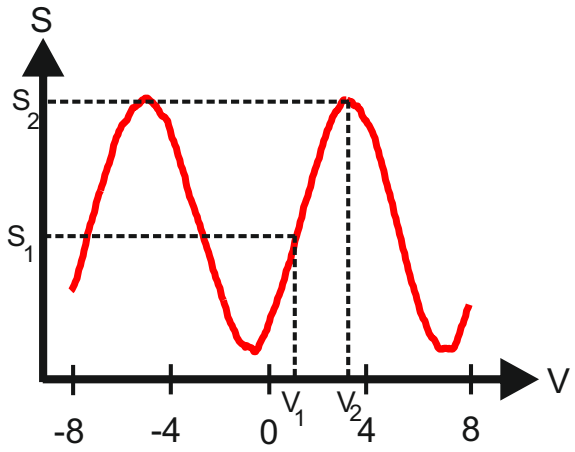

Figure 2.12 *A calibration measurement is used to determine the relation between the piezo voltage of a movable mirror and the phase difference in the reference arm.*

$$I \approx 2 \cdot \sqrt{I_{Sig} \cdot I_{Ref}} \cdot cos\phi.$$

The fundamental noise limit that can be reached is given by the statistical fluctuation of the photon flux which is also called shot noise. In a shot noise limited experiment the signal to noise (SNR) ratio is

$$SNR \propto \frac{\sqrt{I_{sig} \cdot I_{ref}}}{\sqrt{I_{total}}}$$

and because $I_{sig} << I_{ref}$ the equation simplfies to

$$SNR \propto \sqrt{I_{sig}}$$

This means that I_{ref} cannot be used to increase the SNR, although it is useful to raise the interferometer signal above the noise floor of the electrical components in the detection chain.

2.12 Summary

In this chapter theoretical concepts of nano optics have been introduced. In the beginnig the Drude model was used to calculate the dielectric properties of gold. Furthermore the scattering properties of gold spheres have been calculated using Mie theory and T-Matrix calculations. The T-Matrix calculations are used to determine the change in scattering cross section that is caused by a mechanical oscillation of the particle. In the second part we introduce the coupled dipole model that can be used to describe the interaction of a nearfield probe with the surface. The model gives relations for the expected nearfield signals that are dependent on the radius

of curvature of the nearfield probe, the distance between probe and surface and the dielectric function of tip and sample. In the end we describe the components that make up the detector signal in our aSNOM in which the weak nearfield signals are isolated from a large background by using a cross polarization scheme and higher harmonic demodulation.

CHAPTER 3

Technology

Creating a tool that can resolve ultrafast processes on the nanoscale is a challenging task. The tool we want to create consists of an apertureless scanning nearfield optical microscope (aSNOM) that is combined with a pump probe scheme. The result is a tool that can resolve spatial details with 20nm resolution and a temporal resolution 1ps. The first part of this chapter briefly introduces the sample system which is composed of gold nano discs that are designed to have a good optical response at the driving laser wave length of 800nm. The second part gives an overview of the different experimental setups that were employed in order to achieve 20nm spatial resolution and 1ps temporal resolution in one setup.

3.1 Sample system

The optical properties of metallic nano structures are strongly dependent on size, material, shape and the dielectric environment. For this project we want to have nano structures that are robust, easy in handling, have a spectral overlap with our laser source and exhibit high nearfields. We choose gold as a material as its properties are well known, it's chemically inert and the sample fabrication process is easy. Furthermore we opt for discs as nano structure geometry as they possess a high degree of symmetry which makes alignement in a setup easier. With the structure and material set, we used T-Matrix simulations to determine the radii of the discs that have optical properties suitable for our experiments. Typical disc dimensions were a radius of 100nm and a height of 50nm. The gold discs exhibit a dipolar plasmon when excited with 800nm light. The dipolar plasmon resonance creates hotspots in the field distribution that help us to create a big nearfield signal. The

field distribution around the gold discs will be discussed in more detail in 5.1. The sample fabrication is done by electron beam lithography. This allows to fabricate nanometer sized structures with a high accuracy and reproducibility. The fabrication process involves creating an evaporation mask made out of PMMA, evaporating gold onto the surface and removing the PMMA mask with a solvent afterwards. The design of the sample structures is adapted to the measurement technique we want to use it with. In the case of the farfield pump probe measurements we want enough spacing between individual disc so that within the focus there is only one disc. Therefore the farfield samples consist of discs arranged in arrays with a lattice constant of $5\mu m$. An example for such a sample is shown in figure 3.1

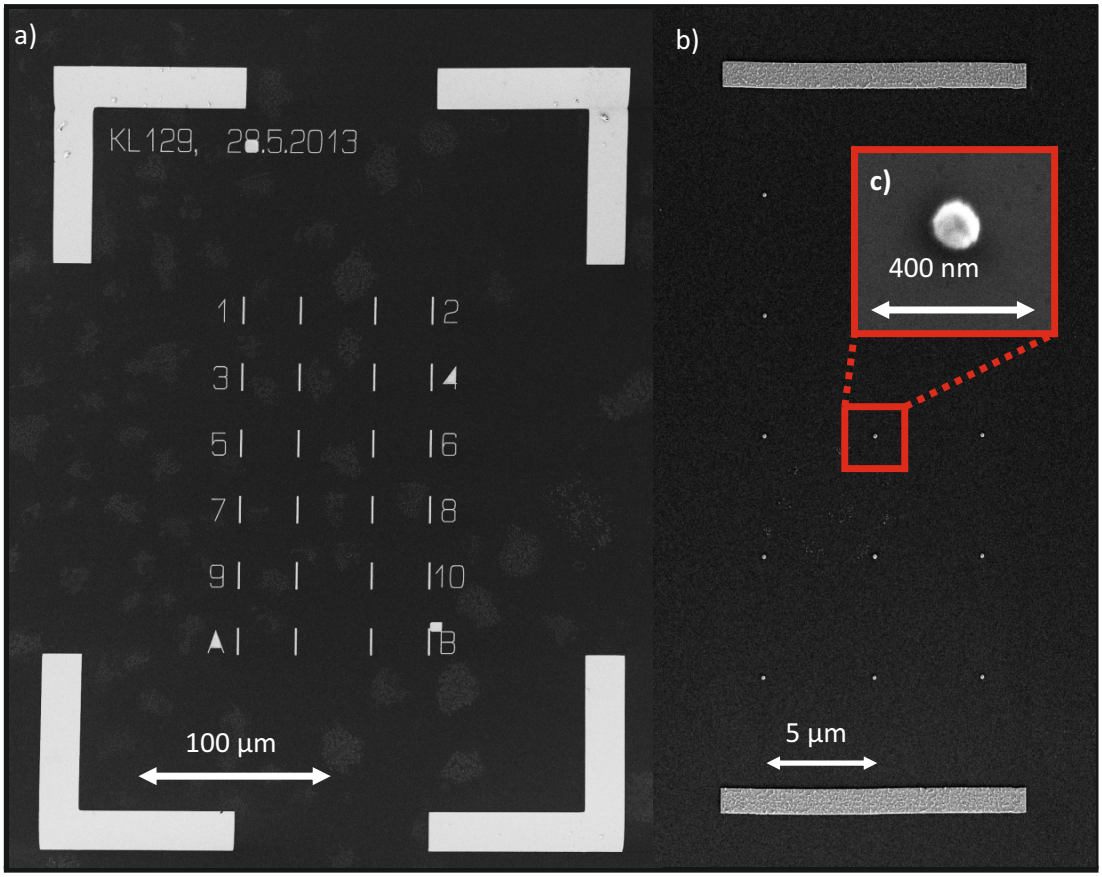

Figure 3.1 *a) SEM micrograph of sample KL129. The sample consists of gold discs of 50nm height and varying radius ranging from 25nm (field 1) to 100nm (field B). b) Closeup view of field 6 which contains gold discs of 50nm radius arranged in a $5\mu m x 5\mu m$ lattice. c) Detail view of a single gold disc with 50nm radius.*

The sample design for the nearfield measurements has different requirements. We want to have a disc array that is as dense as possible with the limitation that there should be no coupling between neighbouring discs. We want to have a high disc density for the nearfield measurements as it fascilitates the alignment process.

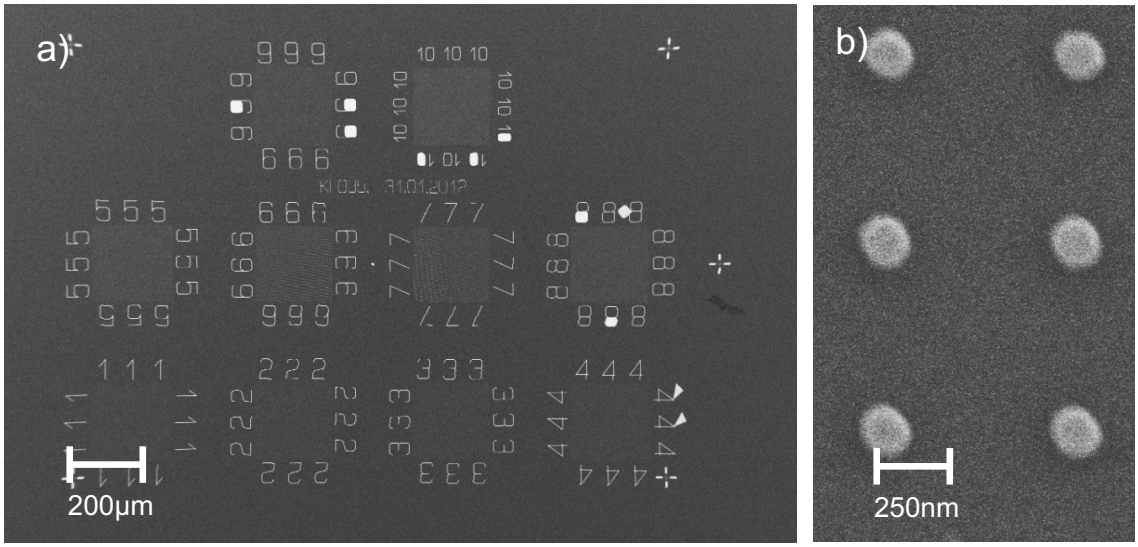

Figure 3.2 *SEM images of a typical nearfield sample. The discs are arranged in an array with $700nm$ lattice constant. a) To compensate for fabrication deviations, every sample consists of several measurement fields containing an array of gold discs with specific radii. Markers around the measurement fields fascilitate navigation on the sample.*
b) Magnified view of field 7 yields a disc diameter of 160nm.

Therefore the nearfield samples look like the one shown in figure 3.2.

3.2 Darkfield measurements

After the fabrication process we measure the linear optical properties of the samples with a darkfield microscope. This measurement is done to ensure that the gold deposited during the evaporation process was of good quality and that the fabricated discs had optical properties according to the design. Figure 3.3 shows the darkfield measurement of the sample as seen in 3.1. As expected the plasmon resonance shifts towards longer wavelength with increasing disc radius. In addition the scattering signal increases with increasing disc radius.

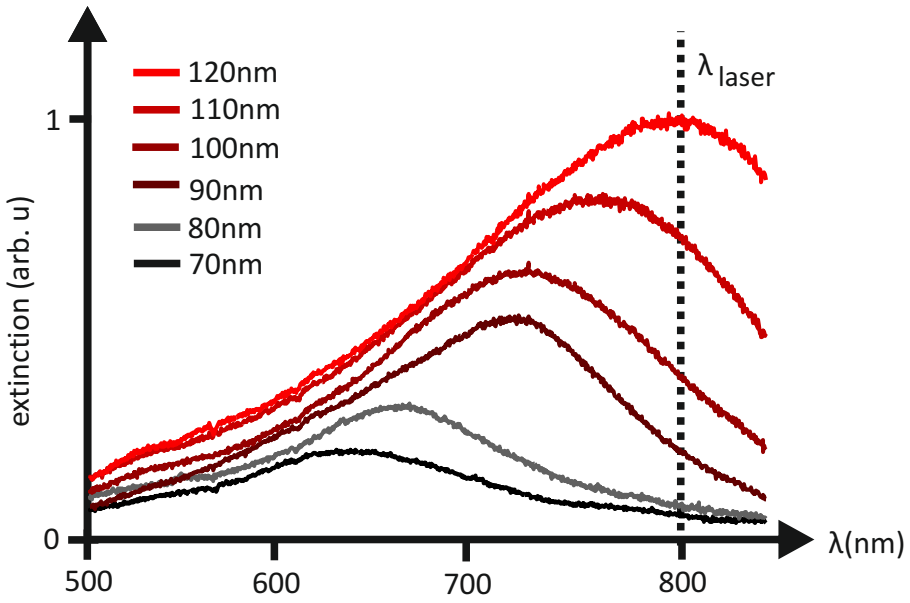

Figure 3.3 *Dark field spectra of individual gold discs of 50nm diameter and varying radius between 50nm and 100nm. The plasmon resonance shifts to longer wave length as the disc size increases. As a reference the wavelength of the laser used in the experiment is shown. The ideal disc has a steep slope in the cross section at the laser wavelength.*

3.3 Pump probe farfield setup

This section focusses on the technical realization of the farfield pump probe experiment. A simplified sketch of the experimental farfield setup is shown in figure 3.4. Ultra-short laser pulses are generated by a Titanium Sapphire oscillator (Ti:Sa) which is pumped by a solid-state Neodymium Vanadate ($ND:YVO_4$) diode laser. The pump laser natively operates at 1064nm wavelength radiation that is converted to 532nm wavelength via second harmonic generation for efficient pumping of the Ti:Sa crystal. The laser model is a Coherent Verdi V18 which is pumping a Coherent Mira 900 with 10W power at 532nm. In this configuration the Ti:Sa oscillator delivers 1.5W output power at 800nm wavelength, a pulse duration of roughly 200fs and a pulse repetition rate of 76MHz. In order to suppress parasitic reflections from the experiment which could influence the laser system, a faraday isolator is installed directly after the laser output window. The laser pulses are then split at a polarizing beam splitter (PBS). The splitting ratio is controlled via a half wave plate in front of the PBS. The PBS creates two distinct optical branches, the pump path (reflection) and the probe path (transmission).

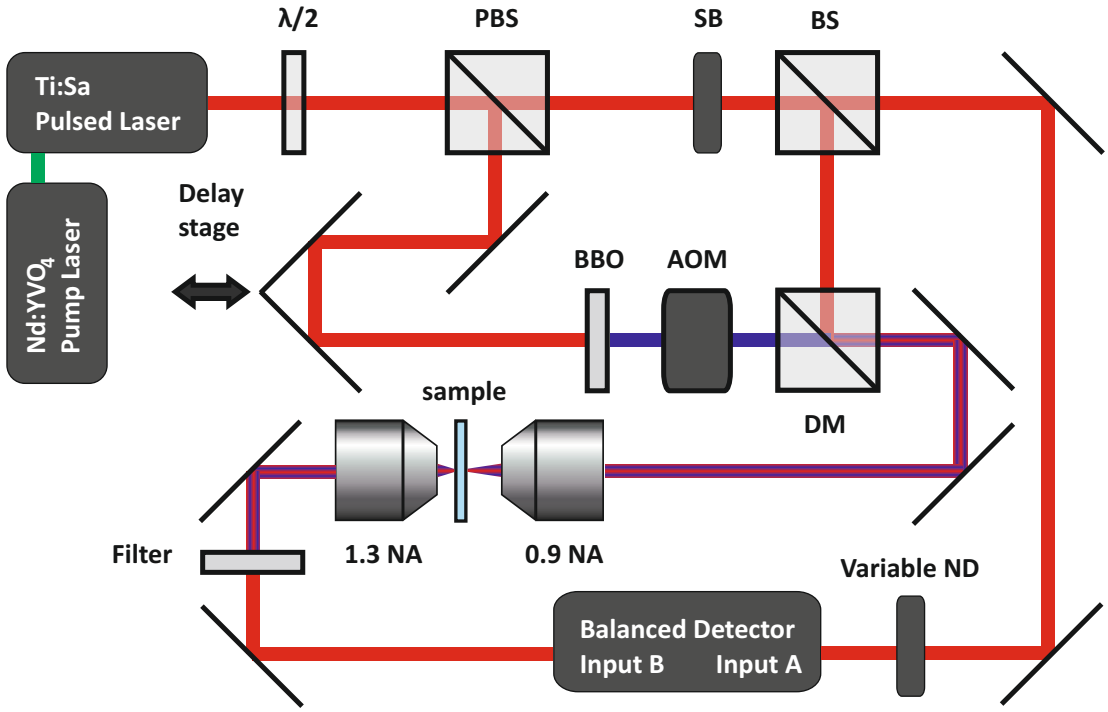

Figure 3.4 *Schematic view of the farfield pump probe setup. Laser pulses emitted by a Ti:Sa laser are split into a pump and probe arm. Pulses in the pump arm are frequency doubled and can be delayed via a retro reflector which is mounted on a motorized linear stag. The pump pulses are overlapped with the probe pulses at a dichroic mirror. The pulses are focused on the sample with 0.9NA objective and collected by a 1.3NA oil immersion objective. The pump pulses are removed from the beam path with a bandpass filter before the is collected with a balanced photo detector.*

3.3.1 Pump path

The temporal spacing between pump and probe pulse is controlled via a retro reflector that is mounted on a motorized linear stage. The motorized linear stage (Owis-Limes 150) has a travel range of 15cm which corresponds to a maximum temporal delay of pump and probe pulse of 1000ps.
In a pump probe experiment one usually has to discriminate between excitation and detection pulse either during signal acquisition or signal analysis. There are several ways to avoid crosstalk between pump and probe light in the measurement signal, such as spatial discrimination through noncollinear beam paths, separation in the frequency domain via modulation-demodulation technique or spectral separation by using filters. In this experiment we choose to separate the pump and probe pulse spectrally. This is achieved by frequency doubling the pump pulse with a phase matched Beta-Bariumborate crystal (BBO) resulting in pulses of 400nm wavelength . A dielectric shortpassfilter (AHF Brighline 390/18) after the BBO suppresses the remaining fundamental light. The pump light passes an acoustic opti-

cal modulator (AOM) that is driven by a function generator with a square wave at 22.5kHz. The stimulated grating created in the AOM results in a diffraction pattern of the transmitted pump beam. The first order of the diffraction pattern is isolated with an aperture and then passes a lens pair with central pinhole in order to clean up the spatial mode of the pump light before it is overlapped with the probe light on the Dichroic Mirror (DM).

3.3.2 Probe branch

Light in the probepath passes a Soleil-Babinet compensator (SB) which allows for precise control of the polarization state. A part of the probe light is then sampled by a beam splitter and passed onto input A of a balanced photo detector (Femto - OE100). A variable ND Filter in front of input A allows to match the incident light power on input A to input B. Pulses reflected on the BS are guided to the DM where they are overlapped with the pump pulses.

3.3.3 Microscope

The microscope assembly consists of two objectives for focussing on the sample and recollimation of the light. The sample is mounted on a piezo stage (Piezo Jena) for fine positioning. The piezo stage itself is mounted on three linear stages for coarse positioning tasks. Pump and probe pulse are focussed on the sample by a 0.9NA objective (Olympus MplanFL (N) 100x/0.90 BD P). The slight focus shift between pump ($400nm$) and probe pulse ($800nm$) due to chromatic abberations of the objective can be compensated by adjusting the recollimation of the pump pulse after the pinhole in the pump branch. The focussed light passes the sample and is collected by a 1.3NA oil immersion objective (Olympus). The collected light is then filtered by a bandpassfilter (Versachrome HC 796/12) that transmits more than 90% of probe light and attenuates the pump light by a factor of 10^6. The remaining probe light is then registered by input B of the balanced photo detector.
Using a balanced photoreceiver with equal optical power for both diodes of input A and B reduces a common mode signal such as laser noise which is present on both optical paths. The difference signal ($A - B$) is amplified by a variable gain factor (typically between 10^6 and 10^7) and then fed to a Lock-In Amplifier (Stanford Research 830). The reference signal for the Lock-In Amplifier is given by the function generator that drives the AOM in the pump branch. The measurement signals are recorded by an ADwin Box that also synchronizes measurement events. A labview measurement program allows to comfortably control the setup.

3.4 Apertureless Scanning Nearfield Optical Microscope

The last section introduced the first ingredient necessary to build a time resolved nearfield microscope, namely the pump probe measurement scheme which enables one to resolve processes on very short time scales. Being a farfield technique however, one is diffraction limited and thus cannot distinguish between objects that are less than $\frac{\lambda}{2}$ apart [42]. By introducing a local probe, nearfield microscopy circumvents the diffraction limit, offering resolution that can be many times higher than the wavelength of the probe light [41]. This section introduces our realization of an aSNOM that offers spatial resolution of 20nm and defines the basis of the time resolved nearfield microscope. The design of the aSNOM used in this project is based on work that has been done by Ralf Vogelgesang and coworkers [20].

Being a technique that relies on the interaction of a local probe and optical nearfields, precise distance control on the nanometer scale of the tip-sample surface is of crucial importance for a nearfield microscope. This distance control is usually established by an atomic force microscope (AFM). During our experiments, we used a commercially available Parkscientific M5 Model. Although that particular model is rather old, it features good optical access to the tip region, a quality that is absent from many newer AFM models. An overview of the aSNOM can be seen in figure 3.5. In order to detect amplitude and phase of the optical signals, an interferometric detection scheme is used. Light emitted by a Ti:Sa-Laser (Coherent Mira 900) is guided to the setup via a single mode fiber. The single mode fiber allows a flexible positioning of the laser system with respect to the nearfield microscope. Furthermore the single mode fiber decouples the nearfield microscope from the laser system in order to suppress signal variations caused by thermal drifts on the laser table. The beam is recollimated after the fiber and is then split up by the beam splitter BS 1 into a signal arm and a reference arm. The reference arm consists of a retroreflector that is mounted on a piezo driven delay stage. This allows to control the optical path length with a few nanometer precision which is necessary in order to perform homodyne measurements that yield the amplitude and the phase of the optical signals. The intensity of the reference light can be controlled with a variable ND Filter. The reference light is then overlapped with the signal at BS 3.
Light in the signal arm is polarized in the sample plane, reflected by BS 2 and then focussed onto the sample by a 0.28 NA objective (Mitutoyo 10X MPlan APO Infinity-Corrected Long Working Distance Objective).
The oscillating AFM tip scatters local nearfields and modulates the scattered light with the cantilever frequency and higher harmonics of it. The scattered light is collected by the illumination optics, transmitted by BS 2 and then overlapped with the reference light. The polarization of the light hitting the detector (Hamamatsu Si APD S2384, Femto HCA-S-200M-Si) is controlled with a polarizer after BS 2. A single mode fiber in front of the APD is used as a mode filter which only transmits

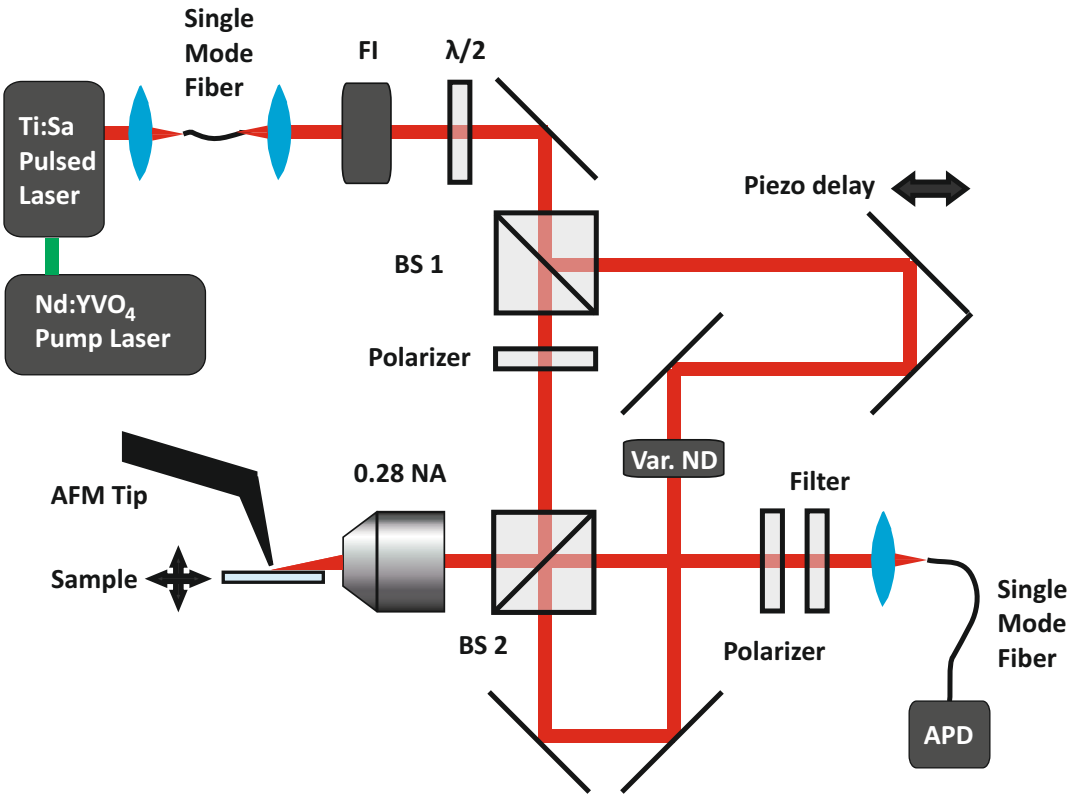

Figure 3.5 *Scheme of the experimental setup. S-polarized light is focussed on the sample. The backscattered light is modulated by the tip oscillation and analyzed for its polarization in a cross-polarization scheme. The signal is interferometrically amplified before it is sent to a detector. Between the laser system and the nearfield microscope a single mode fiber is used in order to minimize the influence of beam deviations caused by thermal drifts. A single mode fiber in front of the APD acts as mode filter.*

the TEM_{00} mode. The light is coupled into the detector fiber with an achromatic doublet (f=30mm). The effective field of view of the Mitutoyo objective is approximately $5\mu m$ in this configuration. Furthermore the fiber aperture acts as a spatial filter. The detector signal is fed to a Lock-In Amplifier that demodulates the signal on the cantilever frequency or higher harmonics of it. The reference signal is derived from the deflection signal of the AFM feedback. The deflection signal is directly proportional to the cantilever oscillation frequency. The Lock-In signal is fed into a PC-Interface. A measurement software written by R. Vogelgesang controls and synchronises the measurements.

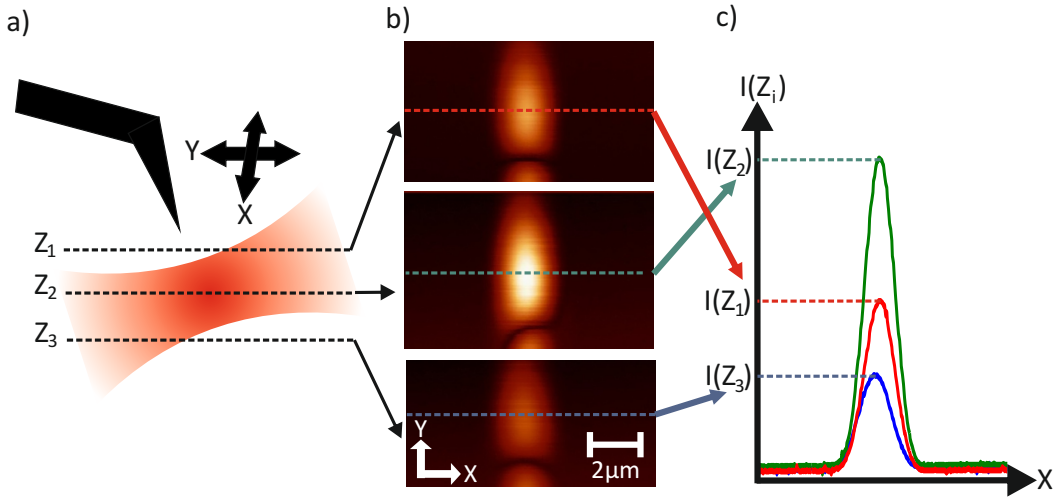

Figure 3.6 *a) The AFM tip is scanned laterally through the focus at different height Z_i. b)The recorded intensity distribution resembles a plane in the focus volume. c) Evaluating for the maximum intensity yields the ideal position for the AFM tip*

3.5 Alignment procedure

The positioning of the tip in the excitation focus is of utmost importance. In this section the aligment procedure of the nearfield microscope will be described. During the alignment, the tip has to be moved into the excitation focus. For this alignement step, the reference beam is blocked and the polarizer in the excitation path is opened by 10°. After coarse tip positioning in which the geometric shadow of the tip after the focus is observed, the fine adjustement is done via the 3D piezo scanner that is included in the AFM Head. It has a travel range of $100\mu m$ in the sample plane and up to $3mm$ perpendicular to the sample plane. For prescise height control, the AFM Head also has a piezo which has a travelrange of $6\mu m$. However the height control piezo is not used in the tip alignement. During the fine positioning of the tip in the illumination focus, the tip is scanned laterally through the focus (see figure 3.6) and the scattered signal of the tip demodulated at the fundamental cantilever frequency is recorded. This is done for several heights Z until the maximum backscattering signal is detected. Through this method the tip can be positioned in the focus with a very high accuracy. This is crucial because a deviation from the optimal position not only affects the excitation of the sample structure underneath the tip, but it also decreases the detection efficiency.

In the next step we want to minimize the back reflection of the AFM tip by establishing the cross polarization. Therefore the reference beam is switched on and the amplitude and the phase of the demodulated scattering signal are measured in dependence of both polarizer and analyzer angle. As can be seen in figure 3.8 the homodyne amplitude shows a minimum at angles that deviates from the nominal cross polarization position of 0° and 90° for polarizer and analyzer. This deviation

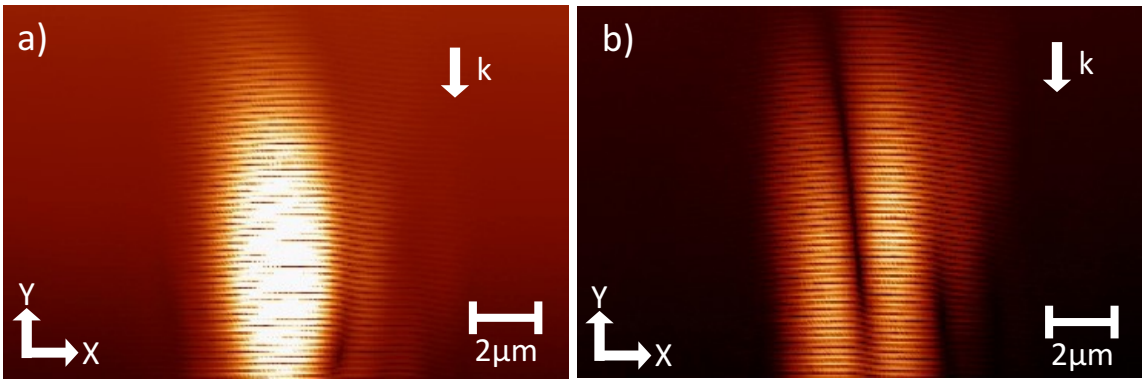

Figure 3.7 *Comparison of an interferometrically detected tip scan a) before and b) after establishing crosspolarization. As the tip scans the y-direction, the path difference between the two interferometer arms is changed and therefore fringes are recorded.*
b) shows an area of zero backscattering, that is extended in the beam direction.

can have many reasons e.g. imperfections in the optical alignement, tilted mounting of the AFM tip, asymmetric shape of the AFM tip or wrong calibration of the polarizer angles. Apart from the minimum in optical amplitude, the more important criterium for the alignement performance is the existance of a phase singularity in the optical amplitude. In this polarizer configuration the backscattering of the tip is maximally suppressed and should vanish in the ideal case [20]. Figure 3.7 shows a comparison between a focus scan with reference switched on before and after crosspolarization has been established. The two main differences between the two scans are the drastically lower intensity in the crosspolarized case and the existance of a region where the backscattering of the tip vanishes. The overall reduced scattering intensity is caused by a minimization of tip excitation whereas the zero scattering zone is a direct consequence of the cross polarized state. Having established crosspolarization, the alignement is now complete. In order to record nearfields the sample is now scanned underneath the tip while simultaneously recording the homodyne amplitude and phase.

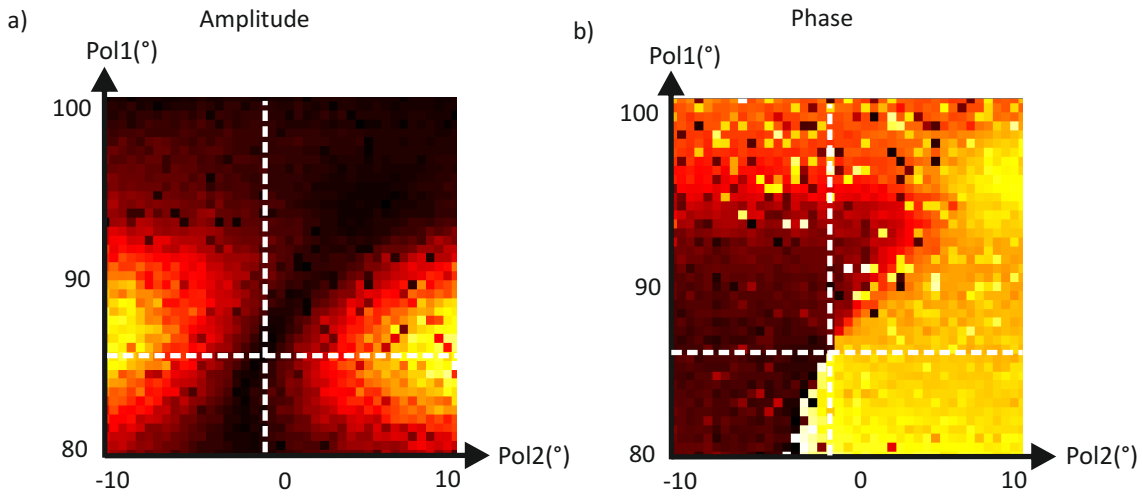

Figure 3.8 *Optical amplitude (a)) and optical phase (b)) are shown for a polarizer scan that is used to determine the crosspolarization configuration. The Polarizer (horizontal axis) and analyzer (vertical axis) are scanned around the nominal cross-polarization position* $0°/90°$*. The crossing of the dashed curves marks the position of the crosspolarization*

3.6 Pump Probe Apertureless Scanning Nearfield Optical Microscope

The last section of this chapter describes the combination of the pump probe scheme introduced in section 3.3 with the aSNOM that was discussed in section 3.4. The goal of the experiment is to demonstrate the combination of temporal resolution of 100fs and a spatial resolution of 20nm in one device. A schematic overview of our implementation of a ppaSNOM is given in figure 3.9.

The ppaSNOM is basically an aSNOM that is extended by a pump arm. Pulses of 800nm center wavelength are emitted by a titanium sapphire laser (Coherent Mira 900), travel through a Faraday isolator (FI) and are then divided by a PBS. The splitting ratio of the PBS can be controlled by a $\frac{\lambda}{2}$ plate that is installed after the FI. Pulses transmitted by the PBS end up in the pump branch where they travel over mechanical delay stage (Physik Instrumente M531.DG) that has a travel range of $30cm$ and therefore allows a maximum delay of up to 2000ps. After the delaystage the pulses are focussed on a phase matched BBO that allows for efficient second harmonic generation. The fundamental light is filtered out by a bandpass filter (AHF 402/15 ET). The remaining blue light is modulated by a chopper (Newfocus model 3501) at a frequency of 6kHZ. The chopped light then passes a steering mirror and is then focussed by 0.25NA substrate corrected aspheric lens onto the sample structures.
Light that is reflected of the PBS directly enters the aSNOM introduced in section 3. The working principle is very similar to a continous wave aSNOM.

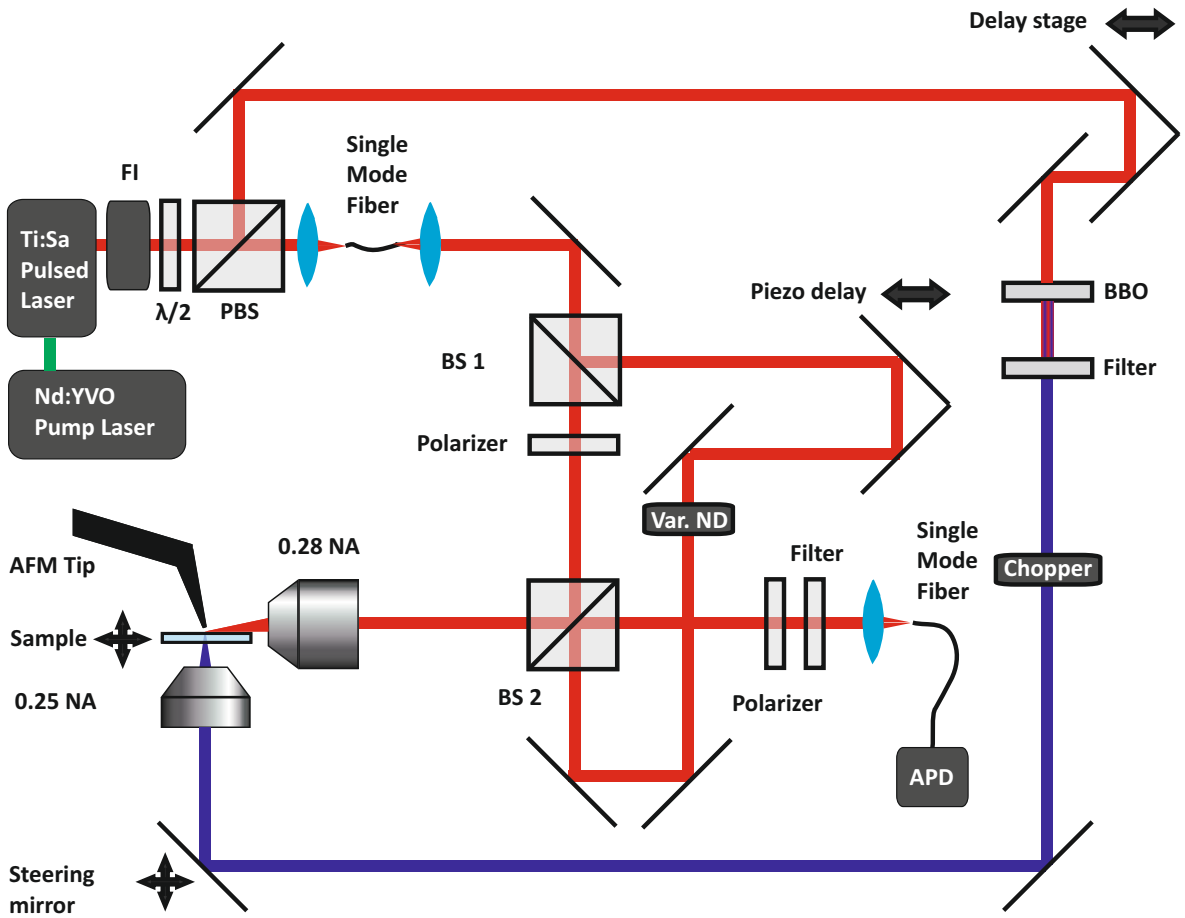

Figure 3.9 *A PBS divides the setup into pump and probe arm. The frequency doubled pumplight can be delayed via a motorised linear stage. Special care has to be taken in the probe arm as the laser pulses restrict the path difference in the Mach-Zehnder Interferometer to the coherence length.*

3.6.1 Differences to the aSNOM

Using pulses in the aSNOM adds an additional requirement to the setup. Being an interferometric measurement technique the path length of signal and reference arm have to be equal within the coherence length of the laser. The coherence length of a laser pulse can be derived as [43]

$$L = \frac{2ln2}{\pi n}\frac{\lambda^2}{\Delta\lambda}$$

where L is the pathdifference between two pulses at which the fringe visibility is reduced by a factor of two, n is the refractive index of the medium, $\Delta\lambda$ is the spectral width and λ the center wavelength of the pulse [43]. The pulses of our laser system have a spectral width of about 5nm at a center wavelength of 800nm which results in a coherence length of roughly $50\mu m$.

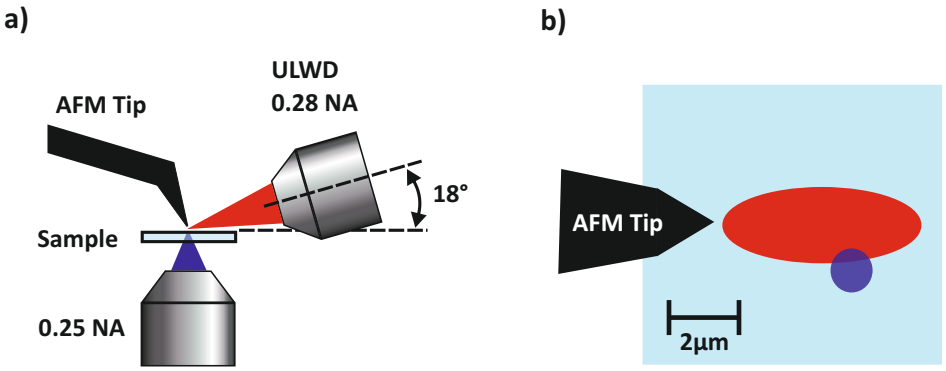

Figure 3.10 *Magnified view of the tip/focus area in a side perspective a) and in birds view b) In a successful ppaSNOM alignement, pump and probe beam overlap. In addiation the tip has to be in the focus and a sample structure has to be excited.*

Figure 3.10 illustrates the optical paths in the sample region of our ppaSNOM setup. Due to spatial restrictions the probe beam impinges on the sample at an angle of 18°. The pump focus is perpendicular to the samplesurface. With top and bottom objective having an NA of 0.28 and 0.25, and being used with 800nm and 400nm light respectively, the diffraction limited focii have diameters of about $3.5\mu m$ and $2\mu m$. The focii of both pump and probe have to overlap in three dimensions. Because the probe focus has to stay fixed in space for the nearfield operation, the pump focus has to be steered over the probe focus. We therefore installed motorized slipstick mirrors (Newport Agilis LS11) before the pump path aspheric lens. Furthermore, a slipstick linear stage can move the aspheric lens perpendicular to the sample plane. These are the three degrees of freedom necessary to overlap the pump with the probe beam. A description of how pump and probe focus are aligned in this configuration is given in section 6.1.

3.7 Conclusion

In order to construct a device that combines 1ps temporal resolution and 20nm spatial resolution in an all optical measurement technique, two experimental techniques are combined. The temporal resolution stems from the utilization of the pump probe measurement scheme. The pump probe scheme is combined with a nearfield microscopy technique that records the scattering signal of a sharp AFM tip which is probing the sample surface. The aSNOM measures amplitude and phase of the z-component of the nearfield with a lateral resolution of 20nm. The technology chapter furthermore describes the alignment process that is used to position an AFM tip in the focus of an objective. The sample system which consists of top down fabricated gold nano discs sitting on a glass substrate is introduced.

The disc dimensions are chosen such that they exhibit a dipolar plasmon resonance when excited with 800nm light. The gold nano discs are a favourable sample system as they are chemically inert, are well studied and exhibit a big optical response under the influence of an external driving field.

CHAPTER 4

Mechanical oscillations of gold nano discs

As a precursor for the time resolved nearfield measurements, the interactions of a laser pulse in the 100fs regime with a metallic nano particle are studied during this thesis. In general the energy deposited by a pulse is distributed over many different processes that happen on a wide range of time scales [44–47]. The interaction can be split into two main phenomena which originate from the interaction of the laser pulse with conduction electrons on the one hand, and a second contribution which stems from the rapid heating of the lattice through the hot electron gas. The first process happens on a sub-picosecond time scale and has been studied by numerous groups [48, 49]. This thesis focusses on the cooling process of a rapidly heated metal particle and the associated acoustic vibrations [50, 51] which cause a time dependent variation of the optical properties.

A schematic representation of the excitation and relaxation processes of a metal particle is shown in figure 4.1. A coherent oscillation of the conduction band electrons is excited by a pulse. The oscillation dephases on a time scale of 10fs leaving an incoherent hot electron gas behind [46, 47]. Within a timescale of a few hundred fs the excited electrons thermalize with the rest of the electron distribution via electron-electron scattering. The hot electron distribution now thermalizes with the lattice in less than $1ps$ via electron-phonon interaction. Because the lattice is forced to expand at a rate that is higher than the speed of sound in the material, the lattice overshoots its equilibrium position [52]. The lattice expansion is further enforced by the increased pressure of the rapidly heated electron gas [53] which leads to an additional force on the particle boundaries. The rapid lattice heating has the same effect on the metal particle as a hammer that is striking a bell, resulting in a ringing particle. The interplay between electron pressure and lattice heating determines the starting phase of the mechanical oscillation. The vibration frequency of the particle

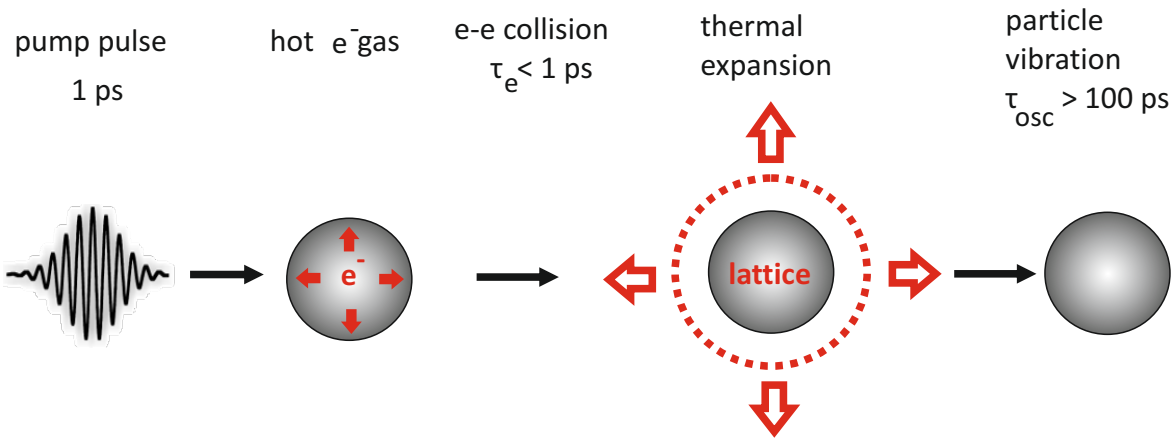

Figure 4.1 *Interaction of a short pump pulse with a metal particle: The electron gas absorbs a portion of the pump pulse leading to an increase in electron temperature. The electron gas thermalizes via electron-phonon scattering with the lattice on a time scale less than $1ps$. The rapid heating process causes the lattice to expand at a velocity that is higher than the speed of sound ν in the material which results in an overshooting its equilibrium state. This leads to acoustic oscillations of the particle. The acoustic oscillations decay through thermal conduction to the environment on a time scale that is dependant on the size. The vibration frequency $\omega_{vib} \propto \frac{\nu}{d}$ where d is the particle diameter.*

is dependent on the elastomechanical properties such as density, young's modulus and poisson ratio as well as the particle size and shape. Typical vibration frequencies for 100nm sized particles are on the order of tens of GHz [51].

4.1 Mechanical vibration model

As the lattice is overshooting its equilibrium position after being heated by a pulse the particle starts to expand and contract periodically. In order to derive the vibration frequency ω_{vib} one has to solve the elastodynamic wave equation. For spheres this equation was solved by Lamb [54]. Starting from the Navier equation

$$\nu_L^2 \vec{\nabla} \cdot (\vec{\nabla} \cdot \vec{u})) - \nu_T^2 \vec{\nabla} \times (\vec{\nabla} \times \vec{u}) = \omega^2 \vec{u} \tag{4.1}$$

with $\nu_{L,T}$ being the longitudinal and transversal velocity of sound in the medium and u being the displacement vector. In a spherical coordinate system by making the ansatz $u(r,t) = u(r) \cdot e^{-i\omega t}$ and introducing

$$\begin{aligned} \vec{\Lambda} &= \vec{\Delta} \cdot \vec{u} \\ \vec{\Gamma} &= \vec{\Delta} \times \vec{u} \end{aligned} \tag{4.2}$$

the following relation for the displacement field can be derived [55]

$$\vec{u} = -\Delta(\frac{\Lambda}{q^2}) + \frac{1}{Q^2}\vec{\Delta} \times \vec{\Gamma} \tag{4.3}$$

where $q = \frac{\omega^2}{\nu_T^2}$ and $Q = \frac{\omega^2}{\nu_L^2}$. For the boundary condition of no force on the particle surface, e.g. a sphere in vaccuum, the solutions for a angular momentum $l = 0$ and $l \neq 0$ are

$$l = 0 : tan(qa) = \eta_L(1 - \frac{\nu_L^2}{4\nu_T^2}(qa)^2)^{-1} \tag{4.4}$$

and

$$\begin{aligned} l = 1 : &- \frac{(Qa)^2}{2}(2l^2 - l - 1 - \frac{(Qa)^2}{2})j_l(qa)j_l(Qa) + \\ &(l^3 + 2l^2 - l - 2 - (Qa)^2)qaj_{l+1}(qa)j_l(Qa) + \\ &(l^3 + l^2 - 2l - \frac{(Qa)^2}{2})Qaj_l(qA)j_{l+1}(Qa) + \\ &(2 - l^2 - l)(Qa)(qa)j_{l+1}(qa)j_l(Qa) = 0 \end{aligned} \tag{4.5}$$

where a is the sphere radius. Equation 4.4 and 4.5 can be solved numerically and therefore values for the oscillation period T_i can be derived. We can write

$$T_i = \frac{2\pi \cdot a}{S_i \cdot \nu_L} \tag{4.6}$$

with $T_i(a)$ being the oscillation period, a being the particle diameter and $S_i = 2q_i a$. Unfortunately Lamb's theory can only be applied to spherical particles in vacuum or particles which are embedded in homogeneous media. This however doesn't resemble the sample structure, which consists of a gold disc sitting on a glass substrate, that we use in our measurements. Therefore, in order to predict the elastomechanical behaviour, we have to employ FEM simulations. In the next section we will introduce our FEM model and compare it against Lamb's theory.

4.2 Comsol modeling

The modelling of the mechanical properties of nano sized metal discs is done with Comsol Multi Physics[56], which is a FEM based program. To justify the usage of Comsol, the elastomechanical properties, specifically the evolution of the oscillation period T with radius a, of a gold sphere in vaccuum is simulated and compared to the solution given by [54]. To retrieve the dependence of the oscillation period T_1 the eigenmodes of a sphere octant are calculated. The sphere octant is chosen as a basis as it fascilitates the retrieval of symmetric eigenmodes. In order to narrow down the FEM solutions, the displacement of the sphere center is set to 0 and dis-

placement normal to the radial direction is prohibited. The eigenfrequency of the radial breathing mode for a given sphere radius a is then extracted from the Comsol solutions. A comparison of Comsol simulation and the Lamb solution for the first order breathing mode of equation 4.4 is shown in figure 4.2 .

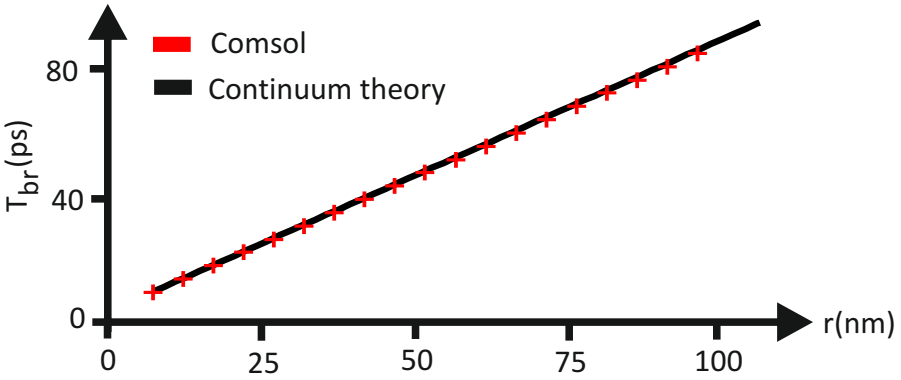

Figure 4.2 *Evolution of the oscillation period T_1 of the first order breathing mode of a goldsphere with radius r in vacuum calculated from the navier equation(black) and comsol(red). The scaling parameter for the first order breathing mode as derived from equation 4.4 is $S_1 = 2.954$*

The comsol results agree very well with Lamb's theory. In addition Comsol allows to simulate different structure types which is why we use it as the standard modeling tool for the elastomechanical properties of metal particles throughout this work. To model the transient volume change in Comsol, a gold disc of 50nm height and variable radius is placed on a half sphere made out of silica glass. As a boundary condition, displacement normal to the gold-glass interface is prohibited. To model the lattice expansion that occurs 1ps after the excitation through a pump pulse, the initial displacement values for the disc at $t = 0$ were set to $[uvw] = 10^{-3} \cdot [xyz]$ thereby mimicking an expanded disc structure. The half sphere of silica glass was assumed to have no prescribed displacement at $t = 0$. In order to incorporate modal damping, an effective damping parameter, the rayleigh damping parameter, has to be chosen. The Rayleigh damping parameter is a concept of solid mechanics that tries to approximate the frequency dispersion of the damping parameter through a parabola that is determined by the damping coefficients of two dominant modes, typically on the lower and upper boundary of the frequency spectrum [57]. The Rayleigh damping parameter is defined as

$$\Sigma = \frac{\alpha}{2\omega} + \frac{\beta\omega}{2} \tag{4.7}$$

were α and β are the damping coefficients of the two respective modes and ω is the frequency. α and β have to be chosen carefully because modes outside the fre-

quency interval of ω_α and ω_β are strongly damped [57]. For the simulation the Rayleigh damping parameter was chosen such that the lifetime of the oscillation matches the experimental results. The experimentally determined lifetimes are on the order of 600ps. This yields $\alpha = 10^{11}\frac{1}{s}$ and $\beta = 10^{-10}s$. The mechanical properties of gold were assumed with a young's modulus of 70GPa, and a Poisson's ratio of 0.40 which lies within the value range that can be found in literature [58]. Via the indirect MUMPS solver [59], the temporal evolution of the mechanically destabilized system is calculated in time increments of 200fs. Snapshots of the total displacement of the gold disc are shown in figure 4.3 .

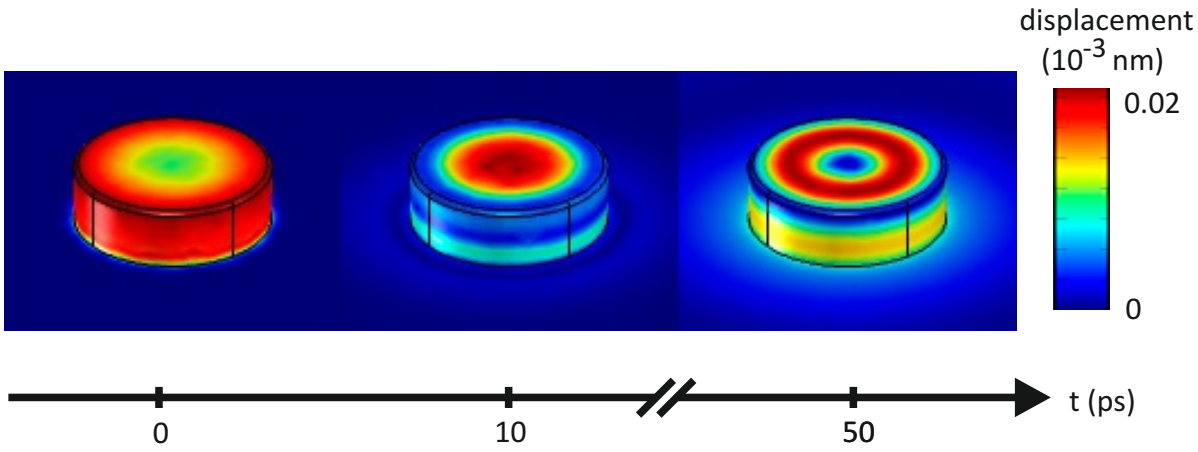

Figure 4.3 *Modelling the elastomechanical response of a gold disc to an instantaneous temperature increase is done by assuming a linear diplacement $[u, v, w]$ along the axis $[xyz]$. The temporal evolution shows the formation of the characteristic breathing mode.*

In the next step the time dependent volume change of the gold disc is calculated via surface integration over the disc surface S of the displacement (u,v,w)

$$\Delta V = \int\int (u, v, w) \cdot \delta S \tag{4.8}$$

An example data set for a gold disc of 50nm height and 70nm radius is shown in figure 4.4. After a steep drop an oscillation of ΔV sets in. The data set is cut to times bigger than t_{cutoff} to isolate the oscillatory part of the trace. The fourier transformation yields a dominant fundamental mode at around 15GHz. This Comsol model allows to calculate the frequency evolution of the fundamental breathing mode for various disc sizes. In a next step we compare the theoretical findings to measurements (see section 4.3).

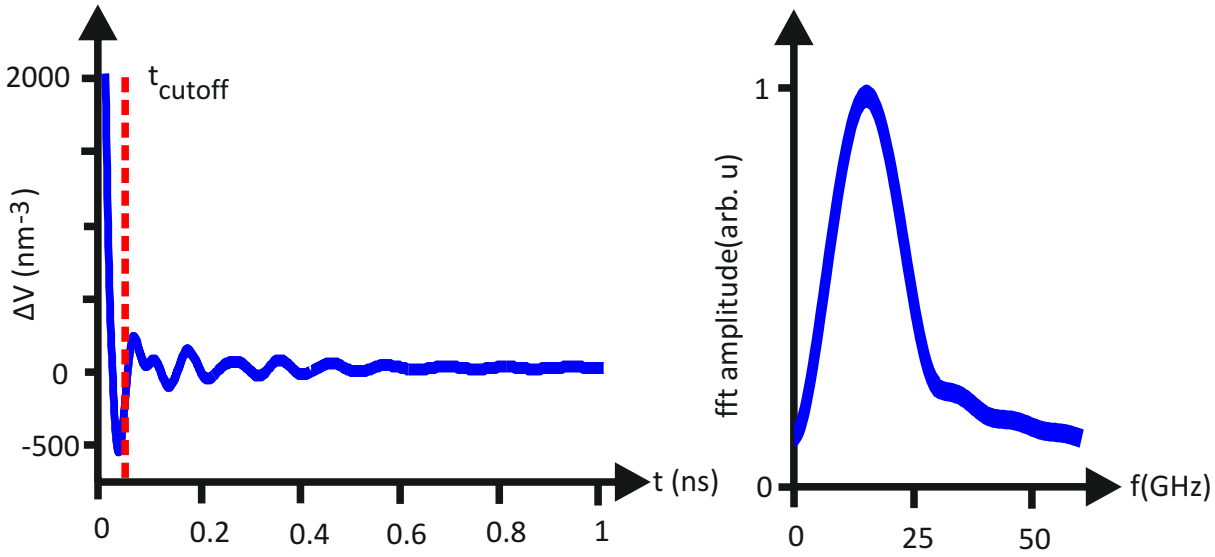

Figure 4.4 *Timedependent volume change ΔV extracted from the Comsol data. After t_{cutoff} a harmonic oscillation consisting of two modes sets in. In order to separate the eigenmodes from the steep drop at the beginning of the trace, the FFT is done for times > t_{cutoff}. The fundamental mode has a frequency of 15GHz and decays within several hundred picoseconds. The second mode has a frequency of 32GHz and is strongly damped.*

4.3 Transient Farfield Absorption

To measure the transient response of individual gold discs the sample is positioned in a confocal microscope. For all measurements shown the pump wavelength λ_{pump} is set to 400nm and the pulse energy is $p_{pulse} = 100pJ$. The probe wavelength λ_{probe} is set to a wavelength where we expect to see the maximum differential signal according to calculations shown in 2.6. Pump and probe pulse are overlapped with the aid of an attached microscope camera. A 2D map of the absorption signal of the probe beam is then measured. This allows to precisely position an individual gold disc in the probe focus. In a next step the transient absorption signal is measured and maximised by adjusting the pump beam position on the sample. Finally the delay between pump and probe pulse is varied with a delay stage. A representative measurement is shown in figure 4.5 a). The raw data shows a spike of the transient transmission when probe and pump pulse overlap at $t = 0$. This spike is caused by the increased absorption of the hot electron gas. A few picoseconds later the particle starts to oscillate. Note that the signal is offset by a thermal background signal. The blue dashed curve represents the equilibrium value of the oscillation trace and stems from the overall temperature increase of the particle. In order to gain information about the mechanical oscillation frequency a two step manipulation of the data has to be applied. In a first step the DC temperature component represented by the blue dashed curve has to be substracted from the data. In the second step

the oscillation is separated from the electron spike by neglecting the data up until 10ps after the spike has occurred. The grey box in figure 4.5 a) represents the data points that are used to retrieve the eigenfrequencies. The FFT of the isolated oscillation trace is shown in figure 4.5 b). One clear peak at around 15GHz is visible. Through comparison to comsol simulations we can attribute this peak to the first order breathing mode. The frequency components below 15GHz are the result of a residual thermal offset which isn't fully suppressed through the data preparation as described before.

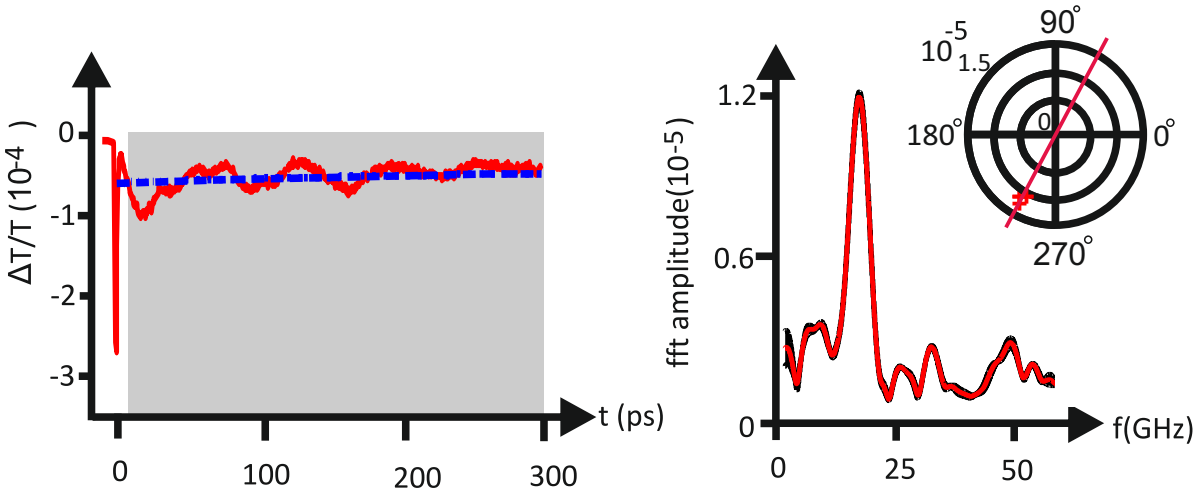

Figure 4.5 *a) Transient transmission signal of a single gold nano disc of 140nm diameter and 50nm height. At $t = 0$ the increased absorption of the hot electron gas leads to a peak in the signal. The rapid transfer of energy to the lattice results in mechanical vibrations that have a period of 70ps. Before the eigenfrequencies of the oscillation can be retrieved, the data has to be prepared by substracting the thermal background and cutting away the electron spike at t=0. b) Fourier transformation of the oscillatory part of the delay trace. The red curve shows a dominant peak at $15GHz$ which corresponds to the frequency of first order breathing mode. The black curve is the standard deviation as calculated from five consecutive measurements. Inset: complex valued FFT amplitude. Because the excitation is phase stable a sign can be attributed to the FFT amplitude.*

Careful data evaluation of the pump probe delay traces allow to retrieve the mechanical eigenfrequencies of oscillating nano particles. This method has been used to study the eigenfrequencies of individual gold discs on the sample shown in figure 3.1. For this study the transient transmission signal was recorded for discs with a radius between 50nm and 100nm. The oscillation frequency and the mean deviation of the fundamental mode are extracted for each disc radius. For better visualization all frequencies are converted into their corresponding oscillation periods T. The results of the measurement are plotted in figure 4.6. In addition the Comsol prediction is shown as well. The simulation data and measurement data show oscillation periods between 50ps and 110ps corresponding to oscillation fre-

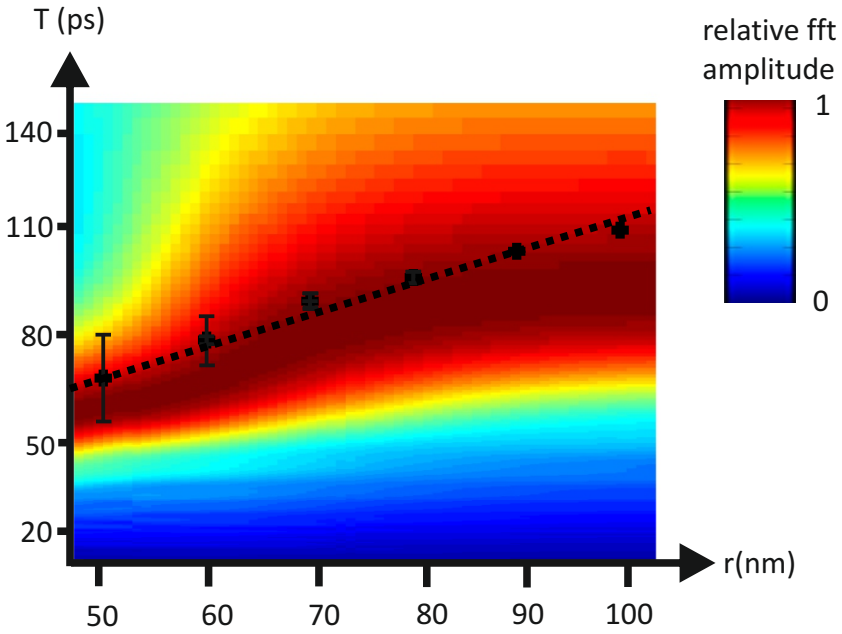

Figure 4.6 *Evolution of the oscillation period T of a gold disc of 50nm height in dependence of the disc radius r as measured (black crosses). The errorbar for the measured values increases with decreasing disc radius r. This behaviour is caused due to the decreasing spectral overlap between probe pulse and plasmon resonance (compare figure 3.3) which causes a decrease in signal magnitude. The measured curve shows a linear relation between radius and oscillation period. A straight line has been fitted to the data points. For better visualization the comsol data for each disc radius is divided by the maximum FFT amplitude for that disc. The dark red color denotes the respective maximum fft amplitude for each disc radius. The comsol data shows a deviation from the linear relation between disc radius and oscillation period indicating that the oscillation eigenmode is changing. In general all measurement values have a higher oscillation period as predicted which could be caused by imperfect fabrication compared to the design structures regarding size and shape.*

quencys from 9GHz to 20Ghz. The measurement data shows a linear relation $T \propto$ and is offset by 15ps compared to the simulation data. One possible reason could be that the sample structure is a little bit bigger than the design size which would shift oscillation periods to higher values. In addition the correct modeling of the gold glass interface and the influence of the gold-glass interface is unknown. Overall the Comsol simulation and the measurement agree quite well. By attributing the eigenfrequency to the fundamental drum mode, the relation between oscillation period T and disc radius r becomes [60]

$$T = 4 \cdot \frac{r}{\nu} \tag{4.9}$$

where ν is the speed of sound. Evaluating the fitted line in figure 4.6 yields a speed

of sound in gold of $\nu = 3740\frac{m}{s}$ which is in good agreement with the literature [61].

4.4 Spectral dependence of the transient absorption

Next we measure the transient absorption signal in dependence of λ_{probe}. The tuning range of the laser system (APE OPO) ranges from 500nm to 750nm. The probe pulses are circularly polarized to average over all polarization angles. The pump pulses have a wavelength of 400nm and are linearly polarized. The time averaged pump power is 80 μW. The wavelength is tuned in 15nm steps and for each wavelength the nonlinear signal is maximised by careful alignment of pump focus, probe focus and the sample position. Then five delay traces are recorded. The maximum oscillation amplitude at the fundamental mode as well as the phase are extracted from the fourier spectrum of the oscillatory part of the delay trace. Figure 4.7 a) shows the wavelength dependent oscillation amplitude of a disc with 50nm radius. The nonlinear response changes sign at the plasmon resonance. The dispersive lineshape as predicted by T-Matrix calculations matches the measurement data reasonably well. For visualization purposes, the T-Matrix simulation is scaled with a factor of 10^{-2}. The discrepancy between the magnitude of the differential response as calculated and as measured could be caused by the omission of the Gold d-band absorption which would alter the excitation kinetics. Nevertheless the T-Matrix simulation predicts the spectral position of the dispersive line shape well. Figure 4.7 b) shows the polar plot of the corresponding measurement evaluated at the fundamental oscillation frequency of 16GHz.

4.5 Maximising the transient nearfield response

In apertureless scanning optical nearfield microscopy signals are usually very weak. In our proof of principle measurement we try to measure a perturbation of the nearfield signal caused by the mechanical oscillation of the particle. Because the nearfield signal itself is rather weak, we need to optimize every aspect of our experiment in order to be able to detect a pump induced perturbation of the nearfield signal. The spectral properties of metal nano particles are strongly dependent on the particle size (see figure 3.3). The requirements for a sample that facilitates the demonstration a time resolved nearfield microscope are contradictory. On the one hand the nearfield should be maximised to have a high quality carrier signal and on the other hand we have seen that the transient cross sections vanish at the spectral position of the plasmon resonance (compare section 4.3). In order to obtain a large transient signal we therefore use T-Matrix calculations (compare chapter 2.6) to predict the best possible sample geometry. The calculation in figure 4.8 is obtained by calculating the scattering cross section in dependence of the radius for a

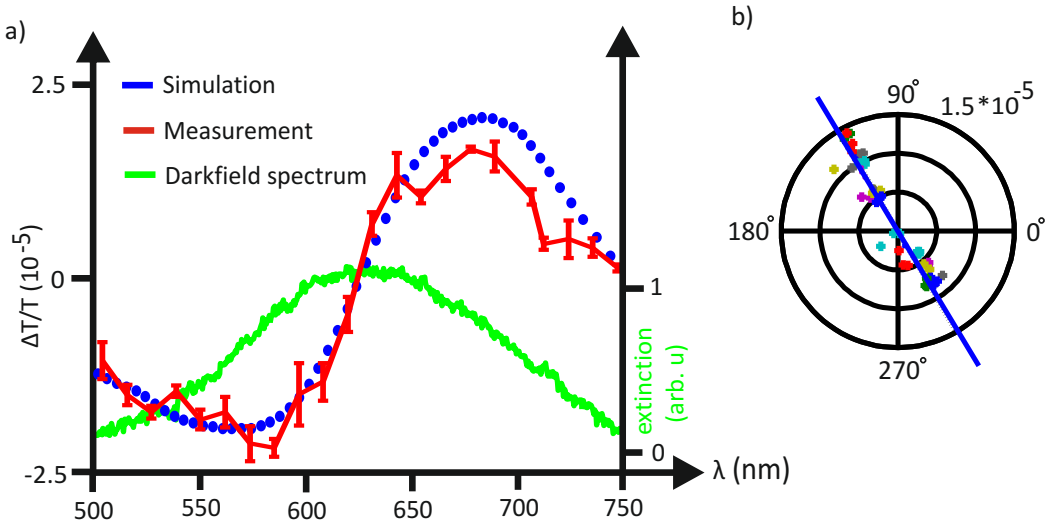

Figure 4.7 *a) Spectrally resolved pump probe measurement of a single gold nano disc with a radius of 50nm and 50nm height. The amplitude spectrum shows a dispersive line shape with a zero crossing at about the plasmon resonance (green). The differential transmission spectrum as calculated by T-Matrix simulation is shown in blue. b) The polar plot of the oscillation amplitude shows a constant phase over all measurements which is to be expected as the mechanical oscillation phase is determined by the geometry of the particle [51].*

particle of 50nm height at a wavelength of 800nm for a ground state ($c_{sca,gs}$) and an excited state ($c_{sca,es}$). Δc_{sca} is then defined as

$$\Delta c_{sca} = c_{sca,es} - c_{sca,gs} \tag{4.10}$$

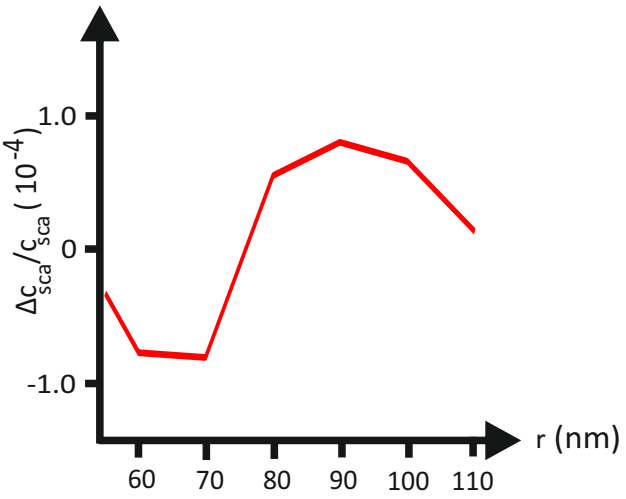

Figure 4.8 *T-Matrix simulation of the differential scattering cross section of a gold disc of 50nm height and radius r calculated for a wavelength of 800nm. The curve shows a dispersive line shape that has a zero crossing at about 80nm disc radius. The extrema of the curve are located at 60-70nm and 90-100nm disc radius. The simulation predicts a maximal relative change of* 10^{-4} *assuming a temperature change in the gold disc of* $\Delta T = 10K$

4.6 Conclusion

Building a time resolved nearfield microscope combines two experimentally challenging techniques. The goal is to demonstrate the combination of picosecond temporal resolution as well is 20nm spatial resolution. The model system used for the proof of principle measurement are the mechanical oscillation of metal nano particles that are excited with a short pump pulse. We model the elastomechanical properties of our gold discs in Comsol and get a good agreement between measurement and simulation. In particular we find that the oscillation period of the first order breathing mode of a metal disc is proportional to the disc radius. We continue to investigate the spectral dependence of the differential scattering signal and find a dispersive line shape that has a zero crossing at the plasmon resonance. The differential scattering measurements are backed up by T-Matrix calculations. In the end we use T-Matrix calculation to optimize the gold disc geometry with respect to the differential scattering cross section. For a disc height of 50nm and a wavelength of 800nm we determine the optimal disc radius to be 90nm to 100nm.

CHAPTER 5

Apertureless Scanning Nearfield Optical Microscopy

In the last chapter pump probe measurements served as a characterization tool for the mechanical properties of gold nano discs, as well as a means to familiarize one self with the pump probe approach. Before the pump probe technique is combined with the nearfield microscope, nearfield measurements are carried out on gold nano discs in order to characterize the nearfield response of the gold nano discs as well as to get to know the behaviour of the nearfield microscope. Scanning nearfield optical microscopy (SNOM) is a technique that allows to optically investigate nano structures beyond the farfield resolution limit which states that the smallest distance between two objects to be separable is given by [42]

$$\Delta d = \frac{\lambda}{2 \cdot NA} \tag{5.1}$$

where λ is the wavelength of light and NA is the numerical aperture. This limit is circumvented in SNOM by placing a scatterer at a distance much smaller than the wavelength of light from the sample surface. At these distances the detector interacts with exponentially decaying nearfields. In this chapter we demonstrate the nearfield capabilities of the setup by measuring the nearfield distribution of a plasmonic particle. These measurements also serve as a characterization step on the way towards the timeresolved nearfield microscope. On the long run, the goal is to create a tool that has a temporal resolution on the order of 10fs as well as a spatial resolution of 10nm. There are two approaches to nearfield microscopy which utilize either aperture probes or apertureless probes. Aperture probes are typically realized by tapering a glass fiber which shrinks the fiber core down to a size of a few hundred nanometers and less, thereby creating a nanoscopic aperture. The aperture fiber can either be used in collection mode or excitation mode in which it serves as

a nanoscopic lightsource that can be used to efficiently funnel light into highly localized modes [62]. The spatial resolution achievable with such an aperture SNOM is given by the aperture size which is typically limited to roughly 100nm. This limit is a result of the transmitted power P_{taper} through the tapered fiber which is [35]

$$P_{taper} \propto e^{-\frac{d}{\lambda}} \tag{5.2}$$

where d is the aperture diameter and λ is the wavelength. In the excitation mode, where the probe light is delivered through the tapered fiber, the temporal resolution of a time resolved near field microscope is limited due to the pulse broadening occurring in the fiber. The temporal broadening is characterized by the GVD value (group velocity dispersion) and can be expressed as [63]

$$GVD = \frac{\lambda^3}{2\pi c^2}\frac{d^2n}{d^2\lambda} \tag{5.3}$$

where n is the refractive index.

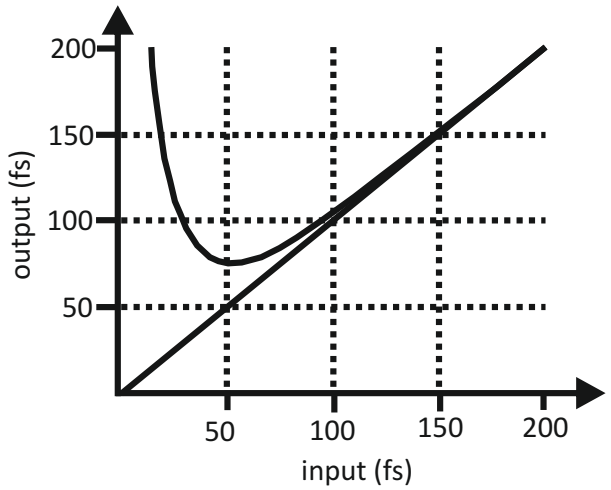

Figure 5.1 *Input pulse width compared to the output pulse width for a travel distance of 20mm through silica glass with $n_{silica} = 1.4$. The center wavelength of the pulse is 800nm. For input pulse durations above 100fs the pulse broadening is negligible whereas a 25fs input pulse has already a width of roughly 100fs after exiting the glass.*

Figure 5.1 shows the effect on the pulse duration of a 800nm center wavelength input pulse when traversing through 20mm of silica glass. The strong dispersion of a broad band pulse severly reduces temporal resolution.
When using the aperture SNOM in collection mode the temporal resolution of a broad band source can be conserved, as has already been demonstrated by Kuypers et al. [64]. Overall the aperture SNOM is capable of delivering very good temporal resolution in combination with a slightly enhanced spatial resolution that is given by the aperture diameter.

In apertureless SNOM (aSNOM) a sharp tip made of metal or dielectric is used as a local probe. Because the illumination and detection is realized in a free space configuration, the temporal resolution of the aSNOM is only determined by the light source used. Furthermore the spatial resolution of the aSNOM is independent of the wavelength of the light and only dependent on the radius of the apex of the tip. A spatial resolution of $d = \frac{\lambda}{100}$ and better has already been demonstrated [65].
In summary the apertureless approach to SNOM is limited by the temporal resolution of the laser source and the spatial resolution is limited by the size of the tip apex which can be 10nm or even smaller. We favor the aSNOM approach as it is the experimental approach with the least theoretical limitations regarding achievable spatial and temporal resolution.

The apertureless SNOM used in this thesis is based on a design developed by R. Vogelgesang and coworkers [20]. The technical details of the apparatus have already been shown in section 3.5.

To characterize the nearfield response of the experiment we use a sample consisting of gold discs on a glass substrate. The disc dimensions are chosen such that the structure delivers a high differential nearfield signal (see 4.5) at a wavelength of 800nm. Detailed information on the sample design is given in section 4.5. The samples were created using a combination of electron beam lithography and metal evaporation process. All samples where manufactured by K. Lindfors.

5.1 FEM field simulations

Prior to the measurements the nearfield signals where simulated using the FEM based software Comsol Multiphysics [55, 66, 67]. The wave front in the focus of the objective is approximated as a plane wave. The total field E_{tot} is the sum of the excitation field E_{back} and the scattered field E_{scat}.

$$E_{tot} = E_{back} + E_{scat} \tag{5.4}$$

In order to mimic the excitation field in the experiment the components of

$$E_{back} = \begin{pmatrix} E_x \\ E_y \\ E_z \end{pmatrix} \tag{5.5}$$

are defined as

$$E_{bx} = 0 \tag{5.6}$$

$$E_{by} = E_y \cdot e^{\frac{j \cdot n_{eff} \cdot 2\pi}{\lambda_0}} \cdot (sin(\phi) \cdot z + cos(\phi) \cdot x) \tag{5.7}$$

$$E_{bz} = 0 \tag{5.8}$$

where E_y is the field amplitude, n_{eff} is the refractive index of the surrounding medium, λ_0 is the wavelength and ϕ is the angle between sample surface and propagation direction. Figure 5.2 shows a top view of the model structure which has been adapted from other works [68] and modified to suit the experiment. A gold disc sits in the center of a medium with refractive index n_{eff} (blue). The outer shell of the model is given by a perfectly matched layer (PML) (outside of dashed white line) with a spherical scattering condition at the outer surface of the PML of $k_{dir}(r) = -n(r)$. To evaluate the fields, an integration plane parallel to the x-y direction is implemented 10nm above the disc surface (not shown in the figure). For the model parameters we use a disc radius of 100nm and a disc height of 50nm. Furthermore we choose $\phi = 18°$, $n_{eff} = 1.4$, $E_x = 0$, $E_y = 1V/m$ and $\lambda_0 = 800nm$. The dielectric properties of gold are taken from the data by Johnson and Christy [26]. The PML mimics an infinitly extended simulation volume by dampening all impinging field components and thereby suppressing any reflections occurring from the boundaries of the shell. We use an adaptive mesh in order to get a good compromise between the number of elements, the computation speed and the simulation accuracy. From the simulation data we then extract the z-component of the scat-

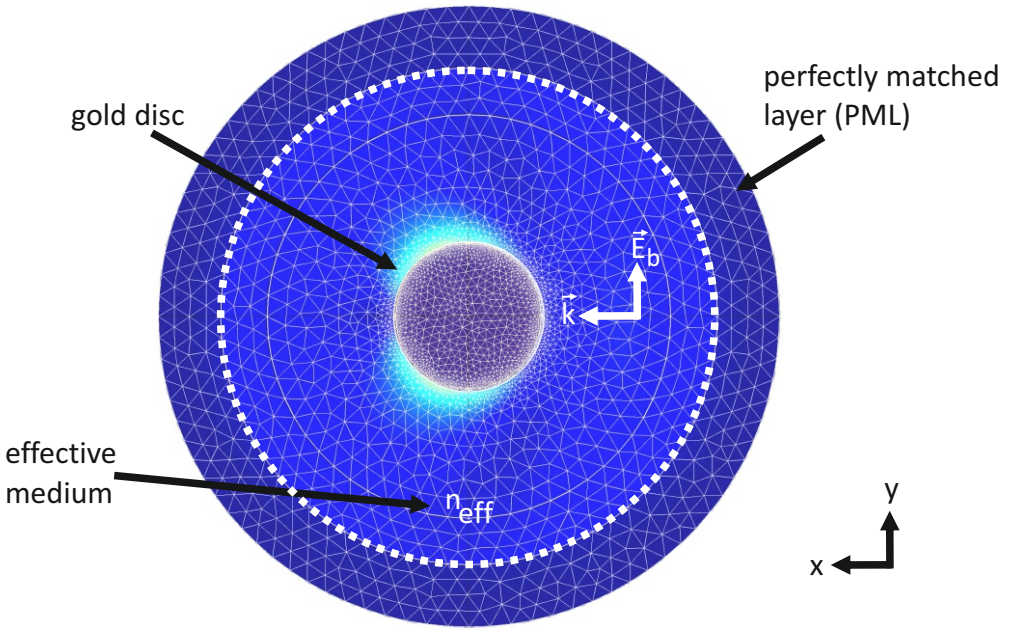

Figure 5.2 *Top view of the Comsol model used for the calculation of the nearfields around a gold disc of 100nm radius and 50nm radius. The gold disc is embedded in an effective medium sphere. Backreflections from the model borders are suppressed by introducing a PML shell around the effective medium. The excitation wavelength of is 800nm.*

tered field E_{sca} in the evaluation plane. Figure 5.3 shows the field distribution of

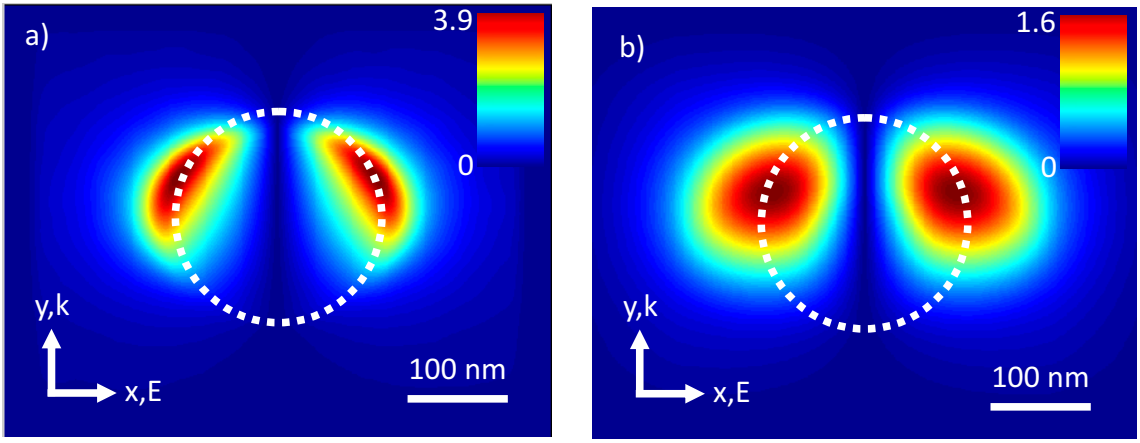

Figure 5.3 *Magnitude of the z-component of the electric nearfield as extracted from a Comsol simulation in a height of 10nm above the gold disc a) and in a height of 40nm above the gold disc b). The simulated disc has a radius of 100nm and a height of 50nm. The circumference of the disc is represented as a white dashed line in the plots. The color scale is given in units of the exciting electric field whose wavelength is 800nm. The z-component of the electric field shows two lobes that are symmetric in the polarization direction of the incident electric field and asymmetric in the x-direction which is a result of the illumination under an angle $\phi = 18°$. The magnitude of the fields is given in values of the excitation field.*

the z-component of the electric nearfield for heights of 10nm a) and 40nm b) above the gold disc surface. The scale of the plot is given in units of the exciting background field E_b. The outline of the disc is shown as a white dashed curve. The field pattern shows two lobes that are symmetric in the x-direction. This field pattern corresponds to the dipolar plasmon resonance. One feature of the plasmon resonance is that it allows to create local hot spot with fields that are significantly higher than the incident fields. Along the propagation direction k of the exciting electric field the field pattern is asymmetric which is a result of the illumination under an angle of $\phi = 18°$ with respect to the sample plane. Comparing the evaluation heights in figure 5.3 a) and b) shows that with increasing evaluation height z, the nearfield decreases in intensity and spreads out laterally well beyond the outline of the disc.

5.2 aSNOM with a CW laser

The timeresolved nearfield measurements that we pursue as an ultimate goal need a pulsed laser source. However in order to collect experience with the measurement technique a CW-laser, namely a Nd:Yag laser at 1064nm, was used in the begin-

ning. The usage of the Nd:Yag laser facilitates the nearfield measurements as the alignement of the Mach-Zehnder interferometer is easier due to the much longer coherence length of the Nd:Yag laser compared to a pulsed laser source. The gold discs on the sample (KL100) were arranged in a penrose tiling and have a radius of 100nm and a height of 50nm. Figure 5.4 shows an example measurement. The experiment allows for the simultaneous aquisition of topography a), magnitude of the z-component of the electric nearfield b) and phase of the electric nearfield c). The mean oscillation amplitude of the cantilver is chosen to be 20nm which corresponds to an average evaluation height of 10nm. The magnitude image in b) shows dipolar field patterns at the positions of the gold discs. Having a look at the phase in c) one sees that there is a phase change of $180°$ between adjacent lobes, resulting from the countermoving nature of the dipole mode. These results agree very well with measurements done by Esteban et al. [69].

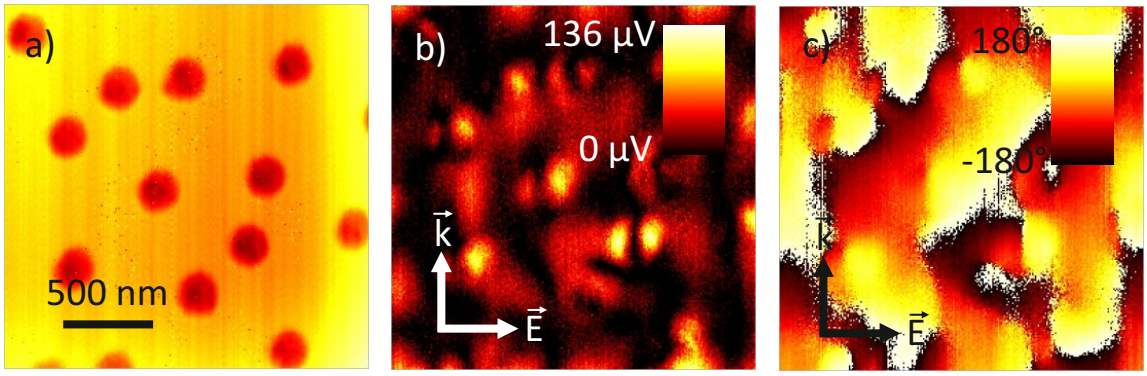

Figure 5.4 *Topography a), nearfield magnitude b) and nearfield phase c) as obtained with the aSNOM. The measurements reveal the dipolar plasmon mode that is expected for an illumination wavelength of 800nm and a disc radius of 100nm.*

Figure 5.5 concentrates on a single gold disc. The data shown is extracted from the measurement as shown in figure 5.4. In addition, the height profile, the signal profile and the phase profile are overlayed on the 2d data. The topography shows a disc height of roughly 50nm. The line profile of the magnitude reveals a maximum signal of $120\mu V$. Furthermore there is some background signal visible which results from an imperfect cross polarization. The phase exhibits a change of $180°$ when going from one lobe to the other. In part d) of the figure, the right part of the lobe is isolated and a curve is fitted to the the nearfield signal between the disc center and the lobe maximum. According to the simulations shown in figure 5.3 a) the nearfield profile along this line is almost steplike. We can use this step in the nearfield signal to estimate the lateral optical resolution that we achieved in the measurement by determining the slope in figure 5.5 d) Therefore for this measure-

ment a tip width of 40nm is obtained which also corresponds very well with the ramp like behaviour of the disc edge in the topography signal.

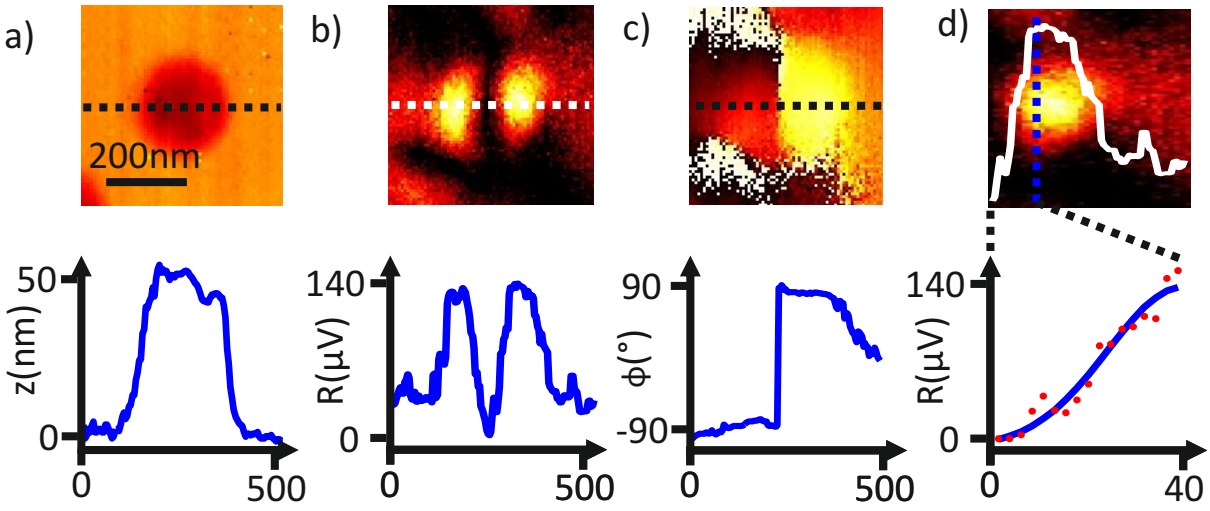

Figure 5.5 *Magnified view of the measurement in figure 5.4. The colormaps are overlayed with line profiles of the signal along the white dashed line. a) shows the topography signal, b) shows the magnitude of the z-component of the nearfield, c) shows the phase of the z-component of the nearfield and d) is a magnified view of the right lobe of b). The magnitude of the nearfield shows a dipolar pattern. The between the lobes changes by* 180^{circ}

After the functionality of the setup with a CW-laser source has been verified, the next step is to modify the experiment such that interferometric measurements with a pulsed laser source, namely a Mira HP 900, are possible. The Ti:Sa laser emits laser pulses with a temporal width of 100fs at a central wavelength of 800nm. The coherence length L of the pulses is [70]

$$L = \frac{2 \cdot ln2}{\pi \cdot n} \frac{\lambda^2}{\Delta\lambda} \tag{5.9}$$

where n is the refractive index of the medium, λ is the center wavelength of the pulse and $\Delta\lambda$ is the pulse width. For a wavelength of 800nm and a pulse width of 5nm we get $L = 56\mu m$. This sets an upper limit on the path difference of both arms in the Mach-Zehnder interferometer. After having established the zero path difference, nearfield measurements are carried out again.

5.3 aSNOM with a pulsed laser

The sample used to demonstrate nearfield measurements with a pulsed laser source is KL120 which contains gold discs arranged in a regular array with a lattice constant of 700nm. The gold disc dimensions are 100nm radius and 50nm height and

the excitation wavelength is 800nm.
Figure 5.6 shows a nearfield measurement of KL120 in which the pulsed Ti:Sa is used. The data set shows the topography a), magnitude of the z-component of the electric nearfield b) and phase of the electric nearfield. The magnitude image in b) shows the dipolar field pattern at the positions of the gold discs. Having a look at the phase of the nearfield in c) one sees that there is a phase change of $180°$ between adjacent dipole lobes, resulting from the countermoving nature of the dipole mode. Compared to the measurements shown in figure 5.4 the signal now shows almost perfect background suppression and a uniform background.

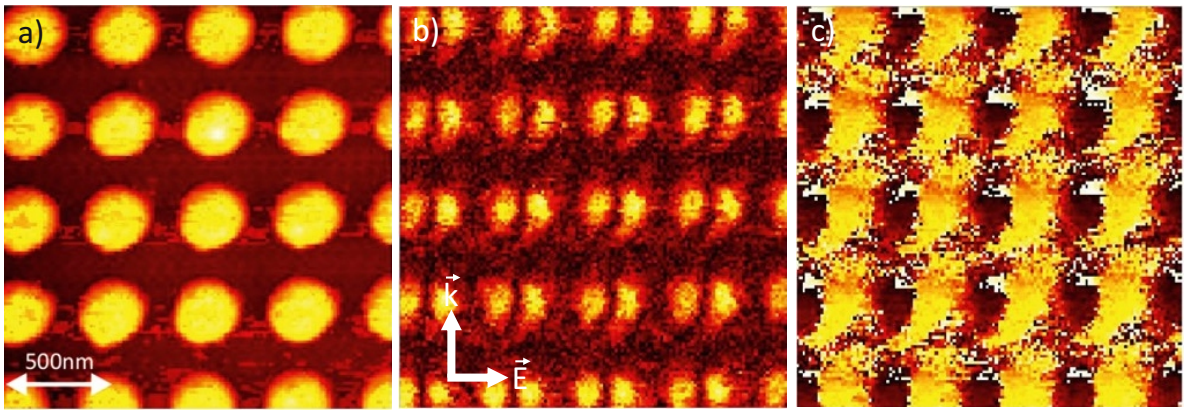

Figure 5.6 *Measurement data for a regular array of gold discs measured with a pulsed laser at source at a wavelenght of 800nm. The nearfield signal in b) shows dipolar pattern and is almost background free. The topography map in a) suggests that the sample consists of gold discs that are 300nm in diameter. Therefore the array looks very dense. However this topography suffers from AFM artefacts caused by a blunt tip. In reality the gold disc have a radius of 100nm and a height of 50nm.*

Figure 5.7 shows a magnified view of one of the gold disc in figure 5.6. In addition, each 2D map has a profile along the dashed line overlayed. The topography shows a disc height of roughly 50nm. The line profile of the magnitude reveals a maximum signal of $100\mu V$. The phase changes by $180°$ when transitioning between the two lobes.

Overall the measurements with the pulsed laser show the same behaviour as the measurements with the CW laser.

5.4 Conclusion

In summary this chapter demonstrates the functionality of our aSNOM setup that allows us to detect nearfields with a spatial resolution of up to 20nm. The measurement scheme allows to acquire simultaneously data for topography, magni-

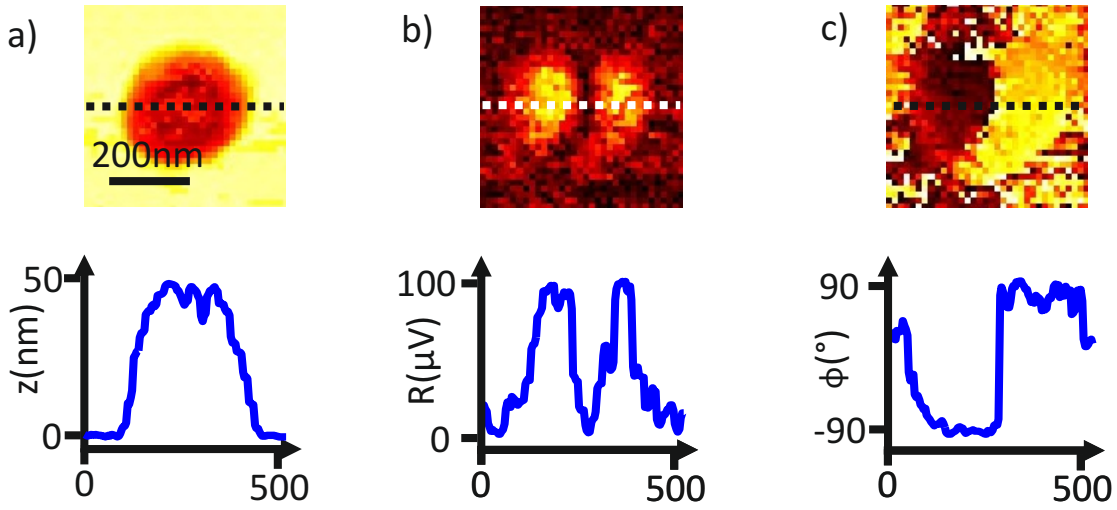

Figure 5.7 *Nearfield data set recorded under pulsed laser excitation at 800nm. The line profile of the magnitude reveals a maximum signal of* $100\mu V$*. In the topography image we see that the gold disc seems to be much bigger than 200nm in diameter. From other AFM measurements on the same sample, we know that the real size of the gold discs is 200nm. The seemingly increased size in the topography is an AFM artefact and stems from a blunt tip.*

tude and phase of the z-component of the electric nearfield. The sample structures measured are single gold discs that upon excitation with 800nm and 1064nm wavelength showed a dipolar plasmon resonance. The plasmon resonance is characterized by a two lobed structure that shows a change of $180°$ in the phase signal. The measurements are confirmed by FEM simulations. In conclusion we find that we are able to obtain nearfield images with a CW laser as well as a pulsed laser.

CHAPTER 6

Pump Probe Apertureless Scanning Nearfield Optical Microscopy

The last two chapters introduced the ingredients that one needs to build a pump probe apertureless scanning nearfield optical microscope (ppaSNOM), a device that combines the high lateral optical resolution of an aSNOM of about 20nm with a temporal resolution of about 1ps given by the pump probe scheme. The experimental setup has already been described in 3.6. To demonstrate the functionality of the experimental setup, a proof of principle measurement is carried out on the mechanical oscillations exhibited by gold discs after excitation with a short pump pulse. We describe the alignement process of the experiment which requires to overlap the noncollinear pump and probe focus. Furthermore we show how the zero path difference between pump and probe focus is obtained. Furthermore we predict the measurement signals with FEM simulations. A detailed analysis of the measurement signals sheds light onto the limitations of the experimental setup. In the end of the chapter improvements to the setup and the experimental technique are discussed in order to increase the sensitivity.

6.1 Overlapping pump and probe beam

One of the bigger challenges of this experimental setup is given by the noncollinear beam paths of pump and probe beam which is visualized in figure 6.1. To achieve the best possible configuration, the nearfield alignment was established in a first step. The AFM tip is brought into the focus of the probe beam and cross polarization is established. After that a nearfield scan is done to verify the functionality of the setup. In a next step the AFM tip is retracted from the surface using the piezos in

the AFM head. By using the AFM piezos for this, the tip can be brought back into the focus position with very high accuracy.

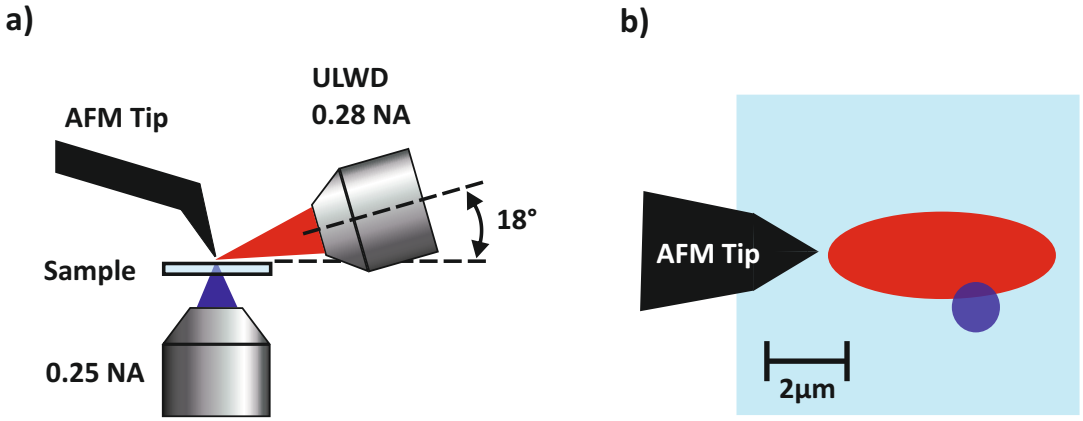

Figure 6.1 *a) Measurement geometry of the ppASNOM. The AFM tip is positioned in the focus of both pump(blue) and probe (red) focus. b) Top view of the tip sample region. The tilted illumination by the probe beam causes an elliptical focus in the sample plane.*

To find the best possible overlap between pump and probe beam, the pump is now placed close to the AFM tip using a motorized mirror mount in the pump path. The AFM camera assists here by providing a top view of sample and AFM tip. The positioning accuracy using this approach is roughly $15\mu m$. The fine alignment is achieved by scanning the sample stage. Note that in our configuration the pump beam position is stationary with respect to the sample stage. This means that by scanning the sample stage one is scanning the pump beam with respect to the probe beam. Figure 6.2 shows a topography image of one of our samples that consists of an area of gold discs with 100nm radius and 50nm height arranged in a lattice with defects. The dashed curves depict the outlines of both the pump and the probe beam.

Scanning the sample stage and simultaneously recording the pump induced change in the reflection signal ΔR a map like in figure 6.3 a) is obtained. The shape of the signal is determined by the convolution of pump and probe focus shape. The pump beam is in normal incidence with respect to the sample plane. However because the probe beam propagates at only $18°$ with respect to the sample plane, the probe focus as well as the shape of the reflection signal are strongly elliptical. The sample stage/the pump focus is then placed at the position of highest signal ΔR. In a last step the delay dependent reflection signal is scanned in order to find the zero path difference. Figure 6.3 b) shows the delay dependent measurement. As already shown in chapter 3, the delay trace shows a flat curve at negative delays and an oscillation signal superimposed on a thermal background after excitation by the pump pulse. In contrast to the measurements in chapter 4, the delay curves mea-

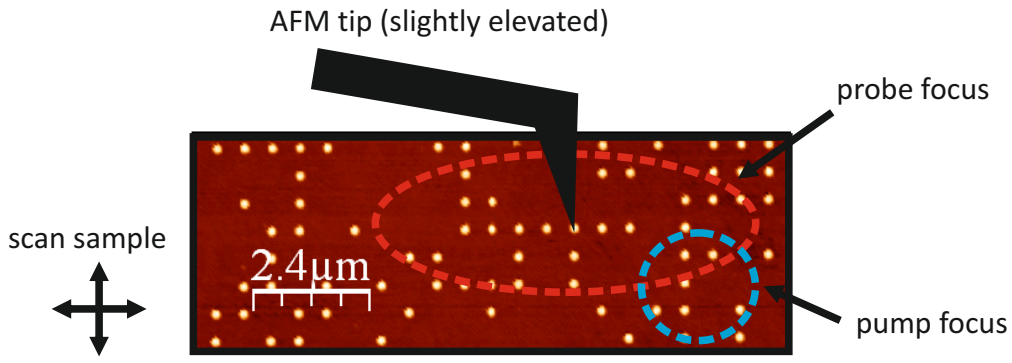

Figure 6.2 *Topography image overlapped with the pump and probe focus which are to scale. The pump focus is stationary on the sample. By moving the sample and recording the differential reflection signal ΔR the overlap between pump and probe focus can be achieved.*

sured in the ppaSNOM setup never showed an electronic spike at the zero path difference (compare 4.5). This behaviour could be caused by the longer duration of the pump pulses used in the ppaSNOM setup which could smear out the electronic peak. The nominal pulse duration of the laser source used in chapter 4 and in the ppaSNOM is the same at about 100fs after the laser but because optical fibers are used in the ppaSNOM, the pulses are smeared out to about 1.5ps through dispersion in the fiber. Nevertheless, although the electronic peak is absent we can very well deduce the position of the zero path difference from the beginning of the plateau in figure 6.3 b). The shape of the signal is determined by the convolution of pump and probe focus shape. The pump beam is in normal incidence with respect to the sample plane. However because the probe beam propagates at only $18°$ with respect to the sample plane, the probe focus as well as the shape of the reflection signal are strongly elliptical. The sample stage/the pump focus is then placed at the position of highest signal ΔR. In a last step the delay dependent reflection signal is scanned in order to find the zero path difference. Figure 6.3 b) shows the delay dependent measurement. As already shown in chapter 3, the delay trace shows a flat curve at negative delays and an oscillation signal superimposed on a thermal background after excitation by the pump pulse. In contrast to the measurements in chapter 4, the delay curves measured in the ppaSNOM setup never showed an electronic spike at the zero path difference (compare 4.5). This behaviour could be caused by the longer duration of the pump pulses used in the ppaSNOM setup which could smear out the electronic peak. The nominal pulse duration of the laser source used in chapter 4 and in the ppaSNOM is the same at about 100fs after the laser but because optical fibers are used in the ppaSNOM, the pulses are smeared out to about 1.5ps through dispersion in the fiber. Nevertheless, although the electronic peak is absent we can very well deduce the position of the zero path differ-

ence from the beginning of the plateau in figure 6.3 b). The AFM tip is still hovering above the sample and can now be easily repositioned in both pump and probe focus. At the end of this adjustment procedure the overlap between pump and probe focus as well as the zero path difference are established. The AFM tip is positioned at the focii and the cross polarization is still intact. This system is now prepared to measure differential nearfield signals.

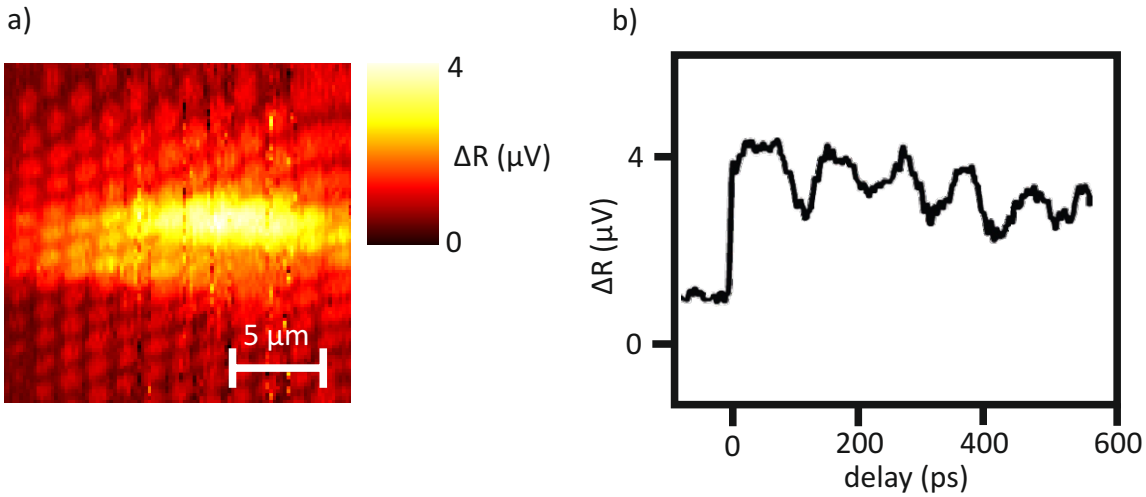

Figure 6.3 *a) Measuring the change in reflection signal ΔR in dependence of the sample position, the best overlap between pump and probe is found. b) After finding the overlap between the two focii, the delay is scanned to find the zero path difference between pump and probe.*

6.2 FEM calculations

The differential nearfield signal maps are calculated using Comsol Multi Physics. The model developed in our group [67] consists of a gold disc embedded in a spherical effective medium of refractive index $n_{eff} = 1.4$ that is surrounded by a perfectly matched layer (PML). A s-polarized background planar wave E_b, which serves as the excitation wave, impinges on the gold disc. The propagation direction of E_b is tilted by 72° with respect to normal incidence in order to reflect the experimental geometry shown in figure 6.1. The disc in the model has a diameter of 200nm and a height of 50nm. The dielectric properties of gold are given by the Johnson and Christy measurements [26]. We then calculate the full field of a gold disc in it's ground state (gs) and the full field of an expanded gold (es) disc with an increased diameter of 202nm. The increase in diameter by 2nm caused by the mechanical oscillation is much too large for a typical temperature increase of 10K. A value of 1pm would be much more suitable, however due to mesh/computer limitations we

choose a larger disc expansion to calculate the qualitative behaviour of the differential cross section. For the expanded gold disc at T=303K we additionally modified the dielectric properties of gold by inserting the modified electron density n_e in the Drude model [71]. To avoid numerical errors through a different meshing between the two different disc sizes the model consists of a gold disc of diameter 200nm that is surrounded by a 1nm thick ring with a height of 50nm. This ring consists of the effective medium in the case of the disc at T=293K and consists of gold in the case of the expanded disc at T=303K. After computing the full field information for both gold discs, we extract the z-component of the electric nearfield in a plane parallel and 10nm above the disc surface which resembles the mean AFM tip - sample distance. We derive the differential nearfield $E_{2\omega_c \pm \omega_{chop}}$ by

$$E_{2\omega_c \pm \omega_{chop}} = E_{2\omega_c, gs} - E_{2\omega_c, es} \quad . \tag{6.1}$$

The simulation results can be seen in figure 6.4. The z-component of the field distribution of the disc in it's ground state (gs) a) and it's expanded state (es) b) show the familiar dipole structure. For normal incidence the dipole field distribution is expected to be symmetric in the sample plane. However because our experiment uses a tilted illumination configuration the symmetry in the propagation direction is broken as retardation effects allready kick in.
Figure 6.4 c) shows z-component $E_{2\omega_c \pm \omega_{chop}}$. Note that the overall shape of the differential field is changed due to the different geometries between the disc ground and expanded state.

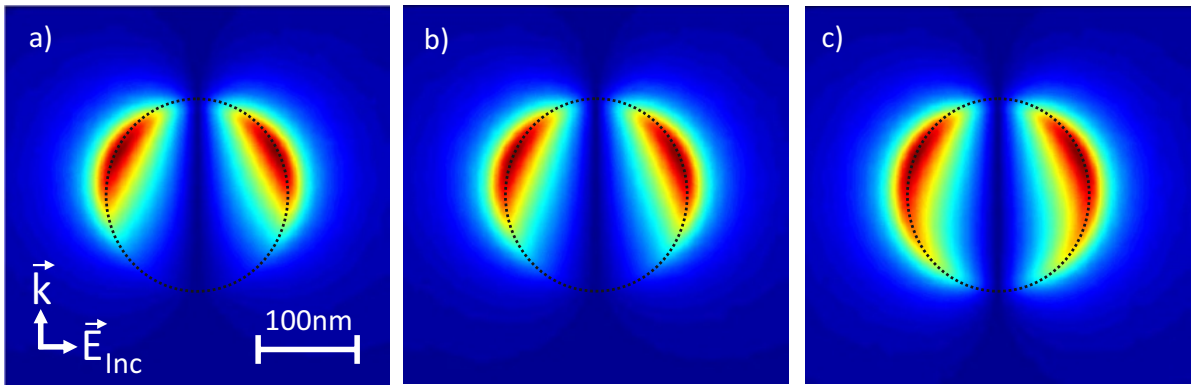

Figure 6.4 *Field distribution of the z-component of the electric nearfield extracted at a position of 10nm above the disc surface. The field map in a) is calculated for a 200nm disc at T=293K whereas the field plot in b) is calculated for a disc of 202nm radius and an altered dielectric function due a decreased electron density. The difference between a) and b) is only visible when substracting the field plots from each other. The differential field plot is shown in c)*

6.3 Signal considerations

The goal of the ppASNOM experiment is to measure a pump induced perturbation of the nearfield signal. Two sources cause a modulation of the signal namely the oscillation of the AFM tip and the periodic modulation of the pump beam by a chopper wheel. The AFM tip scatters the local nearfields into the farfield. As shown in the theory chapter the harmonic oscillation of the AFM tip in the exponentially decaying nearfield creates scattering components that are modulated at the cantilever oscillation frequency ω_c but also at higher harmonics of it. The taylor expansion of equation 2.8 is

$$E_{near,total} \propto A_{near,eff} \cdot (\frac{1}{z} + \frac{d_A}{z} \cdot sin(\omega_c \cdot t + \phi_{cant}) + \tag{6.2}$$

$$\frac{(\frac{d_A}{z} \cdot sin(\omega_c \cdot t + \phi_{cant}))^2}{2} + \tag{6.3}$$

$$\frac{(\frac{d_A}{z} \cdot sin(\omega_c \cdot t + \phi_{cant}))^3}{6} + ...) \tag{6.4}$$

with ω_c being the cantilever oscillation frequency and ϕ_{cant} being the cantilever oscillation phase. In our experiment the nearfield signal serves as a carrier signal for the pump induced modulation. To fully describe the nearfield signal, all frequency components have to be taken into account. However because the lock-in amplifier only demodulates at the second harmonic of the cantilever oscillation we simplify the above formula to

The pump induced perturbation of the nearfield E_{near} can be written as the amplitude modulated field

$$E_{near} = (1 + M_{chop}(t)) \cdot E_{near}(t) \tag{6.5}$$

where M_{chop} is a periodic modulation function with the frequency of the chopper wheel ω_{chop} of the carrier E_{near}. In frequency space this amplitude modulation creates sidebands on all harmonics of ω_c. Assuming a sinusoidal modulation function $M_{chop}(t)$, we can visualize the frequency distribution of the signal according to figure 6.5

This amplitude modulated field is now overlapped with the reference field E_{ref} of the Mach-Zehnder-Interferometer which yields the total electric field E_{tot}

$$E_{tot} = E_{ref} + (1 + M_{chop}(t)) \cdot E_{near}(t) \quad . \tag{6.6}$$

The intensity I_{tot} measured by the detector is therefore

$$I_{tot} = |E_{ref} + (1 + M_{chop}(t)) \cdot E_{near}(t)|^2 \quad . \tag{6.7}$$

E_{ref} which is the field contribution of the reference arm of the interferometer

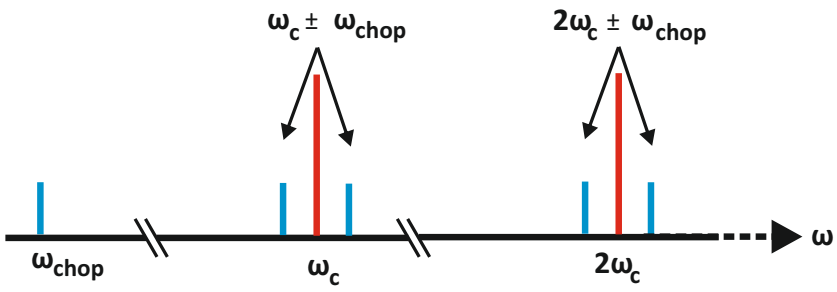

Figure 6.5 *Frequency distribution of the nearfield signal for a sinusoidal modulation function $M_{chop}(t)$. For each carrier frequency $n \cdot \omega_c$ there are two sidebands $n \cdot \omega_c \pm \omega_{chop}$*

shall be given by

$$E_{ref} = A_{ref} e^{i \cdot \phi_{ref}} \tag{6.8}$$

where A_{ref} is the amplitude and ϕ_{ref} is the phase of the reference field, relative to the scattered nearfield. We assume the modulation function M_{chop} to be

$$M_{chop} = A_{chop} \cdot 0.5 \cdot (e^{i \cdot (\omega_{chop} \cdot t + \phi_{chop})} + e^{-i \cdot (\omega_{chop} \cdot t + \phi_{chop})}) \tag{6.9}$$

where A_{chop} is a dimensionless modulation amplitude. The chopper frequency and phase are ω_{chop} and ϕ_{chop}. In our case M_{chop} is a square wave which contains higher harmonics of ω_{chop}. However our assumption of a monochromatic modulation function is still valid because the Lock-In amplifier only demodulates at $2 \cdot \omega_c$ and $2 \cdot \omega_c \pm \omega_{chop}$.

The nearfield scattered of the tip is

$$E_{near} = A_{near} \cdot 0.5 \cdot (e^{i \cdot (2 \cdot \omega_c \cdot t + 2 \cdot \phi_{cant})} + e^{-i \cdot (2 \cdot \omega_c \cdot t + 2 \cdot \phi_{cant})}) \tag{6.10}$$

with A_{near} being the amplitude of the scattered field modulated at the second harmonic, ω_c is the oscillation frequency of the cantilever and ϕ_{cant} is the phase of the cantilver oscillation.

The fields E_{ref},E_{near} and M_{chop} in equation 6.7 are substituted with equation 6.8-6.10 and the resulting expression for 6.7 is evaluated with the software Mathematica. The script and the full solution are given in the appendix A.2. In this equation we isolate the terms that contribute to our measurement signals. In particular we neglect terms that aren't modulated on either the carrier frequency $2 \cdot \omega_c$ or the sideband frequencies $2 \cdot \omega_c \pm \omega_{chop}$. Furthermore we assume that

$$A_{near} \ll A_{ref} \tag{6.11}$$

and

$$A_{chop} \ll 1 \quad . \tag{6.12}$$

Given the above assumptions the following terms for the intensity are left over:

$$I_{2\omega_c}(\phi_{ref}) = A_{near} \cdot A_{ref} \cdot (cos(2 \cdot \omega_c \cdot t + 2 \cdot \phi_{cant} - \phi_{ref}) \tag{6.13}$$
$$+ cos(2 \cdot \omega_c \cdot t + 2 \cdot \phi_{cant} + \phi_{ref})) \tag{6.14}$$

$$I_{2\omega_c - \omega_{chop}}(\phi_{ref}) = A_{2\omega_c \pm \omega_{chop}} \cdot (cos(2 \cdot \omega_c \cdot t - \omega_{chop} \cdot t + 2 \cdot \phi_{cant} - \phi_{chop} - \phi_{ref}) + cos(2 \cdot \omega_c \cdot t - \omega_{chop} \cdot t + 2 \cdot \phi_{cant} - \phi_{chop} + \phi_{ref}))$$

$$I_{2\omega_c + \omega_{chop}}(\phi_{ref}) = A_{2\omega_c \pm \omega_{chop}} \cdot (cos(2 \cdot \omega_c \cdot t + \omega_{chop} \cdot t + 2 \cdot \phi_{cant} + \phi_{chop} - \phi_{ref}) + cos(2 \cdot \omega_c \cdot t + \omega_{chop} \cdot t + 2 \cdot \phi_{cant} + \phi_{chop} + \phi_{ref}))$$

with $A_{2\omega_c \pm \omega_{chop}} = \frac{A_{near} \cdot A_{ref} \cdot A_{chop}}{2}$.
The phase of the reference field E_{ref} is set through the length of the reference arm of the interferometer. In our interferometric measurement $\phi_{ref,1/2}$ is usually chosen such that $\phi_{ref,1} - \phi_{ref,2} = \pi/2$.

The complex signal vectors therefore are

$$\bar{I} = I_{2\omega_c}(\phi_{ref,1}) + i \cdot I_{2\omega_c}(\phi_{ref,2}) \tag{6.15}$$

$$\bar{I}_m = I_{2\omega_c - \omega_{chop}}(\phi_{ref,1}) + i \cdot I_{2\omega_c - \omega_{chop}}(\phi_{ref,2}) \tag{6.16}$$

$$\bar{I}_p = I_{2\omega_c + \omega_{chop}}(\phi_{ref,1}) + i \cdot I_{2\omega_c + \omega_{chop}}(\phi_{ref,2}) \quad . \tag{6.17}$$

Now that we have $\bar{I}_m$ and $\bar{I}_p$ we can construct the side band amplitudes according to [72]. For a pure amplitude modulation we obtain: $\Delta I_{AM} = \bar{I}_m + \bar{I}_p^*$ and for a pure frequency modulation we obtain: $\Delta I_{FM} = \bar{I}_m - \bar{I}_p^*$

For a pure amplitude modulation $\Delta I_{FM} = 0$ and for a pure frequency modulation $\Delta I_{AM} = 0$ [72]. In any case we see that

$$\Delta I_{AM,FM} \propto A_{near} \cdot A_{ref} \cdot A_{chop} \quad . \tag{6.18}$$

6.4 Measurement results

After the setup is prepared as described in section 6.1 the delay is set to +50ps and an overview scan is obtained by recording the nearfield signal and the differential nearfield signal at the frequencies $2 \cdot \omega_c$, $2 \cdot \omega_c \pm \omega_{chop}$. An overview scan of the differential nearfield signal can be seen in figure 6.6.

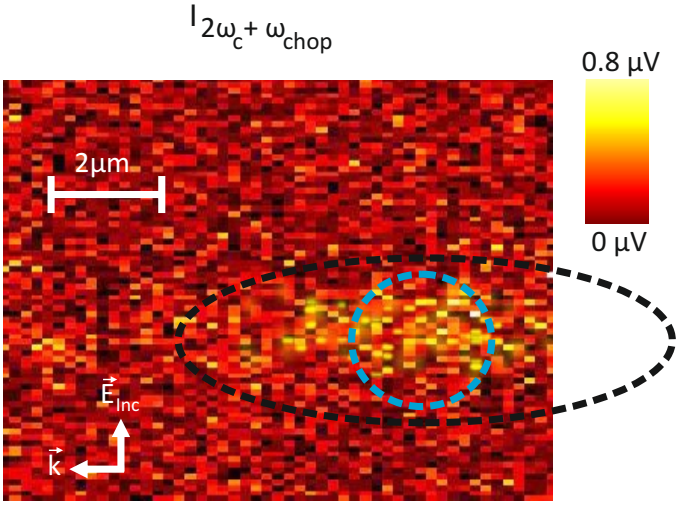

Figure 6.6 *Overview scan to find a gold disc with a good differential nearfield response. The differential nearfield signal only exists in the overlap region between pump and probe.*

We choose the disc with the highest differential nearfield signal. In the ideal case we would now move the sample stage to a position of highest differential nearfield and then scan the delay between pump and probe to directly measure the mechanical oscillation as seen in the farfield experiment. Unfortunately this was not possible in our experiment, because moving the delay stage causes vibrations on the optical table that will result in an AFM tip crashing into the sample while the tip is approached. Instead of the direct measurement of the oscillation we choose to set the delay between pump and probe (while the tip is retracted) and then perform a 2D scan of the topography A, nearfield $\bar{I}$ and the differential nearfield signal $\bar{I}_{p,m}(\phi_{ref,12})$. Note that we measure a 2D scan for each delay twice for two reference phases $\phi_{ref,12}$ with $\phi_{ref1} - \phi_{ref2} = \pi/2$ in order to contruct the complex nearfield $\bar{I}$. Because each 2D scan takes 15 minutes, we select a scan area of $400nm \times 400nm$ to allow thermal drifts without the disc moving out of the scan window. The exact data evaluation script is given in the appendix A.1. In addition we perform a control scan that shows that the differential nearfield signal vanishes when the pump light is switched off. Figure 6.7 shows a measurement series of a single gold disc. Note that the data was measured for a random order for the delays τ. From the top left to bottom left and then from top right to bottom right the 2D scans are ordered

by delay τ in ascending order. In each half the topography A, the complex valued nearfield $\bar{I}$, the amplitude of the differential nearfield ΔI_{AM} and its phase $\phi_{\Delta_{I_{AM}}}$ are shown. Note that for the side band amplitude two values namely ΔI_{AM} and ΔI_{FM} can be constructed. We did the construction for both signals. For the constructed signals we found $\Delta I_{AM} \gg \Delta I_{FM}$ which is why we conclude that we have to deal with an amplitude modulated nearfield signal $\bar{I}$. In addition the data is shown for the case that the pump light is switched off by a beam block (botton right). The topography image serves two purposes. First it allows to control the state of the AFM tip which can degrade due to an imperfect height feedback system of the AFM. The degradation in the AFM image would show up either in a change of the particle size or a change in the particle shape. The second purpose of the topography is that it allows to monitor the disc position which could change due to thermal drifts. The second column shows the complex nearfield signal $\bar{I}$. Note that the phase is already encoded in the color scale of this plot. The complex nearfield signal shows the familiar dipole pattern that is offset by a background. Furthermore one can see that the two lobes of the dipole are counter oscillating. The red dashed box denotes the first delay position that was measured, the blue box the second delay position, the yellow box the third delay position and the black dashed box the last delay position. In these four measurements a change in the nearfield signal $\bar{I}$ is occuring, namely the background signal is changing. This tells us that the tip is drifting out of the focus and therefore out of the cross polarization region. In the third and fourth column the magnitude of the differential nearfield signal ΔI_{AM} and its phase $\phi_{\Delta I_{AM}}$ are shown and are discussed in section 6.4.2.

6.4.1 Temporal evolution of the signal

A control measurement has shown that the differential nearfield signal vanishes if the pump light is blocked from the setup. The differential nearfield signal should also vanish if we measure at negative delays, meaning that we probe the plasmon before a mechanical oscillation is started by the pump pulse. However, the data in figure 6.7 shows that there is a signal even at negative delays. One explanation for this behaviour is that the system can't fully dissipate the energy deposited by a pulse. If we have a look at the delay trace in figure 6.3 b) again, we see that at negative delays the signal is not vanishing which indicates that a slow thermal component is always present in the signal. In contrast the thermal decay of the farfield measurements in figure 4.5 is different, although the measurement settings are seemingly the same. An explanation could be that for the farfield setup (described in chapter 3) the discs on the sample were arranged in a lattice with $5\mu m$ period whereas in the nearfield setup (described in this chapter) the discs on the sample where arranged in a much denser array with 700nm spacing. In addition, although the pump beam intensities were the same for both experiments, the objectives to fo-

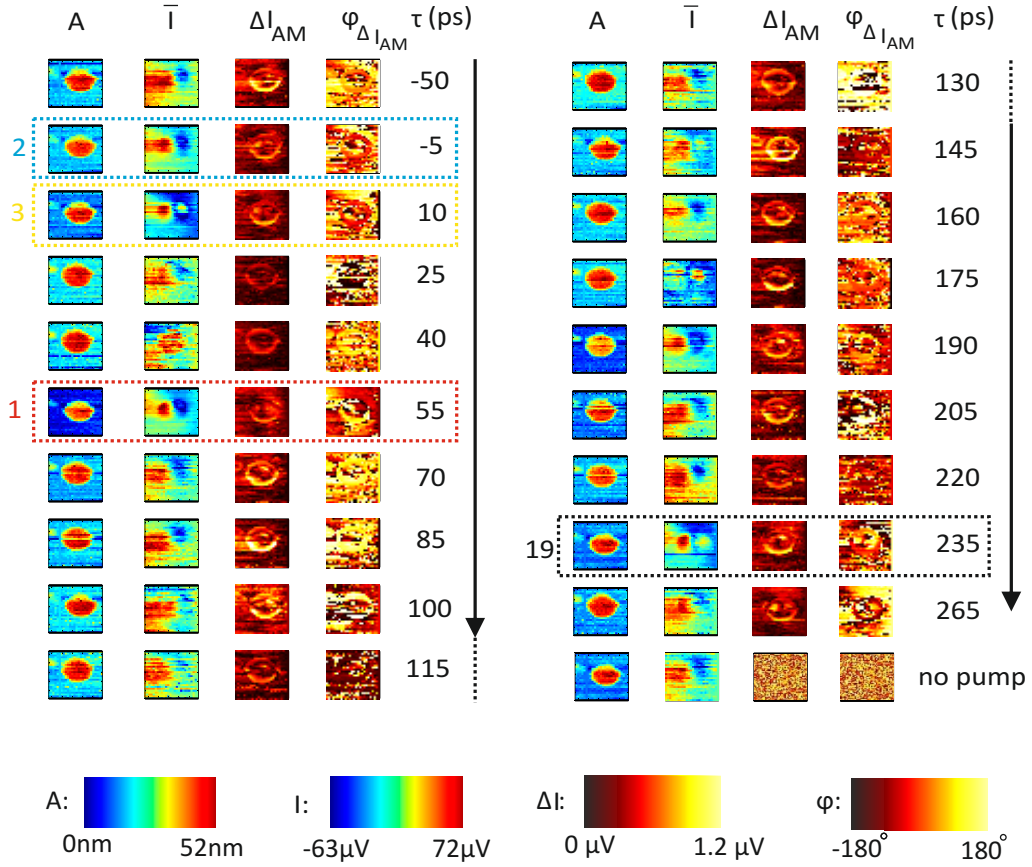

Figure 6.7 *Delay series of a differential nearfield measurement of a gold disc with 100nm radius and 50nm height. The exciation was off resonant at 800nm to ensure the maximal differential nearfield signal. The measurement channels are sorted into colums. For each delay (row) the topography A, the nearfield amplitude $\bar{I}$, the magnitude of the differential nearfield signal ΔI_{AM} and the phase of the differential nearfield signal $\phi_{\Delta I_{AM}}$ are given. The delay τ increases from top left to bottom left and then from top right to bottom right. The scan size is $400nm \times 400nm$. The topography signal shows a disc centered within the frame. The complex nearfield image contains a dipole shape that is typical for the dipolar plasmon resonance. The maps for ΔI_{AM} contain a ring shaped structure that is also visible in the 2D map of the phase. The colored boxes and numbers give the order in which the first few delays where measured. At the bottom right a scan was made with the pump beam blocked in which case we obtain no sideband signal. The sideband signal is independent of the delay τ and even appears at negative delays.*

cus the pump beam were not the same. In both experiments the wavelength of the pump light is $\lambda_{pump} = 400nm$. In the farfield experiment we use a 0.9NA objective resulting at a focus diameter of $d_{ff} = 1.22 \cdot \frac{\lambda_{pump}}{NA} \approx 500nm$ whereas in the pump probe nearfield experiment we use a $NA_{eff} = 0.25$ molded aspheric lens to focus the pump beam which results in a focus diameter $d_{nf} = 1.22 \cdot \frac{\lambda_{pump}}{NA} \approx 2000nm$. As the pump intensities are the same in both experiments the power deposited per area is different because the disc density for the nearfield sample was much higher. To estimate the temperature evolution of the substrate we model the gold disc (100nm radius, 50nm height) as a heat source sitting on a glass substrate. The heating power $P_{heat,V}$ is determined by the absorption cross section $C_{abs} \approx 10^4 nm^2$ and the pump focus intensity $I_{Pump} = \frac{P_{pump}}{A_{focus}}$. With $A_{focus} = \pi \cdot 10^6 nm^2$ and $P_{pump} = 10^{-3} W$ the heating power per volume equates to $P_{heat,V} = 2 \cdot 10^{16} W/m^3$. The substrate has a dimension of 700nm by 700nm and a thickness of 1000nm. As boundary condition we couple the sidewalls and the bottom of the substrate to a temperature reservoir with T=293K. In case of the disc array we assume an infinetly expanded array by only coupling the bottom of the substrate to the temperature reservoir. The meshed model for the single disc and disc in the array case is shown in figure 6.8 a) and b). We now calculate the evolution of the substrate temperature.

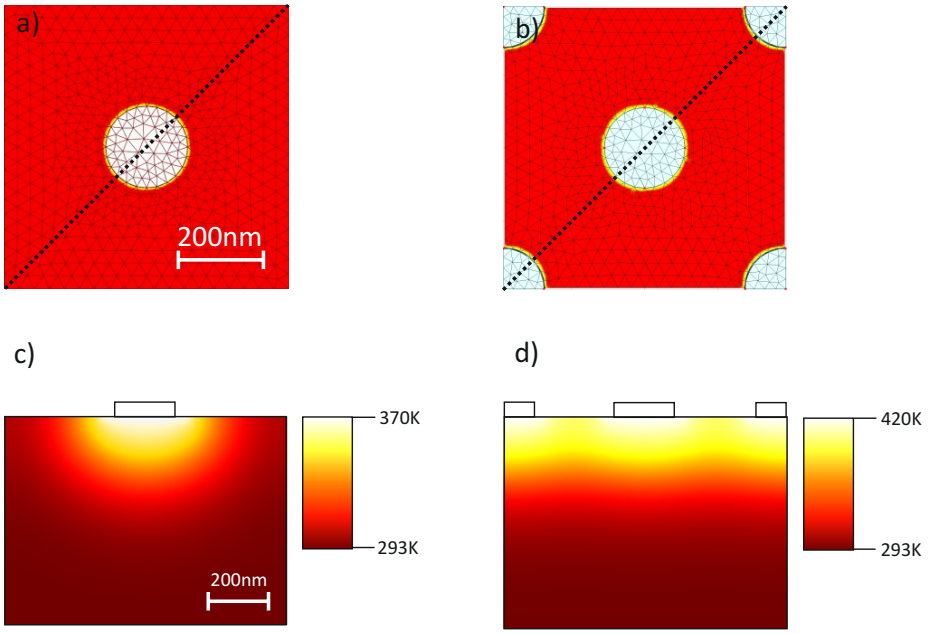

Figure 6.8 *a) and b) show a top view of the model used the simulate the equilibrium temperature of a $700nm \times 700nm \times 1000nm$ glass block that is heated by one gold disc a) and by a gold disc array b). The gold discs act as a heat source with a power density $Q = 2 \cdot 10^{16} W/m^3$. c) and d) show a profile view of the equilibrium temperature along the dashed line in a) and b).*

According to the calculations the equilibrium temperature is reached after about $6\mu s$. Figure 6.8 c) and d) show the temperature profile in equilibrium state. For the temperature profile of the substrate in case of the single disc we can see that $T_{single}(\vec{r} \propto \frac{1}{\vec{r}^2})$ and in case of the array $T_{array}(\vec{r} \propto \frac{1}{\vec{r}})$. Furthermore we see that both, the disc and the substrate have a higher equilibrium temperature in case of the array. This simulation shows why the thermal effects seen in the pump probe measurements of the array are stronger than in the single disc case. The higher substrate temperature also have an effect on the amplitude of the mechanical oscillation because the specific heat capacity $c(T)$ of the gold disc increases with temperature. That also means that the temperature change ΔT that a single pulse causes is getting smaller the higher the base temperature of the disc is. We write

$$\begin{aligned}\Delta T &= \frac{Q}{m \cdot c(T)} \\ &= \frac{Q}{m \cdot (c_0 + \alpha \cdot T)}\end{aligned}$$

with $Q = const$ as the constant energy being depositted by each pulse, m being the mass of the gold disc. Furthermore we assume a linear temperature dependence of the specific heat of gold in the temperature range range between 270K and 470K $c(T) = 128 + \alpha \cdot (T - 293K)$ with $\alpha = 0.34 \frac{J}{kg \cdot K^2}$ (extracted from [73]) and $c_0 = 128 \frac{J}{kg \cdot K^2}$. The evolution of the specific heat in dependence of the temperature is shown in figure 6.9 a). The resulting temperature change for a deposited pulse energy of 100fJ is shown in b). Assuming that the mechanical oscillation amplitude is $A_{mecha} \propto T$ we see that an increase of the substrate temperature leads to a smaller mechanical oscillation amplitude A_{mecha} and therefore a smaller oscillation signal.

6.4.2 Shape of the signal

So far we only discussed the temporal evolution of the differential nearfield signal which seems to be independent of the delay.

Figure 6.10 shows the topography a), nearfield amplitude b) and the magnitude of the differential nearfield signal c) at a delay of τ=55 ps. We choose the data set at 55ps delay as this is the first measurement in the series and the nearfield signal looks best here. The topography shows a roughly 200nm diameter gold disc with 52nm height and small structure to the left with about 20nm height which is supposedly a residue of the fabrication process. The complex amplitude of the nearfield shows the familiar dipole structure with two counter oscillating lobes. There is a drifting background in the signal that is not perfectly suppressed hinting towards an imperfect cross polarization state. The maximal signal amplitude is $73\mu V$. Overall the nearfield image agrees quite well with the Comsol simulations shown in figure 6.4. The differential nearfield signal in c) contains a ring shaped structure

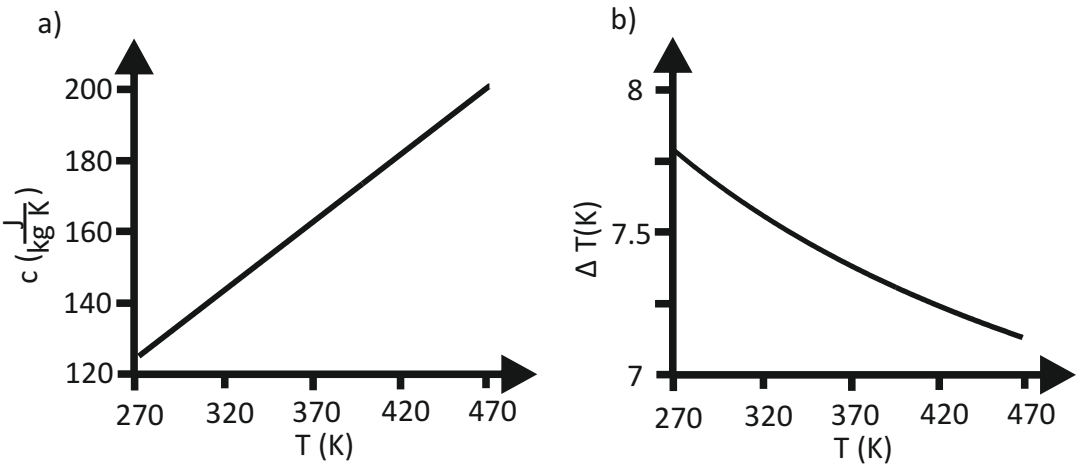

Figure 6.9 *a) The specific heat of gold is a function of temperature. From [73] we derive the relationship $c(T) = 128 + \alpha \cdot (T - 293K)$ for a temperature range between 270K to 470K. b) Calculation for the change in temperature of a gold disc with 100nm radius and 50nm height for different base temperatures between 270K and 470K when absorbing a heat amount of $10^{-13} J$*

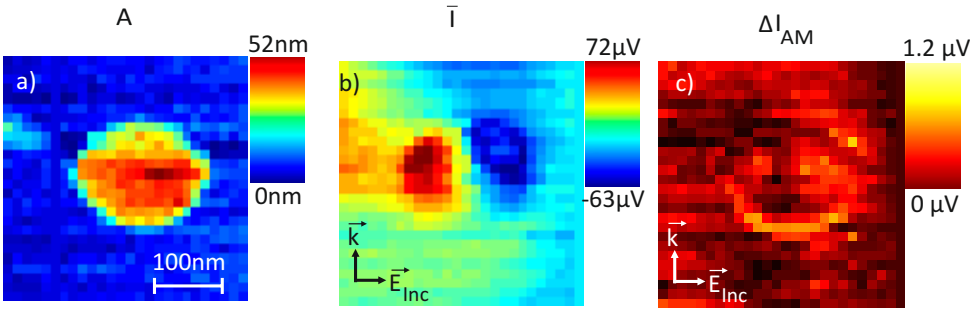

Figure 6.10 *Topography a), complex nearfield amplitude $\bar{I}$ b) and magnitude of the differential nearfield ΔI_{AM} signal c) for the delay $\tau = 55ps$.*

that looks like the outline of the topography. The maximum signal is $1.2\mu V$. In contrast to the nearfield image, the differential nearfield image doesn't resemble the Comsol simulations in figure 6.4. The differential nearfield signal in c) much more looks like the error signal of an AFM height feedback. This together with the fact that we see no delay dependence of the signal brings us to the conclusion that the measured differential signal is a combination of a thermal phenomen and AFM artefacts that overshadow the differential nearfield signal that we were originally looking for. Similar measurement results were obtained in four other measurement series. Unfortunately the experiment had to be disassembled due to a relocation and splitting of the group so that we can't continue to investigate the differential nearfield signals.

6.5 Signal and noise considerations

Although a signal stemming from the differential nearfield is absent in our measurements, we can use the obtained data to determine an upper limit for the differential nearfield signal as well as the modulation depth. The fundamental noise limit in our experiment is shot noise. Shot noise originates from the quantized nature of the photons and can be calculated as [74]

$$\sigma_{SN} = \sqrt{2 \cdot \Delta\nu_{BW} \cdot P_{Det} \cdot \frac{h \cdot c}{\lambda}} \tag{6.19}$$

with λ, c and h being the measured wavelength, the speed of light and the Planck constant. $\Delta\nu_{BW} = \frac{5}{64 \cdot \tau_{int}}$ is the noise equivalent bandwidth for a given filter slope of 24 dB/Oct and depends on the integration time τ_{int} used at the Lock-In Amplifier [75]. A typical integration time of $\tau_{int} = 100ms$ was used in our experiment. The photon flux on the detector $P_{Det} = P_{tip} + P_{ref}$ has two contributions in our setup namely the photon flux P_{tip} originating from the scattered fields of the tip and the photonflux P_{ref} stemming from the reference arm. For the shot noise calculation we neglect P_{tip} because $P_{tip} \ll P_{ref}$. Furthermore $P_{ref} = 0.5\mu W$ with $\lambda = 800nm$ in our experiment. Given these parameters, the shot noise limit equates to

$$\sigma_{SN} = 1.45 \cdot 10^{-14} W \tag{6.20}$$

and therefore the relative noise is

$$\sigma_{SN,rel} = \frac{\sigma_{SN}}{P_{ref}} = 3 \cdot 10^{-7} \tag{6.21}$$

Next we compare this value to the relative noise in the measurement. To evaluate the noise in the measurement we first determine the standard deviation in the background signal of the differential nearfield signal in figure 6.10 which is

$\sigma_{exp,V} \approx 180nV$. Because we can't measure the DC signal of the light on the lock-In amplifier (no DC output), we derive this value from the reference beam power we measured to be $P_{ref} = 0.5\mu W$ multiplied by the gain factor $g = 2 \cdot 10^4 \frac{V}{W}$ of the detector used (Femto HCA-S). The relative noise value of the experiment therefore is

$$\sigma_{exp,rel} = \frac{\sigma_{exp,V}}{g \cdot P_{ref}} \approx 3 \cdot 10^{-6} \tag{6.22}$$

which is about one order of magnitude above the shot noise limit.

From equation 6.15 and 6.18 we can see that the coefficients for the nearfield signal $\bar{I}$ and ΔI_{AM} are $A_{ref} \cdot A_{near}$ and $A_{ref} \cdot A_{near} \cdot A_{chop}$ where $A_{ref} \cdot A_{near}$ is the measured nearfield amplitude and A_{chop} is the modulation index of the amplitude modulation. If we assume that $\sigma_{SN,rel} = 3 \cdot 10^{-7}$ is the upper limit for a detectable signal we can deduce that with a maximum nearfield signal of $I_{Max} = 73\mu V$(from figure 6.10) the modulation index A_{Chop} has to be smaller than

$$A_{chop} \ll \frac{\sigma_{exp,V}}{I_{Max}} = 3 \cdot 10^{-3} \tag{6.23}$$

If we compare this value to the predicted change (see section 4.5) in scattering cross section $\Delta S/S \approx 10^{-4}$ we see that we need to gain at least one order of magnitude in sensitivity.

6.6 Improving the measurement technique

In the last section we estimated an upper limit for the differential nearfield signal ΔI_{AM} and the modulation index A_{chop}. According to equation 6.18 we can write

$$\Delta I_{AM} \propto A_{near} \cdot A_{ref} \cdot A_{chop} \quad .$$

In order to maximise ΔI_{AM}, the coefficients A_{near}, A_{ref} and A_{chop} should be maximised. The reference field A_{ref} can be increased in order to lift the signal above the noise floor, however the signal to noise ratio can't be improved because

$$SNR = \frac{A_{ref} \cdot A_{near} \cdot A_{chop}}{\sqrt{I_{tot}}} = A_{near} \cdot A_{chop} \tag{6.24}$$

as $A_{ref} \gg A_{near}$.
In the following paragraphs we suggest changes to the experimental approach in order to increase ΔI_{AM}:

a) Maximising the modulation ratio A_{chop} can be achieved by increasing the pump power which increases the amplitude of the mechanical oscillation of the nano disc and therefore also increases the detuning of the plasmon resonance.

b) In order to maximise the differential nearfield change, the size of the gold disc was chosen such that the probe wavelength excites the plasmon at the steepest point in the resonance. An alternative approach is shown in figure 6.11. Instead of probing off resonant and detecting a change in scattering amplitude one could also probe on the resonance and detect the phase change of the resonance instead which increases the carrier signal A_{near}.

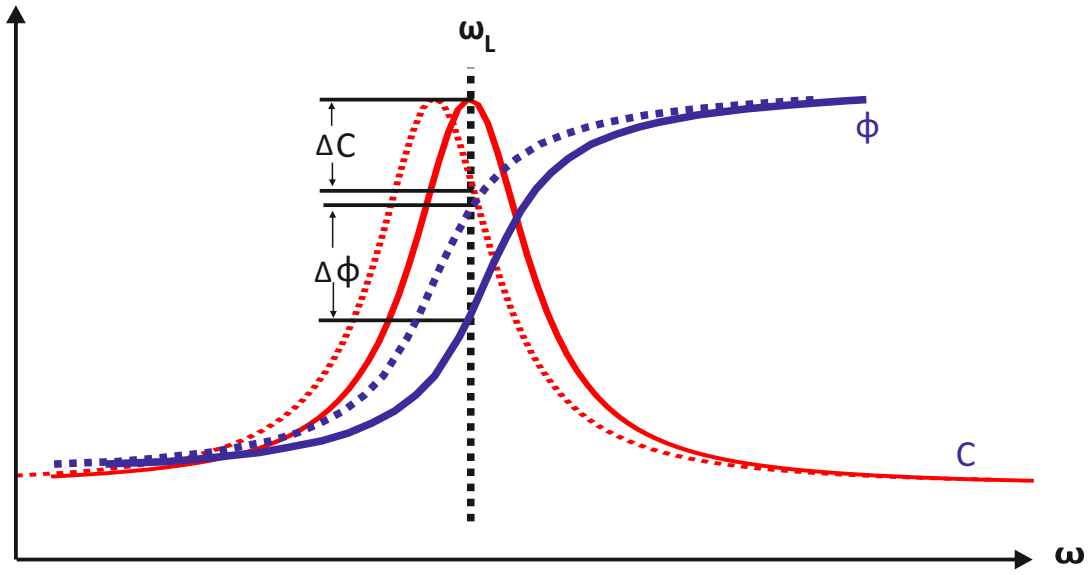

Figure 6.11 *At the plasmon resonance the slope of the phase is highest. Phase sensitive detection would make use of an increased carrier signal* A_{near}

c) Another way of increasing A_{near} is to increase the collection efficiency of the objective. To calculate the collected light of the AFM tip apex in dependence of the numerical aperture (NA) of the objective, we assume the AFM tip to be a dipole that is oriented perpendicular to the substrate (compare figure 6.12a)). We calculate the total integrated electric field E_{tot} of the dipole after an objective in dependence of the NA using a method according to [76]. Note that the angle α between the optical axis and the sample plane is chosen such that $\alpha = arcsin(NA)$ which means that the lower edge of the lightcone touches the sample plane for every NA. Figure 6.12 b) shows the total collected field E_{tot} after the objective in dependence of the NA. According to the calculation the highest light collection efficiency is obtained at NA≈ 0.85. However one might still choose a slightly smaller NA objective due to spatial restrictions at the close vincinity of the AFM tip.

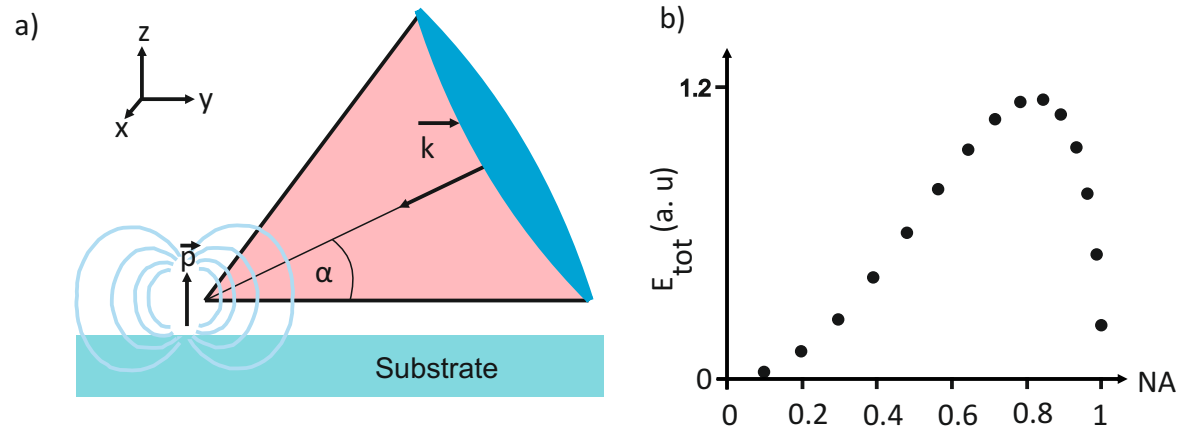

Figure 6.12 *a) The AFM tip can be modelled as a dipole oriented in the z-direction. An objective with NA= $sin\alpha$ collects the emitted radiation. b) Calculation of the total collected field of a z-oriented dipole in dependence of the objective NA. Note that $\vec{k}$ has an angle of α with respect to the sample plane and NA= $sin(\alpha)$. The calculation shown neglect the sample.*

d) In our experiments we use AFM tips made of silicon which are known to have no effect on the plasmonic modes of the sample on the one hand [40], but they are also known to only weekly scatter the nearfields. It has been shown by colleagues that the nearfield response of a weakly interacting tip is [77]

$$A_{near} \propto \vec{p} \cdot \vec{S} \tag{6.25}$$

where $\vec{p}$ is the dipole moment of the AFM tip and $\vec{S}$ is a sum of local fields. In general the dipole moment $\vec{p}$ is defined as

$$\vec{p} = \sum q_i \cdot \vec{x_i} \tag{6.26}$$

with q_i being a charge located at $\vec{x_i}$.

This means that by increasing the charge density, the dipolmoment will also increase. Therefore another possibility of increasing A_{near} is to change the tip material from silicon to a metal like gold. The drawback is that the approximation of a weekly interacting scatterer doesn't hold true any more and in general coupled systems now have to be handled.

In the differential nearfield measurements shown earlier, an AFM artefact spoiled the measurement data. The artefact showed up as a ring that occurs at topography steps. We assume that this artefact is caused by the feedback mechanism that introduces crosstalk between different frequency components in our setup. In order to circumvent the feedback mechanism we propose to perform constant height mode

scans which completely bypass the feedback mechanism at the cost of losing the topography signal.

6.7 Conclusion

In this chapter we presented timeresolved nearfield measurements on single gold nano discs. We introduce the alignment procedure that allows us to position an AFM tip in the focus of two noncollinear beams with very high accuracy. Furthermore the alignment process determines the zero path position between pump and probe pulse. We use the topography as a control measurement for quality of the AFM tip shape and see no degradation over the period of the measurement series. However the nearfield signal degrades over time which can most likely be attributed to thermal drifts within the setup. However the shape of the nearfield signal agrees well with our simulations. The differential nearfield signal most likely originates from AFM artefacts that are pump induced. The sideband signal is independent of the delay which could be due to slow thermal contributions to the signal which we attribute to the sample structure. From our measurements we can estimate that the modulation depth A_{chop} has to be smaller than $3 \cdot 10^{-3}$ which agrees well with a theoretical value of 10^{-4} according to T-Matrix calculations (compare section 4.5). We end the chapter by giving suggestions of how to improve the experimental setup in order to increase the measurement sensitivity.

CHAPTER 7

Conclusion and Outlook

In this work the experimental realization of a pump probe apertureless scanning nearfield optical microscope has been evaluated. This novel device combines the advantages of an ultrafast pump probe spectroscopy scheme and a scattering type nearfield microscope. The resulting tool would allow to investigate nano structures on ultrafast time scales with a a temporal resolution of 1ps and a spatial resolution of 20nm. As a proof of principal model system we choose the mechanical oscillations that gold nano discs exhibits after impulsive heating by a pump pulse are chosen. The mechanical oscillation causes a perturbation of the dielectric properties of the gold disc which is detected by a change in the scattered nearfield. The experimental setup was built up from scratch. We started with the nearfield microscope based on the aSNOM developed by R. Vogelgesang. We verified the functionality of the setup by measuring nearfields utilizing a CW laser with 1064nm and with a long coherence length. For a single nearfield scan we simultaneously obtain the z-component of the electric nearfield, the phase of the z-component of the electric nearfield and the topography signal. After this first functionality demonstration the nearfield microscope was modified to suit the demands of a pump probe scheme which means that we established zero path difference between both interferometer arms. Again we verify the functionality of the system by measuring nearfield signals, but this with the pulsed laser source with 800nm wavelength that we will need later for the timeresolved nearfield measurements. In a next step transient farfield transmission measurements have been carried out on individual gold discs. The delay dependent measurement shows a periodically modulated signal that originates from the mechanical oscillation of the gold disc that was caused through impulsive heating by a short pump pulse. We find oscillation periods that depend linearly on the radius of the discs. T-Matrix calculations are used to calculate the

scattering properties of the gold discs. We calculate the disc dimensions such that the differential cross section is maximised at the laser frequency of 800nm.

In the final step we combine the pump probe scheme with our aSNOM in order to obtain a measurement setup that has a temporal resolution of 1ps and a spatial resolution of 20nm. In order to align the setup we develop a procedure that allows to overlap two noncollinear focii in 4 dimensions on the sample surface with an AFM tip apex being centered within the focii. We then carry out the differential nearfield measurements by performing a 2d scan for several delays. We then evaluate the measured data considering the double modulated nature of the signal. With a single scan we obtain a set of 2d field maps that contain the topography, the magnitude of the z-component of the electric nearfield, the phase of the electric nearfield, the magnitude of the differential nearfield and the phase of the differential nearfield. We compare the measurement data to FEM simulations. For the nearfield signal our data shows a dipolar nearfield pattern which is in good agreement with the simulations. For the differential nearfield signal however, we obtain a ringshaped structure that is independent of the delay. This is in contrast to the simulation which predicts a dipole shaped signal for the differential nearfield signal. The ring shaped structure shown in our scans resembles the topography error signal of an AFM. Incidently the differential nearfield signal perfectly overlaps with the edges of the gold nano disc in the topography signal. We conclude that the measured differential nearfield signal is caused by an AFM artefact.

However from the obtained data we can estimate that the modulation depth of the nearfield signal has to be less than $3 \cdot 10^{-3}$. This is in agreement with T_{Matrix} calculations that estimate the relative change of the scattering cross section to be 10^{-4}. We see a similar behaviour in two other measurements. Because of a relocation and splitting of the group we can't investigate this behaviour further. As was shown the amplitude of the differential nearfield signal is $\propto A_{nf} \cdot A_{ref} \cdot A_{chop}$. Based on this term we propose different measures in order to boost the sensitivity of our setup. The most promising changes are the increase of the light collection efficiency by increasing the NA of the objective and the transition from a weakly scattering AFM tip to a gold tip that will scatter much more light due to the increased dipole moment. Additionally we propose the transition from the visible regime to the IR in order to decrease the requirements for alignment accuracy and temperature stability of the system. We are confident that through these modifications it will be possible to measure differential nearfield signals which would shed new light on interesting processes like spatially resolved charge carrier diffusion in organic solar cells, local excitation and probing of optical networks and spatially resolved conformation changes in proteins.

APPENDIX A

ppASNOM

A.1 Signal construction

For each nearfield measurement we record the topography as well as the Lock-In amplifier demodulation values X and Y for signals at the frequencies $2 * \omega_c$ and its sidebands $2 * \omega_c \pm \omega_{chop}$. Each measurement channel consists of two columns of data in which X and Y is stored. A matlab script reads the data files and constructs the complex signal amplitude

$$Z = X + iY \tag{A.1}$$

is given below:

```
clear all
close all

delays = [300 275 260 255 250 245 240  235
          230 225 220 215 210 205  200 195 190 185 170  155 ];

coords =[17 12;  15 11;  16  12;  16 12;   16 12 ;  16 11;  16 13 ;  16 11;
         16 10;  17 12 ;  16 10 ; 16 13 ;  16 12 ;  15 12 ; 15 11; 16 13;
                 17 12; 15 11; 15 11; 15 11];

path = 'data';
offset=0;
phi_chopper = 0 .* pi / 180;
signal_max = 73e-6 ;
bluepath = 'pumppowervsdelaytravel.txt';

% get norm power
 data = importdata(bluepath);
 data = data.data;

 time = data(:,1);
 time = time ./ max(time);
 norm_d = 200 - 200 .* time;
 norm_p = data(:,3);

 power = interp1(norm_d, norm_p, delays);
 power = power ./ mean(power);



for id = 1:length(delays)

    %load all files
    filename = sprintf('%03dX.dat',delays(id));
    [x2w, x2wm, x2wp, paramx, topox] =   loadmyppsnom(filename);
    filename = sprintf('%03dY.dat',delays(id));
    [y2w, y2wm, y2wp, paramy, topoy] =   loadmyppsnom(filename);

    % BG corr topo by line subtraction
    zeile = topox(21,:);
    topox = topox - repmat(zeile,paramx.xpix,1);

    % clips images to smallest of both sizes, shift if needed, NO OPTIMIZATION!
    [x2w, y2w] = adjustxy(x2w, y2w, paramx, paramy);
    [x2wp, y2wp] = adjustxy(x2wp, y2wp, paramx, paramy);
    [x2wm, y2wm] = adjustxy(x2wm, y2wm, paramx, paramy);

    % make side band as variation relative to the central peak
```

```
% this also removes all phase variations of the central peak
% x2wm = x2wm ./ x2w;
%  x2wm = x2wm ./ x2w;
%  x2wp = x2wp ./ x2w;
%  y2wm = y2wm ./ y2w;
%  y2wp = y2wp ./ y2w;

x2wm = x2wm ;
x2wp = x2wp ;
y2wm = y2wm ;
y2wp = y2wp ;

% remove the phase of the cw signal  = the phase of the cantilever
% the phase of cw signal depends of AFM artifacts, should be zero.

% complex valued NF
nf2wc= abs(x2w) + 1i .* abs(y2w);

% BG corr NF by line subtraction
zeile = nf2wc(1,:);
nf2wc = nf2wc - repmat(zeile,paramx.xpix,1);

% the interfometer phase varies over time
% project on angle so that center comes real and positive
%interf(id) = angle(nf2wc(10,10));
interf(id) = angle(nf2wc(15,17));
%interf(id) = angle(nf2wc(16,13));
nf2w = real(nf2wc .* exp(-1i .* interf(id)));
%nf2w=abs(nf2wc);

% *******
% Side bands
%
% in AM the side-bands Fourier-coeffs are CC of each other
% in FM their are identical
% see ZÃ¼rich blog entry

% contstruct AM & FM parts, as real life might be both


pp2wx_AM = x2wp + conj(x2wm);
pp2wx_FM = x2wp - conj(x2wm);

pp2wy_AM = y2wp + conj(y2wm);
pp2wy_FM = y2wp - conj(y2wm);

%there is only signla in the FM part, we ignore AM from here on
%pp2wx_r = real(pp2wx_FM .* exp(-1i .* phi_chopper));
%pp2wy_r = real(pp2wy_FM .* exp(-1i .* phi_chopper));
```

```
    %assume signal in the AM
    pp2wx_r = real(pp2wx_AM .* exp(-1i .* phi_chopper));
    pp2wy_r = real(pp2wy_AM .* exp(-1i .* phi_chopper));

    % the optical interferometer phase drifts,
    % we used above the cw signal to correct this
    % so we apply it here again to correct the pp signal
    pp2w =   ( pp2wx_r + 1i .* pp2wy_r).* exp(-1i .* interf(id)) ;

    % BG corr PP signal by line subtraction
    zeile = pp2w(1,:);
    pp2w = pp2w - repmat(zeile,paramx.xpix,1);

    % BG corr PP signal by subtraction of median of left area
    pp2w = pp2w - mean(reshape(pp2w(:,1:3), 3 * paramx.xpix,1)) ;

    % %-----------------
    % % PLOT
    %
    subplot( length(delays),6, 6 .* (id -1) +1)
    imagesc( abs(pp2w)  , [0, 1].* 1.5*10e-6   )
    colormap(hot)
    set(gca,'XTickLabel',{})
    set(gca,'YTickLabel',{})

    subplot( length(delays), 6, 6 .* (id -1) +2)
    imagesc( atan(real(pp2w)./imag(pp2w))     )
    set(gca,'XTickLabel',{})
    set(gca,'YTickLabel',{})


    subplot( length(delays), 6, 6 .* (id -1) +3)
    imagesc(nf2w.' )
    set(gca,'XTickLabel',{})
    set(gca,'YTickLabel',{})

end

    time = (180 - delays) .* 2 .* 3.333; % ps

    t = (1:600);
    y = cos(2 .* pi .* ( t ./ 120 + 170 ./ 360)) .* 0.005;
```

In addition the script calls a function *loaddata* that imports the data and construct the complex signal vectors.

```
function [ x2w, x2wm, x2wp, param, topox ] = loadmyppsnom(filename )
%LOADMYPPSNOM Summary of this function goes here
```

```
%   Detailed explanation goes here
data = importdata(     filename);
data = data.data;

 x = unique(data(:,1));
 y = unique(data(:,2));

 x2 = data(:,1);



 param.xmin = min(x);
 param.ymin = min(y);
 param.dx = abs(x(2) - x(1));
 param.dy = abs(y(2) - y(1));

 xpix = length(x);
 ypix = length(y);

 topox=reshape(data(:,10),xpix, ypix);
 topoy=1;

 param.xpix = xpix;
 param.ypix = ypix;



x2w = sqrt(reshape(data(:,4),xpix, ypix) .* reshape(data(:,4),xpix, ypix)
      + reshape(data(:,5),xpix, ypix) .* reshape(data(:,5),xpix, ypix)) .*
      exp(1i .* (pi ./ 180) .* atan((reshape(data(:,5),xpix, ypix)
      ./ reshape(data(:,4),xpix, ypix))));
x2wm = sqrt(reshape(data(:,6),xpix, ypix) .* reshape(data(:,6),xpix, ypix)
       + reshape(data(:,7),xpix, ypix) .* reshape(data(:,7),xpix, ypix)) .*
       exp(1i .* (pi ./ 180) .*  atan((reshape(data(:,7),xpix, ypix)
      ./ reshape(data(:,6),xpix, ypix))));
x2wp = sqrt(reshape(data(:,8),xpix, ypix) .* reshape(data(:,8),xpix, ypix)
      + reshape(data(:,9),xpix, ypix) .* reshape(data(:,9),xpix, ypix)) .*
      exp(1i .* (pi ./ 180) .*  atan((reshape(data(:,9),xpix, ypix)
      ./ reshape(data(:,8),xpix, ypix))));


end
```

A function $adjustXY$ that compensates thermal drifts by cutting the 2d data such that the disc topography is always centered

```
function [ax, ay] = adjustxy(axin, ayin, paramx, paramy)
```

```
ax = axin;
ay = ayin;

if (paramx.ypix ~= paramy.ypix)
    ymax = min( [paramx.ypix , paramy.ypix]);

    if (paramx.ymin == paramy.ymin)
        % starts at same place

        ax = axin(:,1:ymax);
        ay = ayin(:,1:ymax);
    else
       % we just assume that the end is the same


        ax = axin(:,end-ymax+1:end);
        ay = ayin(:,end-ymax+1:end);
    end
end

end
```

A.2 Amplitude modulated nearfield

In order to calculate the amplitude modulated nearfield signal we used a Mathematica script. In section 6.3 we only showed terms that are either modulated on the carrier frequency $2 * \omega_c$ or its sidebands $2 * \omega_c \pm \omega_{chop}$. The script as well as the full solution are given next:

```
Remove["Global`*"];
(* define time *)
Element[t, real]

(* omegac=cantilever frequency*)
Element[omegac, reals]
(* omegachop= chopper frequency*)
Element[omegachop, reals]


(* Field components*)

(* Eref=Reference beam, Aref=amplitude, Phiref=phase*)
Element[Aref, real]
Element[Phiref, real]
Eref := Aref

(* Mchop=Amplitude modulation chopper,
Achop=Modulation depth, Phichop=Chopper phase *)
Mchop1[t_] := Achop1 * 1 / 2 *
   (Exp[I * (omegachop * t + Phichop)] + Exp[-I * (omegachop * t + Phichop)])
Element[Achop1, real]
Element[Phichop, real]

(*Enear=Nearfieldsignal @2 times Cantleverfrequency,
Anear=Amplitude of Nearfield, Phinear=Phase of Nearfield*)

Enear[t_] :=
 Anear * 1 / 2 * (Exp[I * (2 * omegac * t + Phinear)] + Exp[-I * (2 * omegac * t + Phinear)])
Element[Anear, real]
Element[Phinear, real]

(*Etot=Total electric field*)
Element[Aconst, real]
Element[Enconst, real]
Etot[t_] := Eref + (1 + Mchop1[t]) * Enear[t]
g := (Abs[Etot[t]])^2
Simplify[g, g ∈ Reals && t ∈ Reals && Eref ∈ Reals && Aconst ∈ Reals &&
   Econst ∈ Reals && omegac ∈ Reals && omegachop ∈ Reals && Aref ∈ Reals &&
   Phiref ∈ Reals && Acant ∈ Reals && Phicant ∈ Reals && Achop1 ∈ Reals &&
   Achop2 ∈ Reals && Phichop ∈ Reals && Anear ∈ Reals && Phinear ∈ Reals]

omegac ∈ reals

omegachop ∈ reals

Aref ∈ real
```

Figure A.1 *Mathematica script to calculate the amplitude modulated nearfield signal*

$$\text{Phiref} \in \text{real}$$

$$\text{Acant} \in \text{real}$$

$$\text{Phicant} \in \text{real}$$

$$\text{Achop1} \in \text{real}$$

$$\text{Phichop} \in \text{real}$$

$$\text{Anear} \in \text{real}$$

$$\text{Phinear} \in \text{real}$$

$$\text{Aconst} \in \text{real}$$

$$\text{Enconst} \in \text{real}$$

$$\text{Abs}\left[\text{Aref} + \frac{1}{2}\,\text{Anear}\,\left(e^{-i\,(\text{Phinear}+2\,\text{omegac}\,t)} + e^{i\,(\text{Phinear}+2\,\text{omegac}\,t)}\right)\left(1 + \frac{1}{2}\,\text{Achop1}\,\left(e^{-i\,(\text{Phichop}+\text{omegachop}\,t)} + e^{i\,(\text{Phichop}+\text{omegachop}\,t)}\right)\right)\right]^2$$

$$\textbf{ComplexExpand}\left[\textbf{Abs}\left[\textbf{Aref} + \frac{1}{2}\,\textbf{Anear}\,\left(e^{-i\,(\text{Phinear}+2\,\text{omegac}\,t)} + e^{i\,(\text{Phinear}+2\,\text{omegac}\,t)}\right)\left(1 + \frac{1}{2}\,\textbf{Achop1}\,\left(e^{-i\,(\text{Phichop}+\text{omegachop}\,t)} + e^{i\,(\text{Phichop}+\text{omegachop}\,t)}\right)\right)\right]^2\right]$$

$$\begin{aligned}&\text{Aref}^2 + 2\,\text{Anear}\,\text{Aref}\,\text{Cos}[\text{Phinear} + 2\,\text{omegac}\,t] + \text{Anear}^2\,\text{Cos}[\text{Phinear} + 2\,\text{omegac}\,t]^2 + \\ &\ 2\,\text{Achop1}\,\text{Anear}\,\text{Aref}\,\text{Cos}[\text{Phinear} + 2\,\text{omegac}\,t]\,\text{Cos}[\text{Phichop} + \text{omegachop}\,t] + \\ &\ 2\,\text{Achop1}\,\text{Anear}^2\,\text{Cos}[\text{Phinear} + 2\,\text{omegac}\,t]^2\,\text{Cos}[\text{Phichop} + \text{omegachop}\,t] + \\ &\ \text{Achop1}^2\,\text{Anear}^2\,\text{Cos}[\text{Phinear} + 2\,\text{omegac}\,t]^2\,\text{Cos}[\text{Phichop} + \text{omegachop}\,t]^2\end{aligned}$$

TrigReduce[%831]

$$\begin{aligned}&\frac{1}{8}\,\left(4\,\text{Anear}^2 + 2\,\text{Achop1}^2\,\text{Anear}^2 + 8\,\text{Aref}^2 + 16\,\text{Anear}\,\text{Aref}\,\text{Cos}[\text{Phinear} + 2\,\text{omegac}\,t] + \right. \\ &\quad 4\,\text{Anear}^2\,\text{Cos}[2\,\text{Phinear} + 4\,\text{omegac}\,t] + 2\,\text{Achop1}^2\,\text{Anear}^2\,\text{Cos}[2\,\text{Phinear} + 4\,\text{omegac}\,t] + \\ &\quad 8\,\text{Achop1}\,\text{Anear}^2\,\text{Cos}[\text{Phichop} + \text{omegachop}\,t] + \\ &\quad 4\,\text{Achop1}\,\text{Anear}^2\,\text{Cos}[\text{Phichop} - 2\,\text{Phinear} - 4\,\text{omegac}\,t + \text{omegachop}\,t] + \\ &\quad 8\,\text{Achop1}\,\text{Anear}\,\text{Aref}\,\text{Cos}[\text{Phichop} - \text{Phinear} - 2\,\text{omegac}\,t + \text{omegachop}\,t] + \\ &\quad 8\,\text{Achop1}\,\text{Anear}\,\text{Aref}\,\text{Cos}[\text{Phichop} + \text{Phinear} + 2\,\text{omegac}\,t + \text{omegachop}\,t] + \\ &\quad 4\,\text{Achop1}\,\text{Anear}^2\,\text{Cos}[\text{Phichop} + 2\,\text{Phinear} + 4\,\text{omegac}\,t + \text{omegachop}\,t] + \\ &\quad 2\,\text{Achop1}^2\,\text{Anear}^2\,\text{Cos}[2\,\text{Phichop} + 2\,\text{omegachop}\,t] + \\ &\quad \text{Achop1}^2\,\text{Anear}^2\,\text{Cos}[2\,\text{Phichop} - 2\,\text{Phinear} - 4\,\text{omegac}\,t + 2\,\text{omegachop}\,t] + \\ &\quad \left.\text{Achop1}^2\,\text{Anear}^2\,\text{Cos}[2\,\text{Phichop} + 2\,\text{Phinear} + 4\,\text{omegac}\,t + 2\,\text{omegachop}\,t]\right)\end{aligned}$$

Figure A.2 *Mathematica script to calculate the amplitude modulated nearfield signal*

Bibliography

[1] A.Van Helden, R. Van Gent, and H. Zuidervaart. *The Origins of the Telescope*. Amsterdam University Press, Amsterdam, 2011.

[2] R. Lemons and C.F. Quate. Acoustic microscopy - scanning version. *Appl. Phys. Lett.*, 24:163–165, 1974.

[3] B. Ward et al. Helium-ion microscopy. a beam of individual helium ions creates images that challenge sem and other microscopy techniques. *Photonics Spectra*, 41(8):68–70, 2007.

[4] D. Liu. Demonstration of a novel focussing small-angle neutron scattering instrument equipped with axisymmetric mirrors. *Nature Communications*, 4(2556), 2013.

[5] H. Rohrer G. Binnig. Scanning tunneling microscopy. *IBM Journal of Research and Development*, 1986.

[6] G. Binnig, C. Quate, and C. Gerber. Atomic force microscope. *Physical Review Letters*, 56:930–933, 1986.

[7] C. Chen et al. Origin of atomic resolution on metal surfaces in scanning tunneling microscopy. *Physical Review Letters*, 65(4):448–451, 1990.

[8] L. Reimer and H. Kohl. *Transmission Electron Microscopy: Physics of Image Formation*. Springer, 2008.

[9] S. Hell and J. Wichmann et al. Breaking the diffraction resolution limit by stimulated emission: stimulated-emission-depletion fluorescence microscopy. *Optics Letters*, 19(11):780–782, 1994.

[10] T. Klar and S. Hell. Subdiffraction resolution in far-field fluorescence microscopy. *Optics Letters*, 24(44):954–956, 1999.

[11] E. Betzig et al. Imaging intracellular fluorescent proteins at nanometer resolution. *Science*, 313(5793):1642–1645, 2006.

[12] S. Hess et al. Ultra-high resolution imaging by fluorescence photoactivation localization microscopy. *Biophysical Journal*, 91(11):4258–4272, 2006.

[13] M. Rust etal. Sub-diffraction-limit imaging by stochastic optical reconstruction microscopy (storm). *Nature Methods*, 3:793–796, 2006.

[14] U. Düerig et al. Near-field optical scanning microscopy. *Journal of Applied Physics*, 59:3318, 1986.

[15] T. Güenter et al. Femtosecond near-field spectroscopy of a single gaas quantum wire. *Applied Physics Letters*, 22(29), 1999.

[16] Y. Nishiyama. Plasmon dephasing in single gold nanorods observed by ultrafast time-resolved near-field optical microscopy. *J. Chem. Phys. C*, 119(28):16215–16222, 2015.

[17] A. Zewail. 4d ultrafast electron diffraction, crystallography and microscopy. *Annual Review of Physical Chemistry*, 57:65–103, 2006.

[18] A. Zewail. Four-dimensional electron microscopy. *Science*, 328(5975):187–193, 2010.

[19] M. Aeschlimann et al. Coherent two-dimensional nanoscopy. *Science*, 333(605):1723–1723, 2011.

[20] M. Esslinger, R. Vogelgesang, and K. Kern. Background-free imaging in apertureless scanning nearfield optical microscopy. *Review of Scientific Instruments*, 83(3), 2012.

[21] Markus B. Raschke and Christoph Lienau. Apertureless near-field optical microscopy: Tip-sample coupling in elastic light scattering. *Applied Physical Letters*, 83(24):5089–5091, 2003.

[22] A. Doicu. *Light Scattering by Systems of Particles. Null-Field Method with Discrete Sources – Theory and Programs*. Springer, 2006.

[23] K. Kopitzky. *Einführung in die Festkörperphysik*. Teubner StudienbÃ¼cher, 1993.

[24] C. Rockstuhl. Zur elektronentheorie der metalle; ii. teil. galvanomagnetische und thermomagnetische effecte. *Annalen der Physik*, 308(11):369–402, 1900.

[25] M. A. Ordal, Robert J. Bell, R. W. Alexander, L. L. Long, , and M. R. Querry. Optical properties of fourteen metals in the infrared and far infrared: Al, co, cu, au, fe, pb, mo, ni, pd, pt, ag, ti, v, and w. *Annalen der Physik*, 24(24):4493–4499, 1985.

[26] P. B. Johnson and R. W. Christy. Optical constants of noble metals. *Phys. Rev. B*, 6(12):4370–4379, 1972.

[27] Timothy J. Davis, Kristy C. Vernon, , and Daniel E. Gomez. Effect of retardation on localized surface plasmon resonances in a metallic nanorod. *Optics Express*, 17(26):23655–23663, 2009.

[28] C. Bohren and D. Huffman. *Absorption and lightscattering of light by small particles*. Wiley VCH, 1995.

[29] G. Mie. Articles on the optical characteristics of turbid tubes, especially colloidal metal solutions. *Annalen der Physik*, 25(3):377–445, MAR 1908.

[30] U. Kreibig and M. Vollmer. *Properties of Metal Clusters*. Springer, Berling, 1995.

[31] K. Kratzer. Nonlinear spectroscopy using nanoantennas. Diplomarbeit, Max Planck Institute for Solid State Research, 2010.

[32] P.C. Waterman. Matrix formulation of electromagnetic scattering. *Proc. IEEE Vol.*, 53:9805, 1965.

[33] F.R.S Rayleigh. Investigations in optics, with special reference to the spectroscope. *Philosophical Magazine*, 55(49):261–274, 1879.

[34] E.H. Synge. A suggested method for extending the microscopic resolution into the ultramicroscopic region. *Phil. Mag.*, 6:356, 1928.

[35] Novotny, Lukas, Hecht, and Bert. *Principles of Nano-Optics*. Cambridge University Press, Cambridge, 2012.

[36] F. Zenhausen, Y. Martin, and H.K. Wickramasinghe. Scanning interferometric apertureless microscopy: optical imaging at 10 angstrom resolution. *Science*, 269(5227):1083–5, 1995.

[37] P.K. Aravind and H. Metiu. The effects of the interaction between resonances in the electromagnetic response of a sphere-plane structure; applications to surface enhanced spectroscopy. *Surface Science*, 124:506–528, 1983.

[38] M. Brehm, A. Schliesser, F. Cajko, I. Tsukerman, , and F. Keilmann. Antenna-mediated back-scattering efficiency in infrared near-field microscopy. *Applied Physical Letters*, 16(15):11215, 2008.

[39] D. Burt, P. Dobson, L. Donaldson, and J. Weaver. A simple method for high yield fabrication of sharp silicon tips. *Applied Physical Letters*, 85(3):623–630, 2008.

[40] C. Rockstuhl. Direct near-field optical imaging of higher order plasmonic resonances. *Nano Letters*, 8(10):3155–3159, 2008.

[41] R. Hillenbrand and F. Keilmann. Complex optical constants on a subwavelength scale. *Physical Review Letters*, 85:3029, 2000.

[42] A. Lipson and S. Lipson. *Optical Physics*. Cambridge University, Cambridge, 2010.

[43] W. Drexler and J. Fujimoto. *Optical Coherence Tomography*. Springer Science, 2008.

[44] J. Bigot et al. Electron dynamics in metallic nanoparticles. *Chemical Physics*, 251(1-3):181–203, JAN 1 2000.

[45] M. Perner et al. Optically induced damping of the surface plasmon resonance in gold colloids. *Physical Review Letters*, 78(11):2192–2195, MAR 17 1997.

[46] J. Bosbach et al. Ultrafast dephasing of surface plasmon excitation in silver nanoparticles: Influence of particle size, shape, and chemical surrounding. *Physical Review Letters*, 89(25):257404, DEC 16 2002.

[47] C. Sönnichsen, T. Franzl, T. Wilk, G. von Plessen, J. Feldmann, O. Wilson, and P. Mulvaney. Drastic reduction of plasmon damping in gold nanorods. *Physical Review Letters*, 88(7):077402, FEB 18 2002.

[48] R. W. Schoenlein, W.Z. Lin, J.G. Fujimoto, and G.L. Esley. Femtosecond studies of nonequilibrium electronic processes in metals. *Physical Review Letters*, 58(16):1680–1683, 1987.

[49] R.H. Kop and R. Sprik. Phase-sensitive interferometry with ultra-short optical pulses. *Review of Scientif Instruments*, 66(12):5459–5463, 1995.

[50] J.H. Hodak, I. Martini, and G.V. Hartland. Observation of acoustic quantum beats in nanometer sized au particles. *J. Chem. Phy.*, 108(22):9210–9213, 1999.

[51] M.A van Dijk, M. Lippitz, and M. Orrit. Detection of acoustic oscillations of single gold nanospheres by time-resolved interferometry. *Physical Review Letters*, 95(26):267406, 2005.

[52] J. Hodak, A. Henglein, and G. Hartland. Size dependent properties of au particles: Coherent excitation and dephasing of acoustic vibrational modes. *J. Chem. Phys.*, 111(18):8613–8621, 1999.

[53] M. Perner et al. Observation of hot-electron pressure in the vibration dynamics of metal nanoparticles. *Physical Review Letters*, 85(4):792–795, 2000.

[54] H. Lamb. On the vibrations of an elastic sphere. *Proc. London. Math. Soc.*, s1-13:189–212, 1881.

[55] L. Saviot. Size dependence of acoustic and optical vibrational modes of cdse nanocrystals in glasses. *Journal of Non-Crystalline Solids*, 197(2-3):238–246, 1996.

[56] *Comsol Multiphysics Structural Mechanics - User's Guide*. Comsol, 2012. Version: 4.3.

[57] E. Wilson. *Static and Dynamic Analysis of Structures*. Springer, 2004.

[58] W. Demtröeder. *Experimentalphysik 1: Mechanik und Wärme*. Springer, Cambridge, 2008.

[59] *Comsol Multiphysics Studies and Solvers - User's Guide*. Comsol, 2012. Version: 4.3.

[60] Meindert Alexander van Dijk. Nonlinear-optical studies of single gold nanoparticles. Phd-thesis, Universiteit Leiden, 2007.

[61] D. Lide. *CRC handbook of chemistry and physics: a ready-reference of chemical and physical data*. CRC Press, 2003.

[62] M. Knight. Phase-matched excitation of whispering-gallery-mode resonances by a fiber taper. *Optics Letters*, 22(15):1129, 1997.

[63] J. Diels and W. Rudolph. *Ultrashort Laser Pulse Phenomena*. Academic Press, Massachusetts, 2006.

[64] S. Bohzevolnyi and L. Kuypers. Near-field characterization of photonic crystal waveguides. *Semiconductor Science and Technology*, 21:R1–R16, 2006.

[65] R. Hillenbrand. Pure optical contrast in scattering-type near-field optical microscopy. *Journal of Microscopy*, 202(1):77–83, 2001.

[66] *Comsol Multiphysics RF Module - User's Guide*. Comsol, 2012. Version: 4.3.

[67] T. Schumacher, Kai. Kratzer, D. Molnar, M. Hentschel, H. Giessen, and M. Lippitz. Nanoantenna-enhanced ultrafast nonlinear spectroscopy of a single gold nanoparticle. *Nature Communications*, 2:333, MAY 2011.

[68] T. Schumacher. Optical nanoantennas for ultrafast nonlinear spectroscopy of individual nanosystems. Phd-thesis, Universität Bayreuth, 2014.

[69] R. Esteban, R. Vogelgesang, and K. Kern. Direct near-field optical imaging of higher order plasmonic resonances. *Nano Letters*, 8(10):3155–3159, 2008.

[70] W. Drexler and J. Fujimoto. *Optical Coherence Tomography*. Springer Science, 2008.

[71] P. Drude. Zur elektronentheorie der metalle. *Annalen der Physik*, 306(3):566–613, 1900.

[72] *Manual: Agilent Spectrum Analysis Amplitude and Frequency Modulation*. Stanford Research Systems, 2011. Application Note 150-1.

[73] Y. Takahashi et al. Heat capacity of gold between 80k and 1000k. *Thermochimica Acta*, 109:105–109, 1986.

[74] W. Schottky. über spontane stromschwankungen in verschiedenen elektrizitätsleitern. *Annalen der Physik*, 57:541–567, 1918.

[75] *Manual: MODEL SR830 DSP Lock - In Amplifier*. Stanford Research Systems, 2011. Revision 2.5 (10/2011).

[76] J. Fourkas. Rapid determination of the three-dimensional orientation of single molecules. *Optics Letters*, 26(4):211, 2001.

[77] M. Esslinger and R. Vogelgesang. Reciprocity theory of apertureless scanning nearfield optical microscopy with point-dipole probes. *ACS Nano*, 6(9):8173–8182, 2012.

Erklärung

Hiermit versichere ich an Eides statt, dass ich die vorliegende Arbeit selbstständig verfasst und keine anderen als die angegebenen Quellen und Hilfsmittel verwendet habe. Ich erkläre, dass ich bisher keinen anderweitigen Promotionsversuch unternommen habe und die Hilfe von gewerblichen Promotionsberatern bzw. Promotionsvermittlern oder ähnlichen Dienstleistern weder bisher in Anspruch genommen habe noch künftig in Anspruch nehmen werde.

Frauenneuharting, den 21. Januar 2016

Matthias Brandstetter